Assessment of the effects of soil variability in the modeling of liquefiable soils

By

María Fernanda Pico Duarte

A thesis submitted to the Department of Civil Engineering

Universidad del Norte

To obtain the Degree of Master of Science

Barranquilla, Colombia

April 6th /2021

Abstract

Soil liquefaction causes catastrophic consequences in terms of structural damage and loss of human lives. Therefore, geotechnical engineers have developed constitutive models that are able to predict the response of liquefiable soils. However, there is not a standard procedure to validate these models. As a result, the Liquefaction Experiments and Analysis Project (LEAP) was created with the aim to produce accurate experimental data that could be used to validate and evaluate the existing constitutive models' advantages and limitations. Nevertheless, to make a complete evaluation of the numerical models, the soil properties must be well known, as well as the uncertainties associated with these properties.

This research presents a stochastic analysis to asset the effects of considering the spatial variability of a soil deposit formed by liquefiable soils. To develop this analysis, a deterministic finite element model was implemented using the Finite Element platform OpenSees. The soil was modeled using the pressure-dependent multi-yield-surface model "PDMY02". The soil model properties were calibrated using cyclic triaxial tests performed by Andrew Vasko [1] , ElGhoraiby , Park and Manzari [2] and Ochoa-Cornejo et al [3]. Afterwards, the deterministic simulations were validated using the LEAP2020 experimental results. Consequently, the stochastic analysis was implemented using the Random Finite Element Method (RFEM). To evaluate the effects of the spatial variability of the soil, the relative density was modeled as a spatial correlated gaussian random field, considering two scenarios: the first scenario represents the uncertainties expected in an experimental soil deposit, while the second scenario, simulates the in-situ soil conditions. Additionally, in a random field, the variables can be related to each other in terms of the correlation length, which represents the relationship between the variables. A small correlation length means the variables are not related to each other. While a large correlation distance represents a greater relationship between the variables

over a greater area. In this study, three different correlation lengths were considered to address the correlation existing between the properties of the soil deposit. The soil was evaluated in terms of acceleration response, spectral acceleration, excess pore-water pressure, horizontal displacements, and vertical settlements. The results from the deterministic simulations were compared with the results from the stochastic analyses to evaluate the differences between these two approaches. Finally, the results of this study showed that addressing soil variability in a geotechnical system is a powerful tool to predict the soil response in terms of a confidence interval, which is helpful for making safer and optimal designs.

Keywords: Liquefaction modeling, Centrifuge testing, Finite Element Modeling, soil variability, stochastic analysis, Random Finite Element Modeling,

Acknowledgements

I would like to express my sincere gratitude to my supervisors Prof. Vicente Mercado PhD and Prof. Waleed El-Skelly PhD for their guidance throughout this research. Their work and motivation have been an inspiration that helped me accomplished this goal. I am extremely grateful for all their patience and support.

Also, I owe a deep sense of gratitude to Prof. William Fuentes PhD, who introduced me to Soil Mechanics and whose teachings have had a big impact in my career as a researcher. I would also like to thank Prof. Ruben Tovar PhD for sharing his big passion for knowledge and innovation with us and Prof. Elias Niño PhD for his contributions for the development of this research.

I am extremely thankful to my family, especially, to my mother, who is the most intelligent and strong woman I know. She has encouraged me to develop my abstract and analytical thinking since I was a little girl.

I thank Cata, Leo, Dani, Diani, and Bruno for being always there for me. Mely and Andres for their company during my studies. Finally, thanks to all my twitter followers who showed me their unconditional support #LaPicoTesis.

Table of contents

List of figures

List of tables

1. Description of the project

1.1. Introduction

The phenomenon of liquefaction has caused several disasters in different countries such as Haiti, Chile, Japan, and New Zealand. [4] [5] [6]. Gonzalo et al. [7] defines liquefaction as "the phenomenon wherein a saturated sand loses a large percentage of its shear resistance (due to monotonic or to cyclic loading) and flows in a manner resembling a liquid until the shear stresses acting on the mass are as low as its reduced shear resistance. Thus, a slope that liquefies comes to rest only when the slope has been reduced to a few degrees, and a building whose foundation soil liquified will sink or float until the shear stresses in the foundation are consistent with the reduced shear resistance".

Liquefaction have caused devastating consequences to structures and even human lives. For this reason, geotechnical engineers have been developing different numerical constitutive models with the purpose of representing the behavior of the soil under a variety of types of loading such as seismic loads. Different families of this constitutive models have been proposed (e.g. simple plastic models [8], critical state [9] [10] [11], incrementally nonlinear [12] [13] [14] [15], multiple surfaces [16] [17] [18] [19], double hardening [20] [21] [22] , bounding surface [23] [24] [25], single yield surface [26] [27] [28].). However, a standard procedure to calibrate and validate those constitutive models does not exist yet. Therefore, The Liquefaction Experiments and Analysis Project (LEAP) was born as a solution to produce more reliable and high-quality data that could be available to validate the existing constitutive models and numerical methods that are now implement for geotechnical engineering problems.

Additionally, in these constitutive models the soil is assumed to be a homogenous material without considering its different levels of variability that can be defined according to Uzielli et Al. as [29] "*Stratigraphic heterogeneity*, which is the result of large-scale geologic and geomorphological processes. *Lithological heterogeneity*, that happens when a soft layer is

embedded in a stiffer media or with the appearance of pockets of different lithology in a relative uniform soil mass and *Inherent soil variability*, that can be defined as the variation of a property from one spatial location to another inside a soil mass".

Soil variability have a big impact in geotechnical analysis, because it is one of the major contributors to uncertainty in geotechnical systems, because the soil is not a homogenous material and geotechnical site investigation uses methods that are subjected to human error, which can reduce the accuracy of the results. Moreover, developing an exploration in such detail will have an elevate cost. Different authors have addressed soil variability for different geotechnical problems (e.g. sloping ground [30] [31], soil-structure interaction [32], settlements [33] , bearing capacity [34], liquefaction [31], and offshore foundation design [35]). They have found that considering soil variability can lead to more rational and optimal designs.

This research aims to assess the effects of soil variability in the analysis of a retaining wall supporting liquifiable soils that are subjected to a seismic event. The numerical model was implemented in the Finite Element platform OpenSees [36]. The soil was modeled using a pressure-dependent multi-yield-surface model named as "PDYM02" [37] [38] [39]. The Finite Element model was developed within the framework of the Liquefaction and Experiment Analysis Project (LEAP 2020) by the simulation team from Universidad del Norte. To evaluate the effects of soil variability, the constitutive model PDMY02 was calibrated using triaxial experiments and it was validated using the results of the centrifuge test that were developed in the LEAP 2020 version. Afterwards, a Random Finite Element Analysis was implemented. To account for soil variability in the stochastic analysis, the relative density of the soil was modeled as a gaussian multivariate random spatial correlated field. Afterwards, each element within the Finite Element mesh was assigned with a value of the relative density generated with the random field. Two different scenarios were considered; the first scenario simulates the range of variation of the soil in laboratory conditions and the second scenario represents the expected variation of the soil in-situ conditions. Additionally, each of these scenarios were evaluated with three different correlation lengths, which represent the relationships that a soil deposit can exhibit between its properties.

1.2. Objective

1.2.1. General objective

Evaluate the effects of soil variability in the response of a liquefiable soils deposit supported by a retaining wall.

1.2.2. Specific objectives

- Calibrate the constitutive model PDMY02 for different relative densities: 55%, 65%, 75% and 90% using triaxial experiments to predict the soil post-liquefaction behavior.
- Evaluate the advantages and limitations of the PDYM02 model using the predicted results and the centrifuge tests available from LEAP-2020.
- Represent spatial soil variability as a Gaussian Random Field in terms of the relative density.
- Evaluate the effects on the soil response of different correlation lengths in a Gaussian Random Field.
- Implement a stochastic analysis based on the Random Finite Element Analysis (RFEA) to assess the effects of soil variability in liquefaction modeling.
- Evaluate the advantages and limitations of performing deterministic analysis versus stochastic analyses for the geotechnical problem in consideration.

1.3. Research Questions

- Which are the effects of considering soil variability in liquefaction soil modeling?
- Which are the limitations and capabilities of the constitutive model “PDMY02” to predict the response of liquefiable soils subjected to a seismic event?

1.4. Thesis Outline

This work is composed by seven chapters. The first chapter presents the introduction, description of the project and its objectives.

The second chapter is composed by the literature review of the three main topics of the research: liquefaction, constitutive modeling, and soil variability.

Afterwards, the theoretical framework is presented in chapter three addressing the fundamentals concepts and theories that were used to analyze the problems previously discussed.

Chapter four describes the methodology that was implemented to achieve the main goals of the research. Therefore, a brief description of the steps that were followed to calibrate the constitutive model and to execute the deterministic and probabilistic simulations are described in this chapter.

Chapter five present the assumptions considered for the development of the finite element model and the model set-up.

Chapter six presents a comparison between the deterministic simulations and the probabilistic analyses. This chapter explains the reader the reasons considered to select the final parameters for the constitutive model calibration. Later, an explanation of the probabilistic approach is presented to the reader, in which the correlated random field generation is explained, and the implementation of the random finite element analysis is described. Afterwards, the results obtained from using the stochastic analysis are compared with the deterministic analysis and the results from the centrifuge experiments from LEAP2020. The results are presented in terms of acceleration, spectral accelerations, excess pore-water pressure, and displacements compared to the deterministic analyses that were conducted.

Finally, chapter seven presents the conclusions regarding this research, its limitations, and recommendations for future work.

1.5. Liquefaction Experiments and Analysis Projects (LEAP)

The Liquefaction Experiments and Analysis projects (LEAP) is an international group of collaborative research projects that have been developed with the main purpose of producing high quality experimental data that can be used to evaluate, calibrate, and validate the existing constitutive models and numerical simulation procedures that are available today for soil liquefaction modeling. This project is based on the VELACS (Verification of Liquefaction Analysis by Centrifuge Studies) projected created by K. Arulanandan and R.F Scott in 1990 [40]. Since then, different versions (LEAP-GWU-2015 [41], LEAP-UCD-2017 [42], LEAP-

ASIA-2019 [43] and LEAP-2020) have been developed through the years leading to new challenges.

Previous leap phases have been hosted (LEAP-GWU-2015, LEAP-UCD-2017, LEAP-Asia-2019) in different international universities and researchers from several countries have participated trough the implementation of numerical models and centrifuge testing. The LEAP 2020 phase consisted in the evaluation of the seismic response of a retaining wall supporting liquefiable soils as shown in Figure 1.

For the version in 2020 of the Liquefaction Experiments and Analysis Projects (LEAP-2020) several centrifuge experiments were performed at 10 different centrifuge facilities across the world. The tests were conducted using three relative densities (D_R=55%, D_R=65% and D_R=75%) and two types of base motions. Also, several numerical teams from different universities participated by proposing their numerical models to predicting the soil response of the problem in consideration. The response was evaluated in terms of time history accelerations, spectral acceleration, pore-water pressure, and vertical and horizontal displacements. At the end, the predictions from the numerical teams were compared with the centrifuge experiments to analyze the ability of the numerical tools to predict the soil response and their limitations.

La Universidad del Norte participated in this version with a numerical modeling team that presented type B (blind predictions) [44] and type C predictions (named in this research as deterministic predictions) [45]. The numerical model was implemented in the Finite Element platform OpenSees [36]. The soil was modeled using a pressure-dependent multi-surface plasticity constitutive model called “PDYM02” [46] [38] [37] [39]. The soil is supported by a sheet-pile as presented in Figure 1. An elastic material was used to simulate the sheet-pile. This thesis presents the results from the deterministic predictions developed at La Universidad del Norte within the project framework and it also evaluates the effects of considering the inherent soil variability in this type of numerical models.

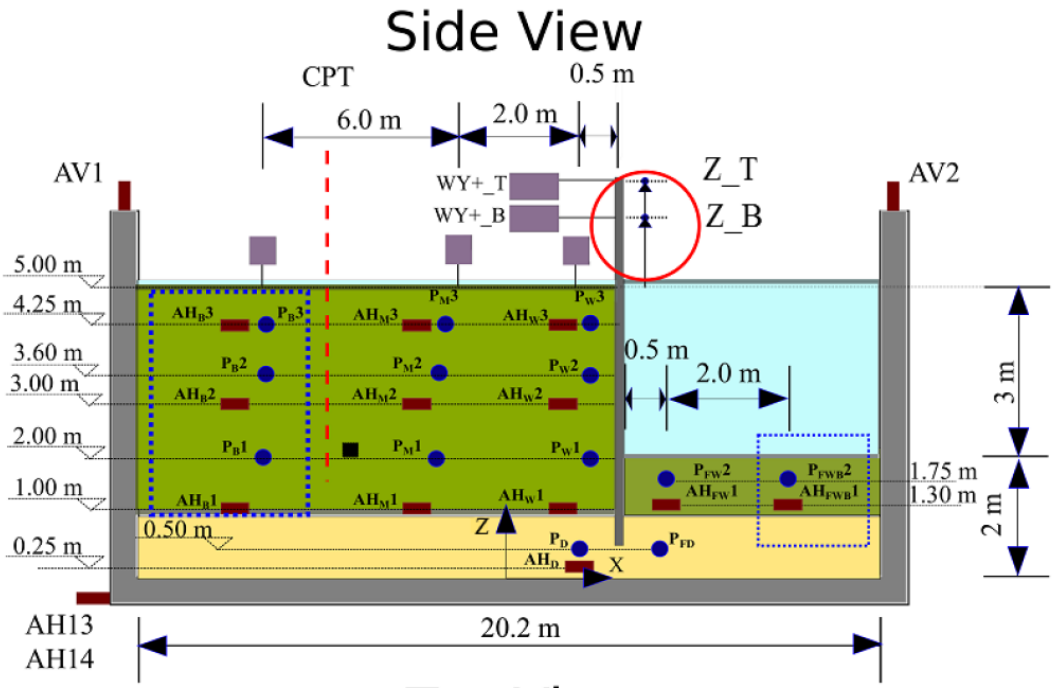

Figure 1. Experimental setup and instrumentation for LEAP 2020. Taken From [47]

2. Literature Review

Due to different formation processes, such as erosion, weathering, and sedimentation and the different natural and loading conditions to which the soil is subjected in the field, the soil can present high variability in its properties from one location to another. Therefore, evaluating the effects of soil variability in soil liquefaction modeling presents a better understanding and more realistic results of the soil response in a geotechnical analysis, because the soil presents heterogenous properties.

To develop a geotechnical analysis that accounts for soil variability different concepts must be take into consideration. This section presents the state of the art of these topics as follows: firstly, the liquefaction problem and the existing methods to evaluate this phenomenon are briefly described, because liquefaction represents the soils dynamic load condition that this research accounts for. Secondly, this research uses a constitutive model to predict the soil behavior, therefore some of the existing constitutive modeling families are analyzed to have a better insight of their advantages and disadvantages. Finally, different studies where soil variability is considered are presented to understand their methods and the advantages that these analyses have showed.

2.1. Liquefaction

Liquefaction-induced deformation of the soil and soil-structure systems can produce devasting consequences, such as mortality and substantial damage as shown in Figure 2. This seismic response has caused several damages in different countries such as Haiti, Chile, Japan, United States, Costa Rica, Indonesia, and New Zealand. [4], [5], [6]. Liquefaction occurs because of a rapid loss of shear strength in cohesionless soils subjected to dynamic load. Dry cohesionless soils have the tendency to densify under both static and cyclic loading. When cohesionless soils are saturated and rapid loading occurs under undrained conditions, the tendency for densification causes excess pore-water pressure to increase and effective stresses to decrease,

as a result, the soil behaves as a viscous fluid, causing permanent deformations or even conditions near to zero effective stress in the soil.

According to Li & Ming [48], the essential responses of granular soils to earthquake loading include flow liquefaction and cyclic mobility. The former is associated with the contractive behavior of the loose materials, it can occur under static or cyclic loading condition when in-situ shear stresses are greater than the minimum undrained shear strength and failure can result in slide or flow depending upon the internal geometry and the stress state. On the other hand, cyclic mobility relates to the dilative response of loose and dense materials at low confining stresses. This phenomenon can occur at cyclic loading without stress reversal, it is controlled by static and cyclic shear stresses and it presents a limited deformation potential, unless the soil is very loose, which can result in flow liquefaction.

Figure 2. a) Liquefaction damage after 1989 Loma Prieta Earthquake. Taken from [49]b) Liquefaction damage after 1991 Costa Rica Earthquake [49] c) Liquefaction consequences after earthquake in Christchurch (New Zealand .Taken from [50] d) Consequences of soil liquefaction after Earthquake in Palu, Indonesia. [51]

Nowadays several methods to evaluate liquefaction have been developed by researchers. [52] The most common are energy based [53] [54] [55]; cyclic stress-based [56] [57] [58], and

Strain Based [59] [60] [61]. Energy based methods present an estimation of the energy that is dissipated into the soil by earthquake loads. Stress-based methods calculate the liquefaction potential as the ratio between the cyclic stress ratio (CSR) and the cyclic shear strength (CRR). Meanwhile, strain-based models suppose that changes in pore-water pressure depends on the cyclic shear strain loads. Most of the mentioned procedures are simplifications that have showed good results for level ground. Nevertheless, these methods do not provide more information about ground settlement and sometimes they cannot be applied for certain geotechnical problems such as retaining structures. For this reason, researchers have been working on formulating constitutive models that capture the liquefaction-induced excess pore-water pressure and ground deformation. The constitutive models are combined with numerical methods such as Finite Element Analyses, which brings the possibility of analyzing the system in terms of the stress-strain behavior of the material.

2.2. Constitutive modeling

Soil behavior is not easy to model because it is composed by a solid skeleton and voids that are filled with gas and water. Moreover, the behavior of geological materials is influenced by factors such as in situ conditions, volume change, saturated and unsaturated states, softening, degradation, fractures, and microstructural instabilities such as liquefaction. Therefore, principles of continuum mechanics have been applied to capture the behavior of soil skeleton, combined with physical laws of incompressible and compressible fluids to represent the behavior of its components [62].

According to Desai [63] "… a constitutive law or model represents a mathematical definition for the behavior of a material based on laboratory and/or field tests that includes the most representative factors affecting the behavior…". Constitutive models aim to predict the stress-strain behavior of the soil. These models are based on the theories of elasticity, plasticity, visco-plasticity, micro-fracture, and damage mechanics. Thanks to the implementation of these models combined with numerical methods (e.g., finite element and finite difference) any geotechnical structure can be analyzed by dividing its shape into a finite number of elements, which represents a big achievement in geotechnical sciences, because most of the older methods were not able to describe the soil behavior in terms of deformations and stress conditions for the entire loading history.

The constitutive models can be divided in the following groups based on their fundamental criteria: [62] a) simple plastic models [8] [64] [65] b) critical state [9] [10] [11] c) incrementally nonlinear [12] [13] [14] [15] d) multiple surfaces [16] [17] [18] [19] e) double hardening [20] [21] [22] f) bounding surface [23] [24] [25] g) single yield surface [26] [27] [28]. Since the development of the pioneer constitutive models, researchers have been working on updating their formulations to produce a soil model that accounts for better predictions of the soil response to different load conditions. The following review presents some of the most common constitutive models used to predict the response of liquefiable soils and their development.

The family of Simple ANIsotropic SAND (SANISAND) of constitutive models was formulated within the framework of critical state soil mechanics and bounding surface plasticity [66] [67] [68]. In 1997, Manzari and Dafalias [66] proposed its first version, which was attractive for its simplicity and foundations in concepts that were understood by the geotechnical engineering community. The model was able to simulate the stress-strain behavior of sands under monotonic, cyclic, drained, and undrained loading conditions using a unique set of model constants at all densities and confining pressures for a given sand. However, the model showed certain limitations, such as the lack of a proper Lode angle in the multiaxial generalization for the dependence of the plastic deviatoric strain rate direction. For this reason, in 2004 Dafalias and Manzari [69], updated the existing formulation to reproduce the effect of fabric changes during the dilatant phase of deformation and the ensuing realistic simulation of the sand behavior under undrained cyclic loading using a fabric-dilatancy related quantity in the triaxial and generalized stress space. Also, the plastic strain rate direction was changed to be dependent of a modified Lode angle in the multiaxial generalization to enable the reproduction of realistic stress-strain simulations in non-triaxial conditions. However, the model only obeyed rotational hardening due to its original yield surface, which dictates that only changes of the stress ratio can cause plastic deformation, while constant stress-ratio loading induces only elastic response. Hence, in 2008 Taiebat and Dafalias [70] implemented a new equation to have a narrow but closed cone-type yield surface that follows rotational and isotropic hardening. Figure 3 presents an illustrative comparison between the original model surfaces and the last yield surface modification. Thanks to this modification, the model is now able to predict plastic strains during any type of constant stress-ratio loading.

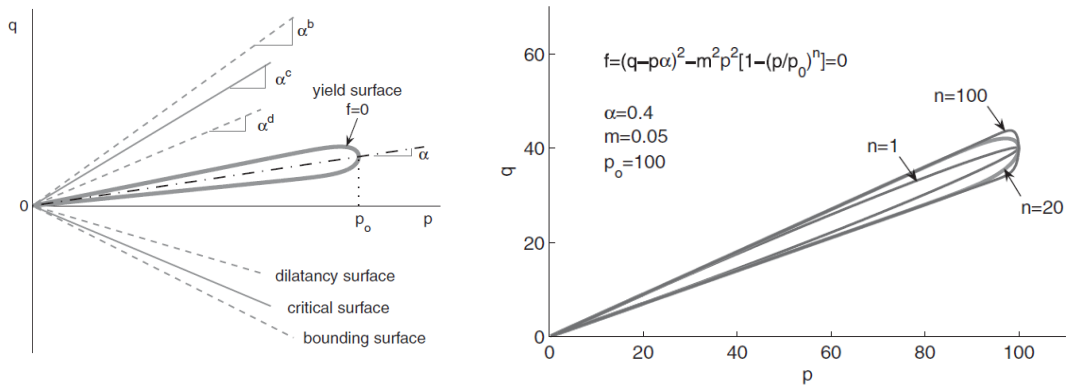

Figure 3.a) P-q diagram of the model surfaces in triaxial stress space proposed by Manzari & Dafalias. Taken from [70] b) p-q Diagram of the modification of the yield surface. Taken from [70]

The PM4Sand plasticity model is a stress-ratio controlled and critical state compatible formulation based on the bounding surface plasticity model presented by Dafalias and Manzari [69]. It was first formulated by Boulanger and Ziotopoulou [71] in 2013. The new implementations included a fabric formation function that depends on plastic shear, a modified plastic modulus relationship, which was made dependent on fabric and a modifying dilatancy relationship for controlling volumetric contraction. Figure 4 and Figure 5 present the modifications in the soil response that can be achieved when considering the fabric term in undrained cyclic direct shear stress conditions, in terms of the shear stress ratio (τ/σ'_{VC}) versus the shear strain (γ) and the vertical effective stress (σ'_V/σ'_{VC}) . Also, the model was able to respond to various loading conditions, including drained and undrained monotonic and cyclic loading. However, one of the limitations of this version was that it tended to over-estimate the accumulation of shear strains under sloping ground conditions during irregular cyclic loading.

Therefore, the PM4Sand (PM4Sand Version 2) was updated in 2016 to improve simulations of liquefaction-induced deformations of sloping ground subjected to uniform and irregular cyclic loading. In this version [72], a new rotated dilation surface in function of the fabric and type of loading was introduced. The dilatancy and plastic modulus was modified to be dependent on the fabric and type of loading. Also, the methodology for tracking initial back-stress ratios with respect to loading reversals was updated. Consequently, the model was shown to improve the modeling of stress paths and strain accumulation during undrained irregular cyclic loading with and without shear stress reversals. Figure 6 presents an example of the undrained irregular cyclic DSS loading responses for two different relative densities with

vertical effective consolidation stress of 100 kPa using the PM4Sand Version 2, in terms of the shear stress ratio (τ/σ'_{VC}) versus the shear strain (γ) and the vertical effective stress (σ'_V/σ'_{VC}).

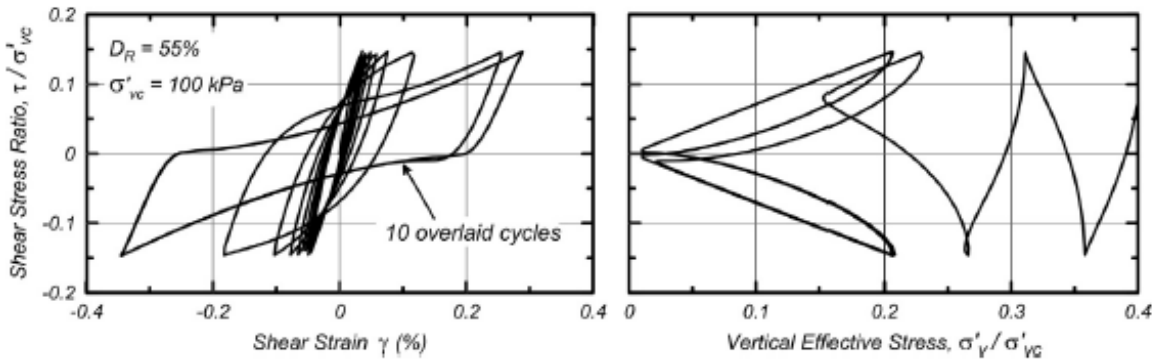

Figure 4. Undrained cyclic DSS loading response without considering the effects of fabric terms. Taken from [71]

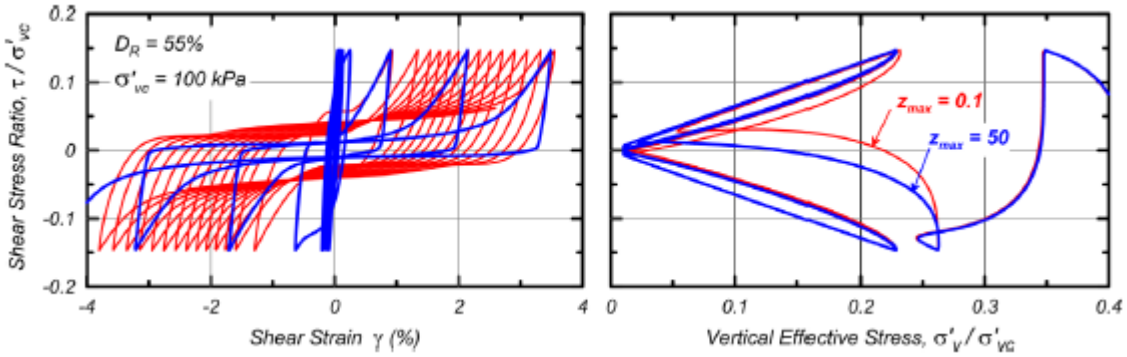

Figure 5. Undrained cyclic DSS loading response considering the effects of fabric terms. Taken from [71]

Another type of constitutive models are the multiple surfaces models. Firstly, developed in 1985 by Prevost [73], who formulated a simple plasticity constitutive model for cohesionless soils, based on the simple multi-surface J2 theory [74] [75] . According to Prevost [73] the model has been tailored to retain extreme versatility and accuracy of the simple multi-surface J2 theory, describing observed shear nonlinear hysteric behavior, shear stress induced anisotropic effects and to reflect the strong dependency of the shear dilatancy on the effective stress ratio in granular cohesionless soils. Conical yield surfaces are used for that purpose. Figure 7 presents the conical yield surface of the model in principal stress space and deviatoric plane.

In 2003, Elgamal et al. [76] extended the multi surface plasticity formulation to reproduce cyclic shear strain accumulation and dilative phases resulting from soil liquefaction. The improvement corresponded to the incorporation of a new appropriate flow rule based on experimental observations, changing the characteristics of the model response, to reproduce the salient cyclic mobility mechanisms and exercise more direct control over shear strain accumulation. Also, a new hardening rule was implemented to produce a more efficient numerical performance illustrated in Figure 7.

Later in 2018; Khosravifar, Elgamal and Li [39] updated the latter model by adding new flow rules to produce better results for capturing contraction and dilation in sands by evaluating the model responses under different loading conditions. Also, the model incorporates a non-associative flow rule and a strain space mechanism to simulate cyclic mobility response features. Figure 8 presents an example of the response of the last version of the model in undrained cyclic shear loading.

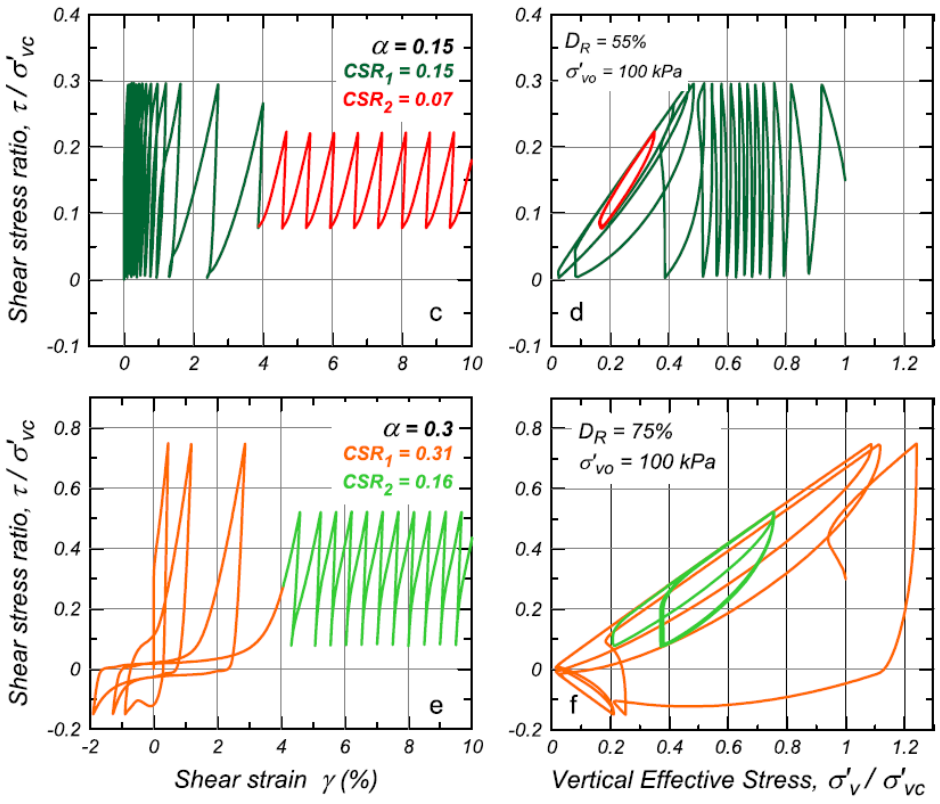

Figure 6. Undrained irregular cyclic DSS loading responses for D_R=55% and D_R=75% with vertical effective consolidations stress of 100 kPa using PM4Sand Version 2. Taken from [72]

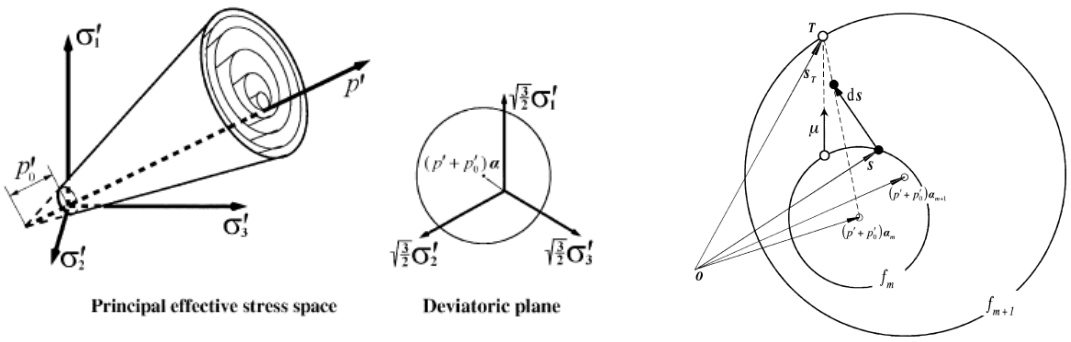

Figure 7. a) Conical yield surface in principal stress space and deviatoric plane. Taken from [76] b) Deviatoric hardening rule proposed by Elgamal et al [76]. Taken from [76]

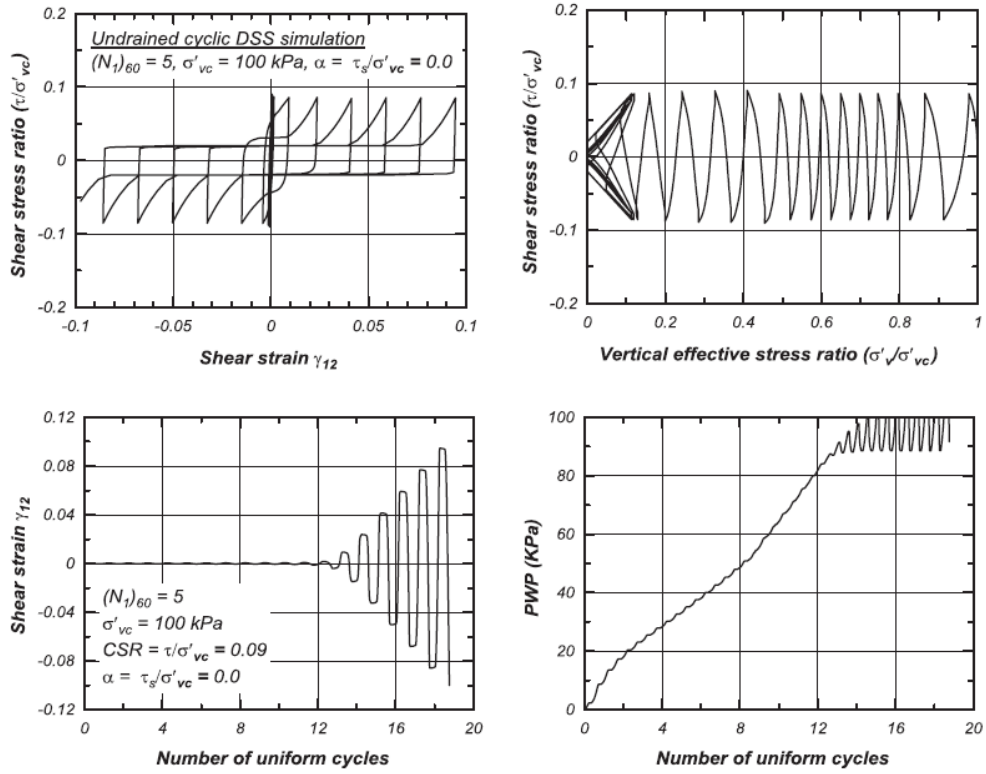

Figure 8. Example model response in undrained cyclic simple shear loading. a) Shear stress ratio (τ/σ'_{vc}) vs. shear strain (γ_{12}). B) Shear stress ratio (τ/σ'_{vc}) vs. vertical effective stress ratio (σ'_v/σ'_{vc}) c) Shear strain (γ_{12}) d) Pore water pressure vs. Number of uniform cycles. Taken from [39]

2.3. Soil variability

Soil is formed in different deposition environments, which causes their properties to vary from one point to another. Therefore, the soil is considered as an heterogenous material. This

variability is an important condition because it is one of the major contributors to uncertainty in geotechnical analyses [77]. Moreover, it has a big influence in the soil response to external loading. For this reason, researchers [34] [78] [29] [79] have considered that relying on methods that uses average measures of the soil properties may not be the most accurate approaches. As a result, stochastic analysis that considers soil heterogeneity have been implemented to achieve a more realistic methodology to evaluate the soil response considering its high level of uncertainty. This approach uses estimation and simulation techniques to consider the variability of available data and to estimate the frequency at which values of interest are likely to be exceeded [77]. Valuable insights can be achieved by using this method in different phenomena such as liquefaction.

According to Lacasse and Nadim [80] there are several ways to classify the existing types of soil variability. One way is based on the source of variability, divided into aleatory and epistemic variability. Aleatory variability is related to the inherent variability of the physical environment and represents the natural randomness of a variable. Examples of aleatory variability are the temporal variation in the peak acceleration of a design earthquake with a given return period and the spatial variation of a soil parameter within a nominally uniform geological layer. This variability cannot be eliminated. On the other hand, epistemic variability refers to uncertainty due to the lack of knowledge on a variable, which involves measurement variability, such as imperfections of an instrument, statistical variability, and model variability, due to idealizations made in the physical formulation. This variability is caused by the limited number of observations. Unlike aleatory variability, epistemic variability can be reduced or eliminated by improving measurement methods or calculation methods.

Another way to categorize variability is according to its nature. When the value of a variable depends on its position, it can be classified as spatial variability. Different properties can be placed in this category, such as density and permeability [31]. Several authors have proposed different methods to measure spatial correlation, which is a measurement assigned to variables that are spatially related, e.g. Method of Moments, Maximum Likelihood and Local Average Theory [81] [82] [83]. Additionally, to measure the correlation function, Vanmarcke [84] implemented the concept of correlation length. This parameter along with the mean and coefficient of variation produce a better description of the spatially correlated field

[31]. Additionally, another category to classify variability is temporal variability, which describes how random fields changes with respect to time, such as the variability present in the base acceleration time history of a seismic event. [31] Figure 9 presents a brief schematic of the classification of soil variability.

The most popular applications of soil variability in modeling are [29]: (a) *geostatistics*: due to the limited amount of available data in geotechnical exploration, different methods have been implemented for soil properties interpolation. One example of a statistic modeling approach that has been developed is known as *geostatistical kriging*, first developed by mathematicians [85] [86] [87] based on the theory of random processes. This procedure minimizes the estimated variance of the interpolated value with the weighted average of its neighbors. The weights depend on the spatial location of the points of interest for estimation. Several authors have developed different formulations of kriging [88] [89] [90] and Nadim [91] and Lacasse & Nadim [92] have implemented different applications in the geotechnical area. (b) *Reliability-based geotechnical design.* This approach develops geotechnical designs based on the probability of failure, depending on parametric and model uncertainties, allowing the engineer to perform various parametric studies without performing thousands of design checks. Several investigations about reliability design have been developed and it can be found in Phoon et al. [93] [94]

Soil variability have been evaluated in different geotechnical problems such as slope stability, soil-structure interaction, off-shore foundations design and seismic induced liquefaction by several authors using stochastic analyses. The results have shown valuable insights about the effects of evaluating soil variability in geotechnical engineering analysis. A summary of these analyses and results will be described in the following paragraphs.

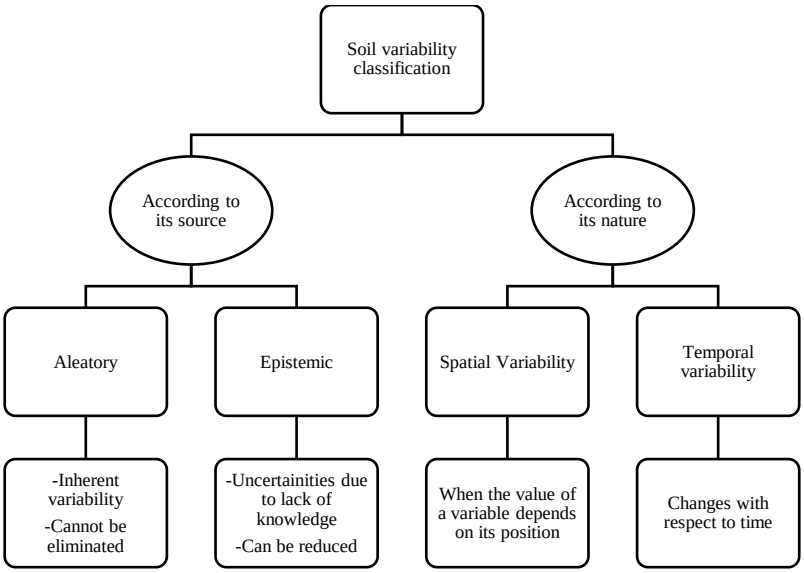

Figure 9. Schematic of the classifications of soil variability

Griffiths & Fenton [30] performed a soil stability analysis addressing the effects of soil variability using the Random Finite Element Method (RFEM). Two type of simulations were performed, the first type was a simple approach where the strength of the slope was treated as a single random variable and the second type of analyses implemented the finite random element method considering spatial correlation and local averaging. The advantages of this method include that it accounts for spatial correlation and averaging, and it does not require priori assumptions related to the shape or location of the failure mechanism. The research showed that simplified probabilistic analysis that ignored spatial variability can lead to unconservative results of the probability of failure. Figure 10 shows the representation of the finite element model created by Griffiths & Fenton.

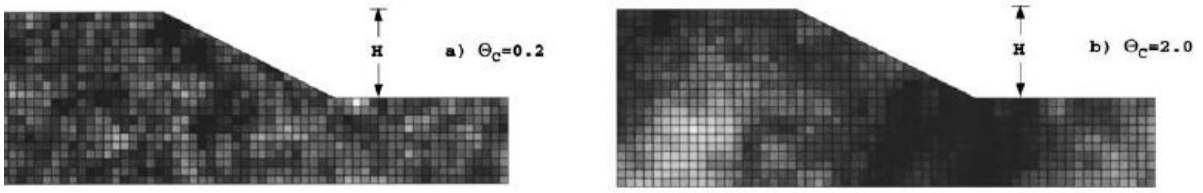

Figure 10. Example of a probabilistic slope stability random finite element model considering spatial variability. Taken from [30]

Soil-structure interaction is also affected by soil variability. Breysse et al. [32] studied the effects of soil heterogeneity in soil-structure interaction systems by developing a finite element

model of a structure resting on a spatially varying soil described with Winkler-type springs. This model was used to represent soil-pavement interaction and soil-railway interaction. The authors concluded that soil variability induces specific problems (e.g., Differential settlements, bending moments, stresses, and possible cracking) that cannot be predicted if the soil is assumed homogenous, which could prevent consequences such as local or global failure.

Furthermore, Popescu et al. [95] analyzed the bearing capacity and differential settlements of a rigid strip foundation on over consolidated clay layer using a nonlinear Finite Element Model in a Monte Carlo simulation framework. It was proven that different sample realizations of random fields to generate the soil properties corresponded to fundamentally different failure surfaces. Through this analysis, it was possible to appreciate the compound kinematics of settlements, which could not be inferred from deterministic bearing capacity calculations. In addition, Fenton & Griffiths [33] developed a probabilistic model to predict the reliability of shallow foundations in the form of excessive and differential settlement in a three dimensional spatially random medium. Figure 11 presents the finite element meshes created to address this problem.

For offshore foundation design the effects of soil variability has also been studied. Nadim [35] presents an overview on how uncertainty and variability of mechanical soil properties are dealt with in offshore site investigation considering its high costs. One alternative is to use reliability tools that considers the uncertainties caused by natural variabilities to establish the representative characteristics of soil properties in offshore foundations design. The author applies these concepts to verify the stability of a platform using the method of spatial averaging by kriging.

Another phenomenon that is influenced by soil variability in geotechnical engineering is seismic liquefaction-induced ground failure. Popescu et al. [95] investigate the effects of soil heterogeneity on the liquefaction potential of a spatially heterogeneous soil deposit subjected to earthquake loading, through different Monte Carlo simulations that were performed using non-normal bivariable random fields and non-linear finite element analyses. Two variables were select to be represented as random fields to model the heterogeneity of the soil: the overburden stress-normalized cone tip resistance and the CPT-based soil behavior classification index. Deterministic and probabilistic analysis were performed to compare the

results. The results showed that for excess pore-water pressure the deterministic analyses yielded unconservative results for low-intensity inputs and slightly greater values for high-intensity loading. Also, probabilistic simulations were used to obtain the maximum liquefaction-induced ground settlement. Moreover, results suggested that a 2D model and the deterministic model in which spatial variability is neglected may lead to unconservative results.

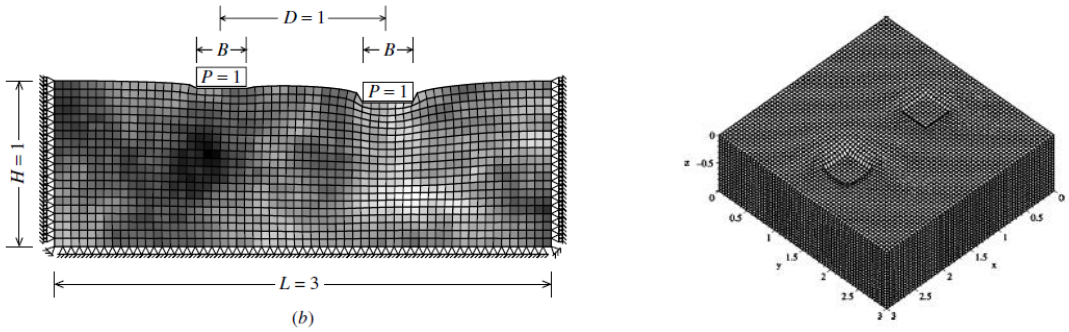

Figure 11. a) Cross section of the finite element mesh for two footings founded on a spatially heterogenous soil b) 3-D visualization of the finite element mesh. Taken from [33]

ElGhoraiby & Manzari [31] evaluated the effects of soil heterogeneity in lateral spreading of mildly sloping liquefiable ground using non-linear finite element modeling couple with Monte Carlo simulations. In this research, two sources of variability were considered: inherent spatial variability of the soil density in terms of void ratio. The second source is the variability in the magnitude and frequency of the base motion. The stochastic analyses were performed based on the variabilities observed in the centrifuge tests conducted for the Liquefaction Experiments Analysis Projects (LEAP) LEAP-GWU-2015 and LEAP-UCD-2017. The results exhibit that the prediction of lateral displacements of the soil is more sensitive to base excitation variability than to variability in soil density. Also, it was proved that stochastic analysis can predict the observed variability of the centrifuge experiments when the different sources of variability are carefully accounted for. It was also demonstrated that simulations that does not address variability when the soil is significant heterogenous can be compromised. Figure 12 presents the finite element model mesh addressing soil variability in terms of void ratio.

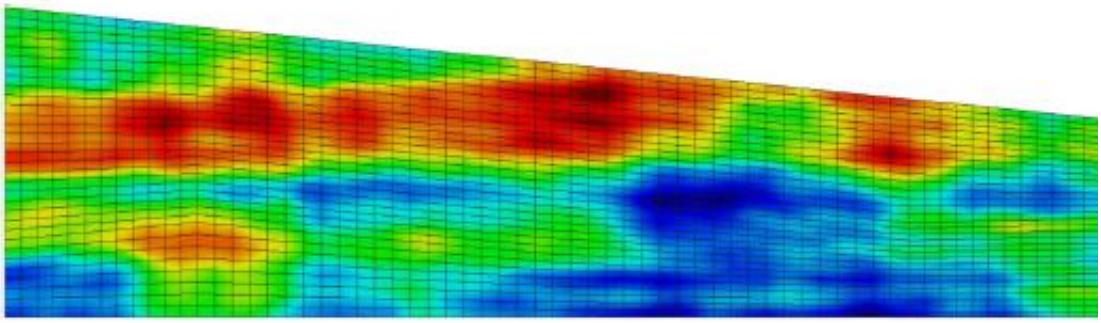

Figure 12. Soil variability in terms of void ratio for a mildly sloping ground of liquifiable soils. Taken from [31]

In outline, soil variability is an important variable because soils are not homogenous materials, and its heterogeneity introduces more uncertainty to numerical models. As it was mentioned, several investigations have evaluated soil heterogeneity in different geotechnical problems such as sloping ground, soil-structure interaction, offshore pile design and liquefaction. The results suggest that probabilistic simulations accounting for soil variability can lead to estimations that could not be achieved using uniform and deterministic analysis, such as the prediction of failure surfaces, failure mechanisms and avoid overestimated designs. Subsequently, when the sources of variability are carefully modeled, reliable predictions can be obtained from probabilistic simulations where in-situ investigations have high costs. For this reason, producing and validating probabilistic simulations that addressed soil variability is a useful computational tool that can be used to predict the soil response taking into consideration the uncertainties presented in geotechnical systems.

3. Theoretical Framework

3.1. Stochastic analysis

For most of geotechnical engineering problems field exploration and experimental data are expensive and require a long amount of time. Additionally, a deterministic solution cannot always lead to the optimum system design. Thanks to the advances in computational tools, numerical methods have been developed to provide practical solutions that could be implemented to analyze the effects of soil variability. The Finite Element method is a numerical tool that have been used for analyzing different geotechnical systems, which can be combined with statistical methods to provide stochastic analysis for obtaining solutions to static and dynamic problems with stochastic mechanical, geometric and/or loading properties. [31]

Two different approaches that combine finite element analysis with statistical principles have been developed. One of them is the stochastic finite element method (SFEM). SFEM is an extension of the classical finite element method coupled with the stochastic framework that helps to solve stochastic problems using finite elements whose properties are randomly generated. A variety of problems have been analyzed using this method (e.g. Soil, structural and fluid mechanics, and heat transfer) [96] [97] [98] [99] [100]. The literature presents three different variants of the method [101] . a) the perturbation approach, based on the Taylor series expansion [102] b) the spectral stochastic finite element method SSFEM [103], where the responses are represented using a series of Random Hermite Polynomials and c) The Monte Carlo Simulation (MCS) [104], which solves a deterministic problem several times using different random input parameters that follows certain probabilistic distributions. There are three principal steps that should be followed to perform a Stochastic Finite Element analysis: first, a stochastic field accounting the uncertain system properties must be generated, secondly, a stochastic matrix is formulated. Lastly, the response variability is calculated.

On the other hand, the second method presented in the literature is named as Random Finite Element Method (RFEM). RFEM has been developed and implemented for probabilistic geotechnical engineering by Griffiths and Fenton [105]. This method combines the theory of the non-linear finite element analysis with random-field theory. Also, spatial correlation can be added into the finite element mesh. Several problems have been evaluated using this technique, such as slope stability problems [30] [106], bearing capacity [105], calculations of passive earth pressure [107], steady seepage [108] and settlement evaluation [33]. This research implemented a stochastic analysis based on the Random Finite Element Method for the analysis of the retaining wall under study.

3.1.1. Random Fields

According to Vanmarcke [109] an experiment can be defined as "*an act or operation designed to discover some unknown truth or effect*" and their outcomes can be described in terms of *random variables*. A random field is a set of random variables ***X(t),*** which have locations in n-dimensional space, such as coordinates or parameters. The collective outcome of all experiments comprising the random field is denoted by ***x(t).*** The random variables can be discrete or continuous. When the random variable is discrete, the random field is termed "discrete state". The random field is a "continuous state" when it is formed by continuous random variables.

Powell [110] defines random fields theoretically as follows "For a two-dimensional domain $D \subset \mathbb{R}^2$, a (real valued) *random field* $Z(x): x \in D$, also written $Z(x, \omega)$,accounts for real-valued random variables on a probability space $(\Omega, \mathcal{F}, \mathbb{P})$. That is, for each $x \in D, Z(x): \Omega \rightarrow \mathbb{R}$ is a random variable. The random field is second order if Z(x) has finite variance for each $x \in D$ and for such fields, the mean function can be defined as $\mu(x) = \mathbb{E}[Z(x)]$ and the *covariance* function as

$$C(x, y) = Cov\,(Z(x), Z(y)) = E[(Z(x) - \mu(x))(Z(y) - \mu(y))], \quad x, y \in D.$$

For a fixed $\omega \in \Omega$, the realizations correspond to a deterministic function $f: D \rightarrow \mathbb{R}$ defined by $f(x) \coloneqq Z(x, \omega)$ for $x \in D$. Therefore, a realization represents one possibility for the quantity Z as a function of x. Thus, to perform a statistical analysis, multiple realizations

of $Z(x,\omega)$ are needed if Z (x,ω) stands for an input in a mathematical model". Figure 13 presents different realizations of a random field to illustrate this concept.

The key properties of a random field are [109] a) *homogeneity*, that occurs when all the joint probability distribution functions remain the same when the set of locations $t_1, t_2, \dots, t_M$ is translated in the parameter space. b) *Isotropic* if the joint probability density functions remain the same when the constellation of points $t_1, t_2, \dots, t_M$ is rotated in the parameter space. c) *ergodic* when all the information about its joint probability distributions can be obtained from a single realization of the random field including its statistical parameters.

Some types of random fields correspond to *stationary random fields*, where $\mu(x)$ is constant and the covariance depends on ***x-y***, and *isotropic random fields*, where the covariance depends on $\|\boldsymbol{x}-\boldsymbol{y}\|_2$.

Different random-field generator algorithms have been developed. The most common are the moving average (MA) methods, covariance matrix decomposition, Discrete Fourier Transform (DFT), Fast Fourier transform (FFT), circulant embedding, Turning-bands method (TBM) and local average subdivision (LAS) method. More information regarding these methods can be found in Fenton & Griffiths [34].

3.1.1.1. Gaussian random fields

Powel [110] defines a *Gaussian Random Field* as a second-order field where the vector of random variables $\boldsymbol{Z} = [Z(x_1), Z(x_2), \dots, Z(x_N)]^T$ is described with the multivariate Gaussian distribution for any $x_1, \dots, x_N \in D$. That is, $Z \sim N(\mu, C)$ where the mean vector, μ , and the covariance matrix ,C, have entries $\mu_i = \mu(x_i)$ and $c_{i_j} = C(x_i, x_j), i, j = 1, \dots, N$, where C is a symmetric and nonnegative matrix by definition. Figure 13 shows examples of different realizations of zero mean Gaussian Random Fields performed by Powell [110] as an illustrative example for the reader.

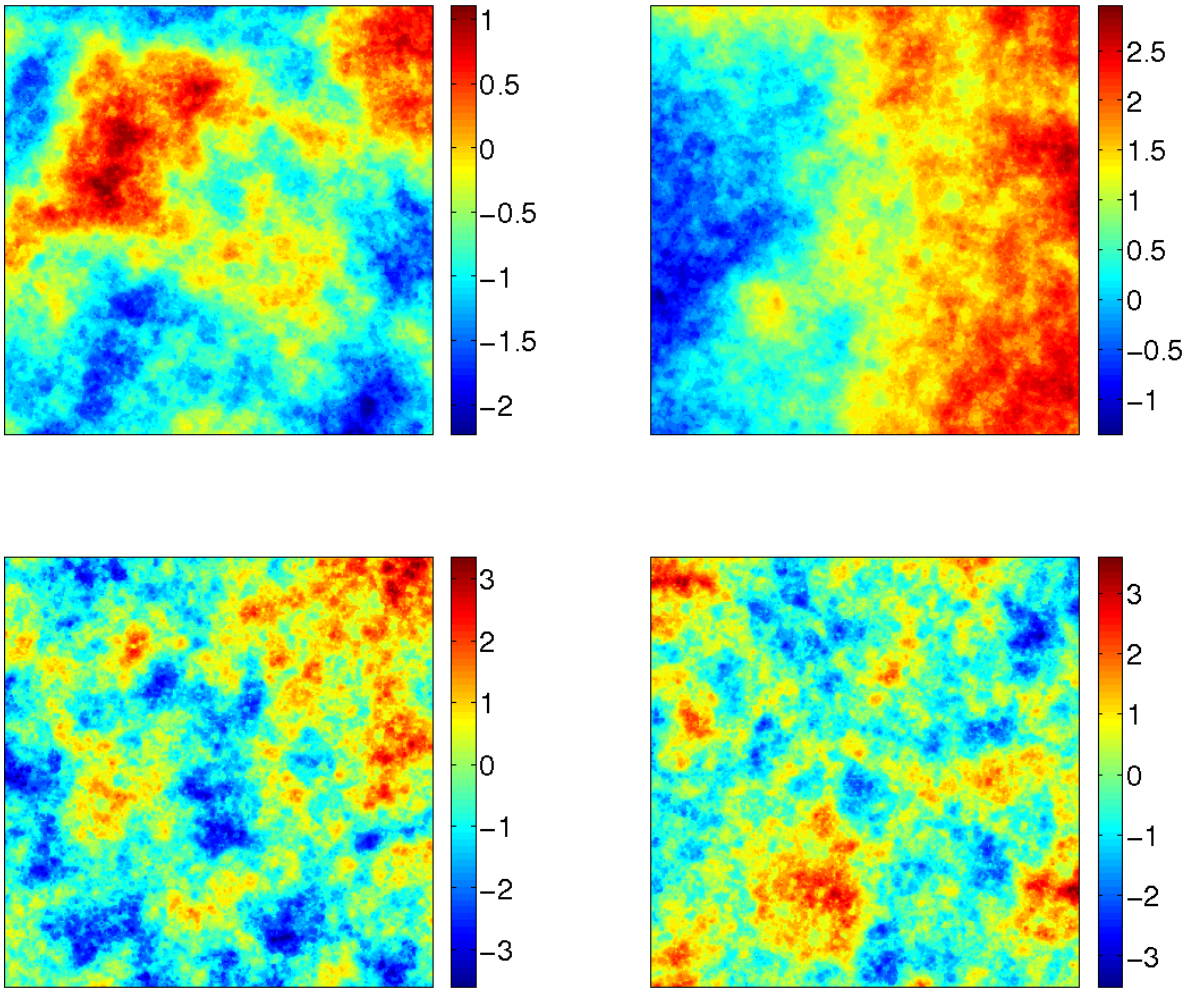

Figure 13.Example of different realizations of a mean zero Gaussian Random Field on a two-dimensional domain (D= [0,1]× [0,1]). Taken from [110]

This work considers the relative density, D_R, as a multivariate gaussian process to model the spatial variability presented in soils. This assumption is based on the studies reported by Huber [79] , in which he explains that the simplest way for describing spatial variability is by a multi-Gaussian distribution. Additionally, Lacasse and Nadim [80] propose that moisture-density characteristics, such as natural water content, w_n, total unit weight, γ, dry unit weight, γ_d, buoyant unit weight,γ_s, relative density, D_R, specific gravity, G_s and the degree of saturation, S, can be modeled as a Gaussian variables.

3.1.1.2. Spatial correlation length

This research models the soil as a spatial correlated field because, as point out before, geological materials come from weathering processes and residual soils that are transport to

their present locations by physical ways. Also, they are subjected to different stresses, pore fluids and physical and chemical changes, leading to variations of their properties from place to place within a certain distance [79].

Fenton & Griffiths [34] describe the *correlation length, θ*, which can also be named as the *scale of fluctuation,* as the distance within which points are significantly correlated. Consistently, two points are uncorrelated when they are separated by a distance more than the *correlation length, θ.* The *correlation length θ* can be considered as a measurement of the variability of a random field. Vanmarcke [109] presents the mathematically definition of the *correlation length θ* as the area under the correlation function ρ according to Equation 1, where $\boldsymbol{\tau}$ corresponds to the separation between two variables.

$$\boldsymbol{\theta} = \int_{-\infty}^{\infty} \boldsymbol{\rho}(\boldsymbol{\tau})\boldsymbol{d\tau} = \mathbf{2}\int_{\mathbf{0}}^{\infty} \boldsymbol{\rho}(\boldsymbol{\tau})\boldsymbol{d\tau} \qquad \text{Equation 1}$$

The spatial correlated variability is represented using a multivariate Gaussian process described by the probability density function presented in Equation 2.

$$fx(\boldsymbol{x}) = \frac{1}{\sqrt{(2\pi)^k|\boldsymbol{C}|}} exp\left\{-\frac{1}{2}(\boldsymbol{x}-\boldsymbol{\mu})^T C^{-1}(\boldsymbol{x}-\boldsymbol{\mu})\right\} \qquad \text{Equation 2}$$

Where, the random variables contained in vector $\boldsymbol{x}$ has a mean of vector $\boldsymbol{\mu}$ and the covariance matrix $\boldsymbol{C}$ can be calculated using Equation 3.

$$\boldsymbol{\mu} = E[\boldsymbol{X}];\ \boldsymbol{C} = E[(\boldsymbol{X}-\boldsymbol{\mu})(\boldsymbol{X}-\boldsymbol{\mu})^T] \qquad \text{Equation 3}$$

When assuming a stationary random process, the covariance matrix is independent of its position and it can be expressed in terms of the correlation coefficient $\boldsymbol{\rho}$, as follows.

$$\boldsymbol{C} = \boldsymbol{\rho}\boldsymbol{\sigma}_{\boldsymbol{x}}^{\mathbf{2}} \qquad \text{Equation 4}$$

In this research, a Gaussian correlation function was used to model the correlation coefficient according to Equation 5 [111] .

$$\rho_{(\boldsymbol{x_i},\boldsymbol{x_j})} = \exp\left(\frac{-|\boldsymbol{\tau}|^{\mathbf{2}}}{\mathbf{2}\boldsymbol{\theta}^2}\right) \qquad \text{Equation 5}$$

Where ρ is the correlation coefficient, θ the correlation length and $\boldsymbol{\tau}$ indicates the separation between two points. Figure 14 illustrates this concept by showing different examples of a mean

cero Gaussian Random Fields, with a correlation length of $\theta^2 = 1/10$ for the figures located at the top and a correlation length of $\theta^2 = 1/1000$ (bottom). It can be noted that a long correlation length produces contours with less variation than a short correlation length, because a short correlation length represents more variability between the variables in the random field.

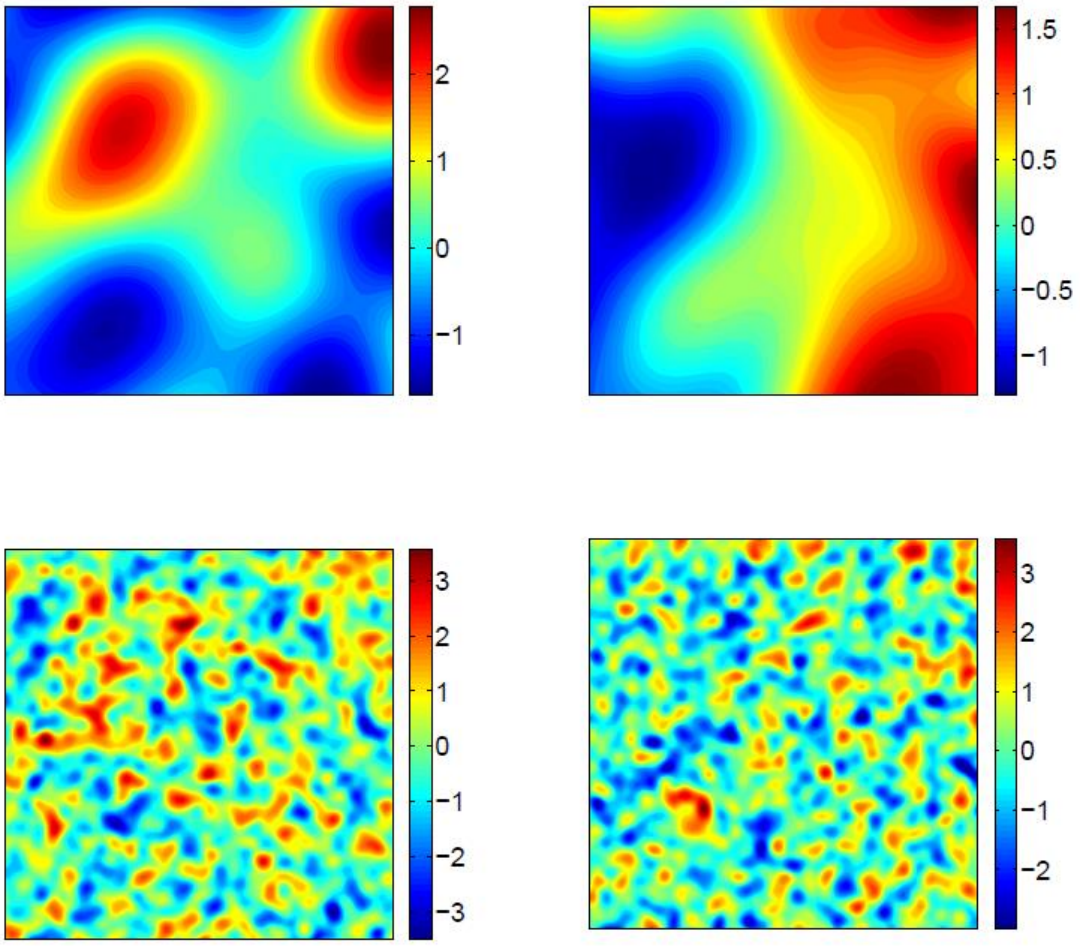

Figure 14. Different realization of a mean zero Gaussian Field with correlation length $\theta^2 = 1/10(top)$ and $\theta^2 = 1/1000(bottom)$. Taken from [110]

4. Methodology

Considering the devasting effects that liquefaction have caused and the numerous constitutive models that have been proposed for different authors to predict its effects, there is an urgent need for producing more experimental and reliable procedures to calibrate and validate the existing models. This research aims to evaluate the advantages and limitations of a pressure-dependent multi-yield surface model referred to as "PDMY02" Model [46] [37] [38] [39] using the resulting data from centrifuge testing produced in the Liquefaction Experiments and Analysis Project LEAP 2020. Furthermore, a stochastic analysis was performed to evaluate the effects of the spatial variability of the soil in liquefaction modeling.

The research presents two type of approaches. The first approach corresponds to the deterministic evaluation of the problem. This part is composed by the calibration and validation of the finite element model using the centrifuge experiments produced by LEAP 2020. The second approach evaluated the problem using a stochastic analysis based on the Random Finite Element Method. In this section, the methodology implemented to achieve the aims of the research will be described. Figure 15 presents a brief description of the steps that were followed.

Firstly, to elaborate the Finite Element deterministic model, the parameters of the pressure-dependent multi-yield surface constitutive model "PDMY02" were calibrated using the results of cyclic triaxial experiments for Ottawa F-65 Sand, produced by Andrew Vasko [1], ElGhoraiby, Park and Manzary [2] and Ochoa-Cornejo et al [3] for four different relative densities (D_R), 55%, 65%, 75% and 90%. According to the LEAP2020 project specifications, the centrifuge experiments were conducted using one of the first three relative densities in the top layer of the soil deposit and all the experiments had a dense layer at the bottom, with 90% of relative density. The constitutive model was calibrated using cyclic triaxial experiments

because it was proven that they show better adjustments than simple shear tests to predict the dynamic behavior of the soil [44].

Afterwards, the numerical model was implemented in the software OpenSees using the finite elements method to perform the nonlinear simulations. The model was composed by a top layer of Ottawa F-65 sand retained by a sheet-pile. Behind the sheet-pile, the soil layer had a thickness of 4 meters and a length of 13.00 meters in prototype scale. Meanwhile, in front of the sheet-pile the layer had 1 m of thickness and a length of 7.00 m. Underline this layer, there was a dense layer of 90% relative density and 1m thickness. The schematic of the model is presented in Figure 1. The numerical model was developed according to the guidelines provided to the numerical modelers team in the LEAP-2020 project. The results of the finite element model were validated using the centrifuge experiments from the project. Thus, it was possible to identify the capabilities and limitations of the constitutive model to simulate the soil response when subjected to seismic loads.

The second approach of the research involves the stochastic analysis of the same model taking into consideration the spatial soil variability. To perform this analysis, the relative density (D_R) was chosen to be a random variable, following a gaussian multivariate random process. This assumption is supported by the findings of Lacasse & Nadim [80] and Phoon & Kulhawy [78], who suggested that the probability distribution function for relative density(D_R) is a normal distribution. Additionally, a spatial correlation function was introduced to represent the relationship between the variables of the random field. This function indicates that the values on the random field are correlated to one another according to the spatial correlation length, θ, discussed previously. The Gaussian Random Fields were generated using a function from the NumPy [112] library named as "multivariate.random_normal" [113] [114].

To describe the Random Fields, the relative density(D_R) was modeled with a mean of 65% for the looser layer of the model and a mean of 90% for the dense layer. After the generation of the Random Fields, the results were mapped out into the Finite Element Mesh using their coordinate system. As a result, it was possible to assign to each element of the finite element model a gaussian random value for the relative density (D_R). Further, considering that one of the limitations of the constitutive model "PDMY02" is that it does not address for changes in the relative density implicitly, the function SPLINE [115] in MATLAB [116] was used to

interpolated the parameters of the constitutive model for each corresponding value of the relative density (D_R) in the random field, based on the calibrations made for the three different relative densities (55%, 65%, 75% and 90%).

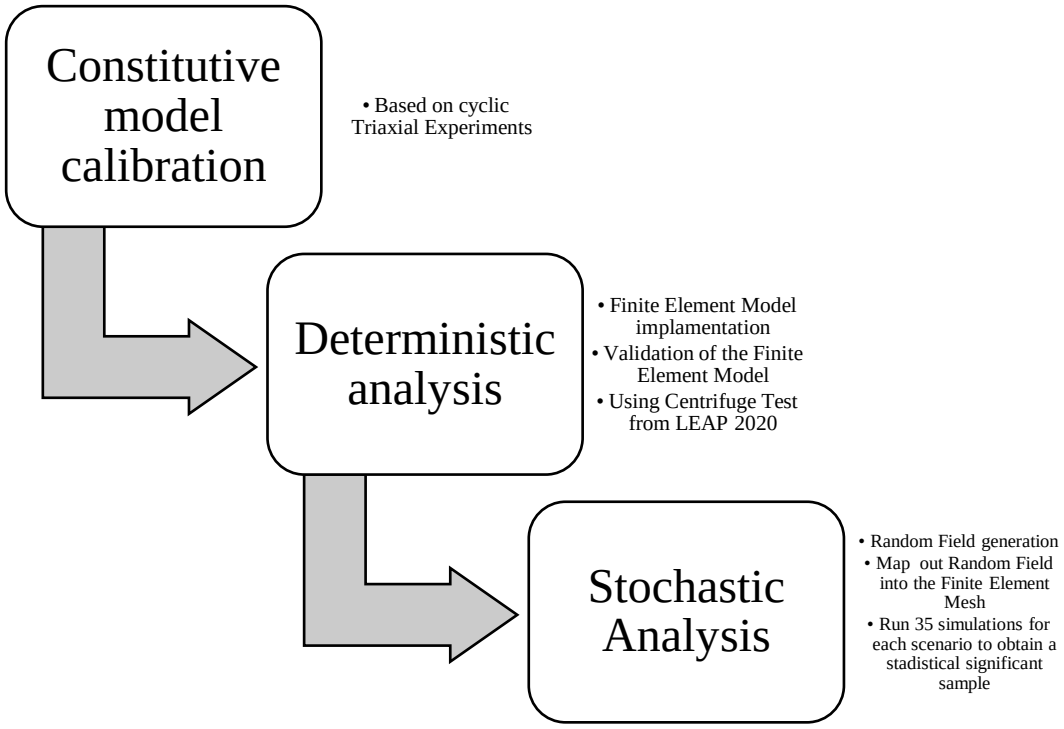

Figure 15. Description of the implemented methodology

Lacasse & Nadim [80] reported the probability distribution, the mean and coefficient of variation for different soil properties from different literature data considering several sources of uncertainty due to soil properties, test methods, stress conditions, stress history and testing errors. For the Relative Density, D_R, the coefficient of variation **(C.V.)** is reported to be ranging from 11%-36% when it is directly calculated. When the value of relative density, D_R, is calculated indirectly from SPT tests, the **C.V.** is between 49%-74% [78]. Additionally, Kutter et al. [117] reported a coefficient of variation **(C.V)** for the relative density of 26% based on the observed range of variation of LEAP-GWU-2015. In the LEAP-UCD-2017 version, the relative density (D_R) was reported with a coefficient of variation **(CV)** of 15 % according to ElGhoraiby & Manzari [31]. Following these reported values, two scenarios between these ranges were chosen to perform the probabilistic analysis. The first scenario corresponds to the conditions that are expected in experimental

tests and the second scenario represents the conditions expected in situ for the value of relative density.

The first scenario models the relative density as a multivariate gaussian distribution with a coefficient of variation (CV) of 6%, which corresponds to a standard deviation (σ) of 4%. The second scenario also models the relative density as a multivariate gaussian distribution, but a coefficient of variation (CV) of 15% is used, for a standard deviation of (σ) 10%. In addition, three different values of the spatial correlation length were analyzed, R=0.7m, R=3.5m and R=7m, for each scenario. These values were arbitrarily chosen, since we do not have detailed information about the soil condition, but they represent a short, medium, and large distance of the correlation length. 35 simulations were performed to obtain a statistically significant sample for a total of 210 simulations. Figure 16 shows a schematic of the simulations performed. The results were analyzed in terms of spectral accelerations, acceleration time history, excess pore-water pressure, vertical settlements, and lateral displacements. Finally, conclusions and remarks based on the findings of this research are presented.

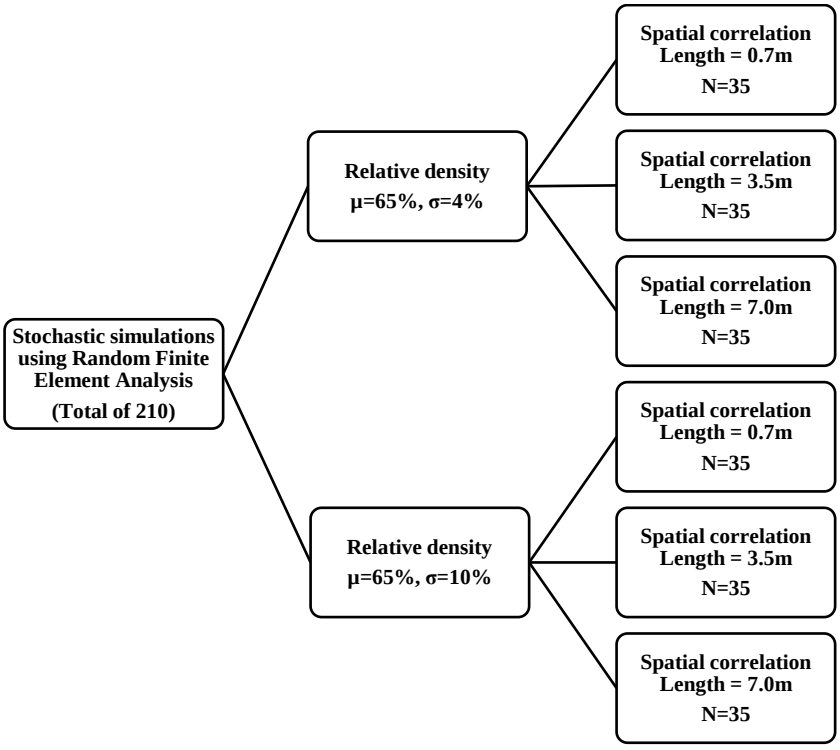

Figure 16. Schematic of the performed numerical simulations for stochastic analyses.

5. Model Setup

5.1. Finite Elements Model Description

The description of the finite elements model is taken from Mercado et. al [44] . The finite elements software OpenSees [118] was used to perform the nonlinear simulations. The model was developed in 2 dimensions and plane-strain conditions were assumed. Two material types were used: a pressure dependent multi-surface plasticity constitutive model was assigned to simulate the soil, while the sheet pile was simulated using an elastic material.

To simulate the soil, Four-noded plane-strain elements were used to simulate the dynamic response as a solid-fluid fully coupled material. In OpenSees they are known as FourNodeQuadUp [38], which are based on Biot's theory of porous medium. The nodes of these elements have 2 degrees of freedom for solid displacement and 1 degree-of-freedom for fluid pressure.

The soil mass was simulated by 1274 plane-strain elements and 1383 nodes and the sheet pile was represented using 20 two-noded elastic beam elements as presented in Figure 17. All the simulations were made in prototype units. For the deterministic predictions, the first meter bottom of the soil was assigned with properties of a dense material corresponding to a relative density of 90%. Meanwhile, the rest of the elements were assigned properties of a medium-dense material, corresponding to relative densities of 55%, 65% and 75%. For the probabilistic simulations, randomly normal spatial correlated properties were assigned to each element.

As it is shown in Figure 17, the bottom boundary of the model has undrained conditions, horizontal and vertical directions are initially constrained. For the horizontal surfaces, free drainage conditions were applied at both left and right sides. To simulate the horizontal pressure caused by water, a vertically increasing distributed horizontal pressure was applied to the sheet pile. Also, the effects of the water resting over the soil were simulated applying a

mechanical vertical pressure and a pore-water pressure of 29.43 kPa (3m*γ_w) to the surface nodes.

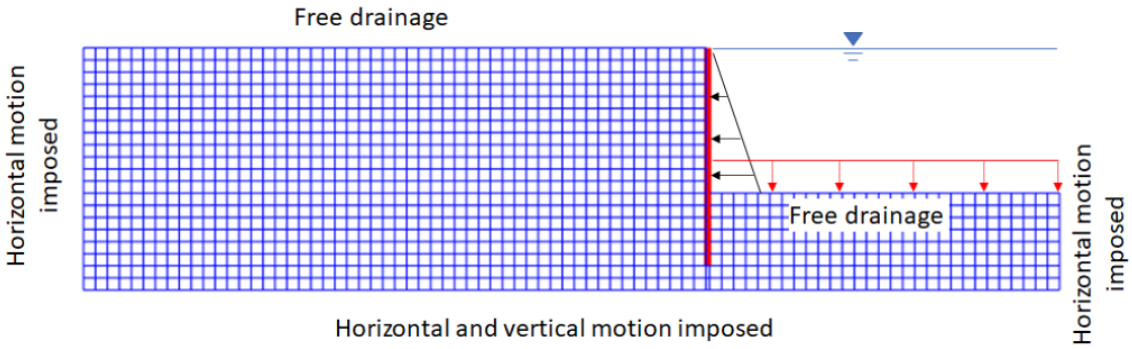

Figure 17. Finite element mesh. Taken From [44]

The interaction between the soil and the sheet pile is presented in Figure 18, it was modeled using zero-length elements according to the following directions:

- The interaction in the normal direction was represented using a uniaxial elastic material (uniaxialMaterial ENT in OpenSees), restraining the tension forces. To simulate a nearly rigid normal interaction between soil and wall, an arbitrary high value for the compressive normal stiffness was used (500.000 kPa).
- The interaction in the tangential direction was modeled using an elastic perfectly plastic uniaxial material (uniaxialMaterial Elastic in OpenSees), which behaves as an elastic material up to certain level of stress, after which it reaches a perfectly plastic state. The stress at which the material behavior becomes plastic was defines as $f = Ko\sigma' \tan(\delta')$ at each node connection, where σ'accounts for the initial effective vertical stress at the node location, Ko represents the coefficient of vertical stress, assumed as 0.5 and δ' is a coefficient of the soil-wall friction, which was assumed as 10°. This approach leads to a soil-wall tangential resistance that is proportional to the horizontal effective stress. This assumption (which uses an approximated initial value of the horizontal effective stresses) should offer a reasonable approximation of the interaction, even though the true horizontal effective stress for the soil adjacent to the wall varies with time as the system is excited.

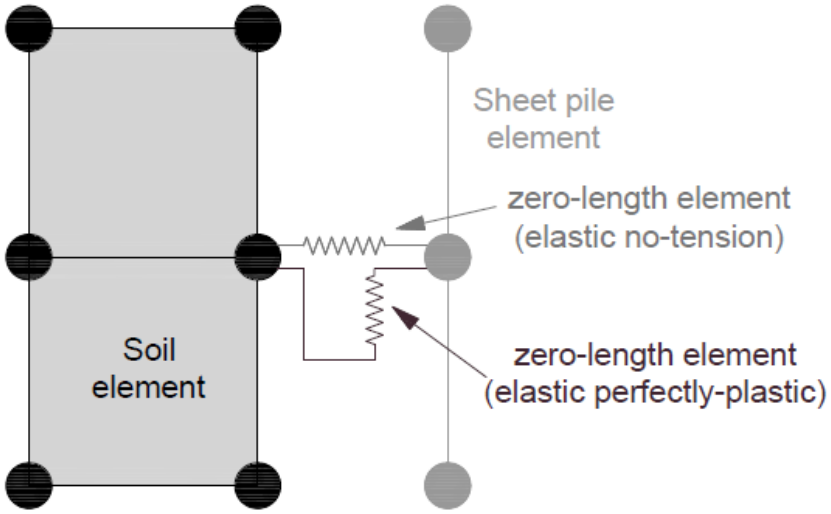

Figure 18. Soil- Wall interaction. Taken from [44]

For the dynamic stage of the simulation, horizontal and vertical input motions were imposed at the base of the model. Only the horizontal component of the input motion was imposed at the lateral boundaries.

5.2. Solution Algorithm and Assumptions

Initially, an elastic step was used to prior the dynamic excitation of the system. In this step, the material configuration was set to behave elastically as gravity loads were applied to the system. To dissipate pore-water pressure, the system was able to drain for a certain amount of time. Also, in this initial stage, the soil permeability of all elements is initially set to 1.0m/s for rapid consolidation. Afterwards, the permeability of the whole model was updated to 1e-4 m/s. Prior to the application of the base excitation, the material behavior was changed to plastic.

A Krylov Newton algorithm was used for the dynamic analysis. This algorithm is based on a Krylov subspace accelerator that accelerates the convergence of the modified Newton method [119]. The penalty method was implemented to carry out boundary conditions, the penalty value of 1e18 was used. The initial time step was 0.005 seconds with a tolerance for energy unbalance of 1e-5. According to modeling practices by Vytiniotis [120], the algorithm can increase the time-step up to a value of 0.01s in case of convergence. Also, in case of non-

convergence after a certain number of iterations, the algorithm can reduce the time step up to a value of 0.0005s.

Rayleigh damping was added to the system, acting mainly on the higher frequencies. The stiffness proportional damping coefficient was set to 0.001 and for the mass proportional damping coefficient a value of 0.0 was used.

5.3. Constitutive model formulation

The simulations were carried out using a multi-surface plasticity model named as Pressure-Dependent Multi-Surface Plasticity Model (PDMY02). The model formulation is made on the original multi-surface plasticity framework formulated by Prevost [73]. In the following section the components of the material plasticity including yielding function, hardening rule and flow rule will be described. More details related to the model formulation are provided by Prevost [74] , Yang and Elgamal [46] , Yang et al [37] and Khosravifar et. al [39].

5.3.1. Yield surface

The yield function is defined by several authors [73] [46] [37] based on the Drucker-Prager criterion [121] using Equation 6, which describes a conical shape multi-surfaces with common apex located at the origin of the principal space as it is shown in Figure 19.

$$f = \frac{3}{2}(s - p\ \propto) : (s - p \propto) - (Mp)^2 = 0 \qquad \text{Equation 6}$$

Where $s = \sigma - p\,\delta$ refers to the deviatoric stress tensor, σ is the Cauchy effective stress tensor, δ is a second-order identity tensor, $p = \left(\frac{1}{3}\right)\tau_r\ \sigma$ is the effective mean confining stress, α is a back-stress ratio tensor and M is a parameter use for describing the size of the yield surface.

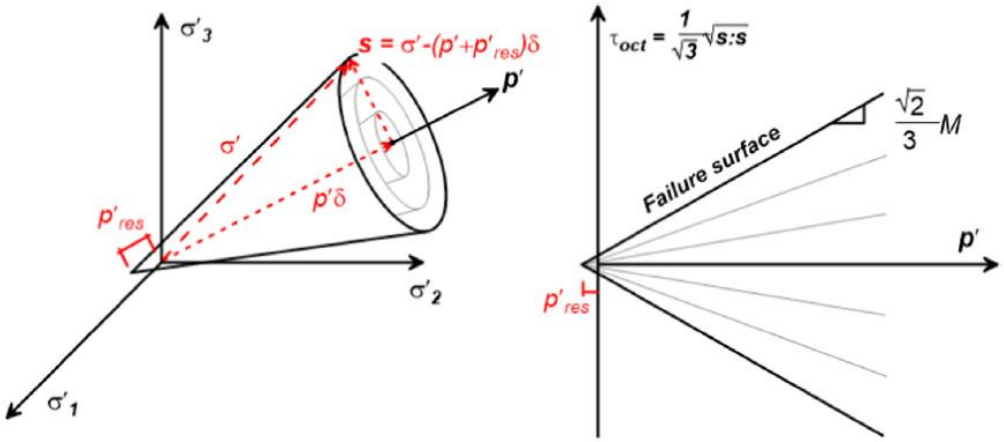

Figure 19. Conical multi-surface yield criteria in principal stress space. Taken from [39]

To calibrate the plastic hardening rule to different experimental or theoretical data a collection of nested yield surfaces is introduced, each of these yield surfaces are defined by Equation 7. The outermost surface is designated as the failure surface, which size is defined by the parameter M_f using Equation 8.

$$f_m = \left(\frac{3}{2}\right)(s - p\alpha_m) : (s - p\alpha_m) - (M_m p)^2 = 0 \qquad \text{Equation 7}$$

Where m refers to the m^{th}yield surface.

$$M_f = \frac{6\ sin\ \varphi}{3 - sin\ \varphi} \qquad \text{Equation 8}$$

5.3.2. Stress-Strain response

To reproduce the stress-strain response of the material a shear stress-strain backbone curve is used [122] [46] [37]. The original version of the PMY02 model employs a backbone curve defined by a hyperbolic function adopted by Kondner and Zelasko [123] and Hardin and Drnevich [124]. Equation 9 describes a pure shear stress loading at a certain reference confinement p_r.

$$\tau(\gamma) = \frac{G_{max,r}\,\gamma}{1 + \frac{\gamma}{\gamma_{ref}}} \qquad \text{Equation 9}$$

Where τ refers to the shear stress amplitude, γ is the shear strain amplitude, $G_{max,r}$ is the small strain elastic shear modulus and γ_{ref} is a reference deformation.

Equation 10 defines the shear modulus, a stress-dependent variable, at small strains G_{max}

$$G_{\max} = G_{\max,\mathrm{r}}\left(\frac{p'}{p'_r}\right)^d \qquad \text{Equation 10}$$

Where $G_{max,r}$ refers to the shear modulus at the reference effective confining stress (p'_r), d is the stress-dependency input parameter, which is commonly selected as 0.5 for sands [122] and p' is the effective confining stress. The tangent shear modulus is assumed to follow the same confinement dependence rule. Also, the bulk modulus of the soil skeleton, B, is defined according to the following expression.

$$B = 2G_{max}(1+\nu)/(1-2\nu) \qquad \text{Equation 11}$$

Where ν refers to the Poisson's ratio.

5.3.3. Hardening rule

A deviatoric kinematic rule was used according to the proposals of Morz [125] and Prevost [73] to generate the hysteric response. This rule is between the framework of the Mroz concept of conjugate points contact. For drained cyclic shear loading, the model exhibits Masing loading/unloading behavior.

5.3.4. Flow rule

The initial formulations of the original model used the flow rule equations to capture the cyclic mobility mechanism including the accumulation of post liquefaction plastic shear strains and the following dilative phases involved in the soil's response. For this case of study, a new update of the flow rule was used to have better control of the rate of pore-water pressure generation [39].

According to Khosravifar et. Al. [39], in this model, the deviatoric component of the plastic strain increment follows an associative flow rule ($\widetilde{P'} = \widetilde{Q'}$), where $\widetilde{P'}$ and $\widetilde{Q'}$ are the deviatoric components. Meanwhile, the volumetric component of the plastic strain increment follows a non-associative flow rule ($P'' \neq Q''$), $where$ $P''\tilde{I}$ and $Q'\tilde{I}$ are the volumetric components. As a result, $P''$is defined according to the relative location of the stress state with respect to the Phase Transformation (PT) surface, η, $\eta = \sqrt{3(\tilde{s}:\tilde{s})/2}/p'$. Also, η_{pt} refers to the stress

ratio along the PT surface. The value of η and $\dot{\eta}$ determine the contractive or dilative behavior of the material when it is subjected to shear loading.

5.3.5. Contractive phase

Shear induced contraction occurs inside the PT surface $(\eta < \eta_{pt})$ and outside $(\eta > \eta_{pt})$ when $\dot{\eta} < 0$. The contraction flow rule is defined as follows for contractive phase:

$$P" = -(1 - sign(\dot{\eta}) \frac{\eta}{\eta_{PT}})^2 (c_1 + c_2\gamma_d)(\frac{p'}{p_{atm}})^{c_3} \quad \text{Equation 12}$$

Where c_1, c_2 and c_3 are model input parameters that help to adjust the volumetric response by adding flexibility, γ_d is a non-negative scalar that represents the accumulative volumetric strain, which increases by dilation and decreases by contraction [39] [44]. The term γ_d is used to represent fabric damage, as it is observed in experiments.

5.3.6. Dilative phase

Dilation occurs due to shearing outside the PT surface ($\eta > \eta_{pt} and \dot{\eta} > 0$). The original model formulation employed the dilative phase to capture the cyclic mobility and post-liquefaction accumulation of shear strain. In the latter formulation new updates were made to capture he effects of effective overburden stress using the parameter d_3 [39]. For loading associated to a dilative tendency, the flow rule is defined by:

$$P" = (1 - sign(\dot{\eta}) \frac{\eta}{\eta_{PT}})^2 (d_1 + {\gamma_d}^{d_2})(\frac{p_{atm}}{p'})^{-d_3} \quad \text{Equation 13}$$

Where $d_1, d_2 and\ d_3$ corresponds to the model input parameters that controls the dilative tendency and γ_d is an octahedral shear strain accumulated from the beginning of a particular dilation cycle if no significant load reversal happens [39].

As the stress state approaches the PT surface $(\eta = \eta_{pt})$ from below, a permanent amount of shear strain may accumulate prior to dilation, causing minimal changes in shear stress and the effective mean pressure (p). Therefore, the model uses $P" = 0$ during this yielding phase, until a boundary from the deviatoric strain spaced is reached, with subsequent dilation thereafter. This boundary extends when the accumulation of shear strain during the dilation phase exceeds the maximum γ_d the material has ever experienced before. The enlargement of

this strain boundary is controlled by the parameter, *Liq*. Khosravifar et al. [39] and Yang et al. [46] presents the details of this mechanism.

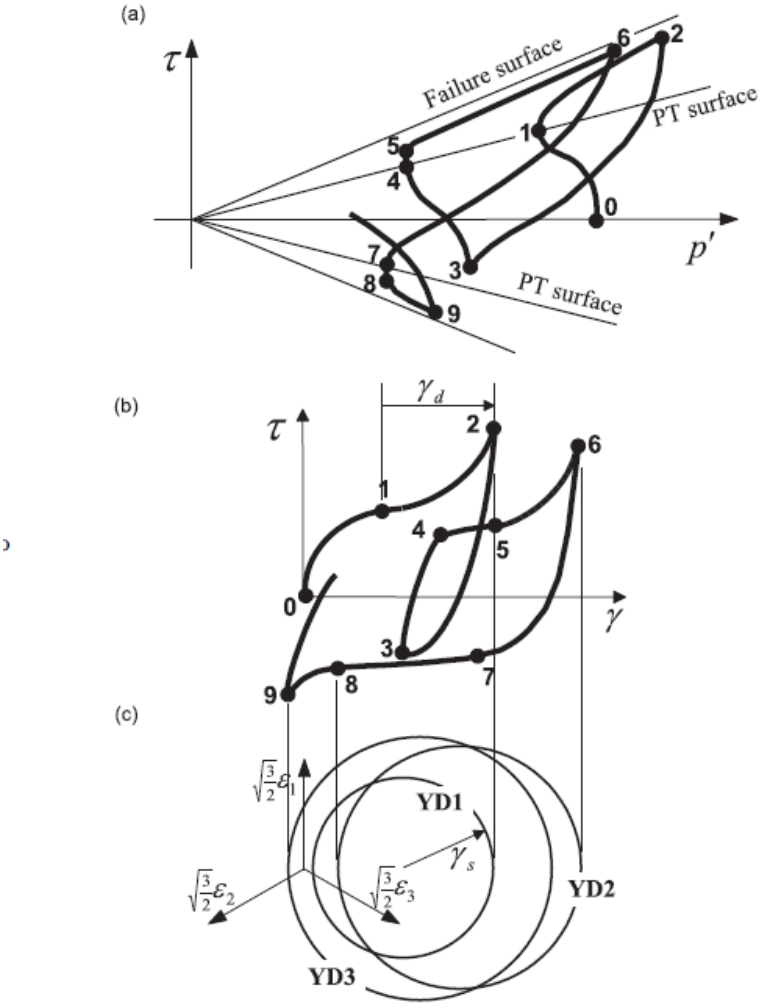

Figure 20. Schematic of the neutral phase in model response showing (a) τ octahedral stress vs. effective confinement p' response. (b) τ octahedral γ strain response and c) configuration of yield domain. Taken from [39]

6. Deterministic vs. Stochastic simulations

6.1. Deterministic simulations

6.1.1. Calibration process

The constitutive model parameters were calibrated using two sets of cyclic triaxial experiments. The first set of experiments was carried out at the George Washington University by Andrew Vasko [1]. The method of sample preparation by dry pluviation with minor tapping on the mold was implemented to achieve the desired density. Additional information of these experiments can be found in [1]. The second set of experimental tests contains the results of stress-controlled cyclic triaxial test on Ottawa F65 sand reported by El Ghoraiby, Park, and Manzari [2]. This data set was used in the calibration phase of LEAP-2017. The calibrations were executed for experiments performed at relative densities of approximately 55%, 65%, 75% and 90%. The calibration process was part of the simulation exercise performed at Universidad del Norte for LEAP-2020. As a result, the following parameters were determined.

The function $G_{max} = G_{max,r}(p/p_r)^d$, with a value of d of 0.5, was used to describe the dependency of the shear modulus with respect to the confinement. To address the variation in relative density, a different value of $G_{max,r}$ was chosen for each relative density, using an arbitrary reference mean confinement pressure p_r =67 kPa, because the PDMY02 model does not account implicitly for changes associated to the variation in relative density.

The reference shear modulus ($G_{max,r}$) was obtained from the reported results by Parra [126] and Alarcon-Guzman et al [127], shown in Figure 21. As a result, the values of $G_{max,r}$ for $D_R = 55\%, 65\%, 75\% \; and \; 90\%$ are 70000 kPa, 75000 kPa, 82000 kPa and 92500 kPa, respectively. After evaluating the shear stress-strain behavior of the soil, the backbone curve of the material was defined using the conventional Kondner and Zelasko hyperbolic function (Equation 9).

The experimental shear stresses were plotted against the vertical effective stresses to identify the values of the failure and phase transformation surfaces. The failure surface was identified as a limiting surface, bounding the maximum achieved shear stresses, while the PT surface was identified at stress locations at which the soil behavior changes from contractive to dilative. Consequently, the angle that defines the failure surface was set as $\varphi = 35°$ for soils with relative density of 55% and $\varphi = 36°$ for soils with relative density between 65% and 75%. The angle defining the PT surface was set as $\varphi_{PT} = 17°$ for soils presenting relatives densities ranging from 55% to 75%. Meanwhile, for soils with relative densities of 90%, the failure surface angle was defined as $\varphi = 40°$ and the PT surface angle was defined with a value of $\varphi_{PT} = 16°$

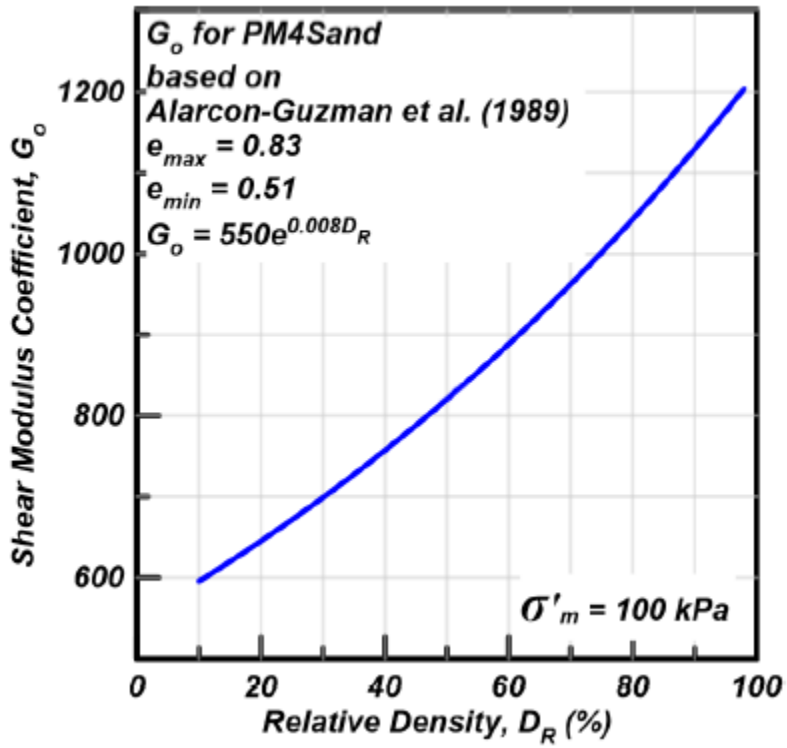

Figure 21. Shear Modulus Coefficient, Go, vs. Relative density for a confinement pressure of 100 kPa. Taken from [126] [127]

The parameters describing contractive and dilative phases (c_1, c_2, c_3, d_1, d_2 and d_3) were adjusted by trial and error to simulate the pore pressure behavior observed in the triaxial tests. The parameter c_1 controls the tendency for achieving plastic contractions for a certain level of plastic deviatoric strains; an increase in c_1, results in a larger tendency. For undrained shear

loading, this leads to an increase in pore-water pressure. Parameter c_2 influences the contraction based on the "fabric damage" experience during a dilative stage according to Equation 13, meanwhile, c_3 adds a dependence of the contraction on the confining pressure [44]. Similarly, the dilatancy of the material is managed by parameters d_1, d_2 and d_3. According to Khosravifar et al. [39] "Decreasing in d_1 reduces the dilative tendency and that, in return, increases the accumulated shear strain per cycle". Parameter d_2, in contrast, influences the dilative tendency based on the octahedral shear strain accumulated in a single dilative cycle (γ_d). Meanwhile, d_3 adds a dependency on the effective confining pressure. Additionally, the parameter, $Liq1$, manages the amount of permanent shear strained reached during the neutral phase.

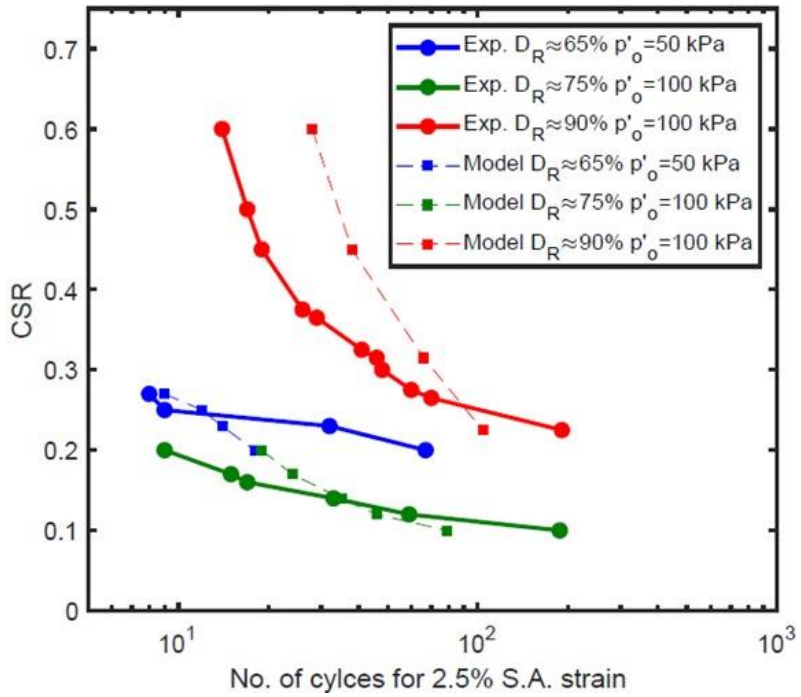

Figure 22. Liquefaction Strength Curves obtained from Cyclic Triaxial tests [2] along with simulated results using the calibration parameters. Cyclic Stress Ratio (CSR) vs No. of cycles for 2.5% S.A. strain Taken from the calibration exercise by Universidad del Norte.

Figure 22 presents a comparison of the liquefaction strength curves between the cyclic stress-controlled triaxial tests on Ottawa F-65 Sand and single element simulations. The data plotted shows the number of cycles until a 2.5% single amplitude of strain is achieved versus the cyclic stress ratio, which is defined as $CSR = \frac{q_{max}/2}{p'_o}$, where q_{max} corresponds to the

maximum deviatoric stress and $p_o{}'$ is defined as the initial effective stress. As can be seen, there is a good match between the simulation results and the laboratory test data for the Ottawa sand F-65 at three relative densities.

In Table 1 the constitutive model parameters used for each simulation are summarized. The columns assigned with the name of the university that performed the centrifuge test (e.g., RPI 12, RPI10 and RPI 13) presents the model parameters of the upper layer of "loose" soil material; Meanwhile, the column named as DENSE presents the parameters corresponding to the lower layer "dense" soil material. The material definition of the dense soil is equal for all simulated experiments.

Table 1. Summary of implemented model parameters

Parameter	**RPI 12**	**RPI10**	**RPI13**	**DENSE**
Relative Density, D_R [%]	55	65	75	90
Sat. mass density ρ [t/m^3]	2.015	2.032	2.051	2.080
Bulk Modulus,	35000	37500	41000	46250
Ref. Conf. pressure, p_r'[kPa]	67	67	67	67
Ref. Shear mod., $G_{max,r}$ [kPa]	70000	75000	82000	92500
Pressure dependence coef., d	0.5	0.5	0.5	0.5
Friction angle, φ [°]	35	36	36	40
Phase transf. angle φ_{PT} [°]	17	17	17	16
Contraction coefficient, c_1	0.41	0.185	0.16	0.14
Contraction coefficient, c_2	20	20	20	20
Contraction coefficient, c_3	0.15	0.15	0.15	0.15
Dilation coefficient, d_1	0.001	0.005	0.005	0.0075
Dilation coefficient, d_2	3.0	3.0	3.0	3.0
Dilation coefficient, d_3	0.5	0.5	0.5	0.5
Damage parameter, $Liq1$	1.0	0.65	0.30	0.065
Number of yield surfaces	20	20	20	20

6.2. Stochastic analysis

6.2.1. Simulation process

In this section a summary of the steps that were followed to develop the stochastic analysis is presented. Four main steps are considered: the first one involves the generation of the random fields that will simulate the spatial correlated variability of soil properties, which for this case of study corresponds to the relative density (D_R). Secondly, the gaussian random field is map out into the Finite Element Mesh to assign to each element a different value of relative density according to their coordinate system. Step three consisted in the interpolation of the constitutive model parameters for each value of relative density based on to the calibrated parameters for each relative density presented in Table 1. The final step consisted in running the simulations 35 times per scenario to obtain a statistically significant sample, for a total of 210 simulations. Figure 23 presents a briefly description of the steps that were followed for the implementation of the stochastic analysis.

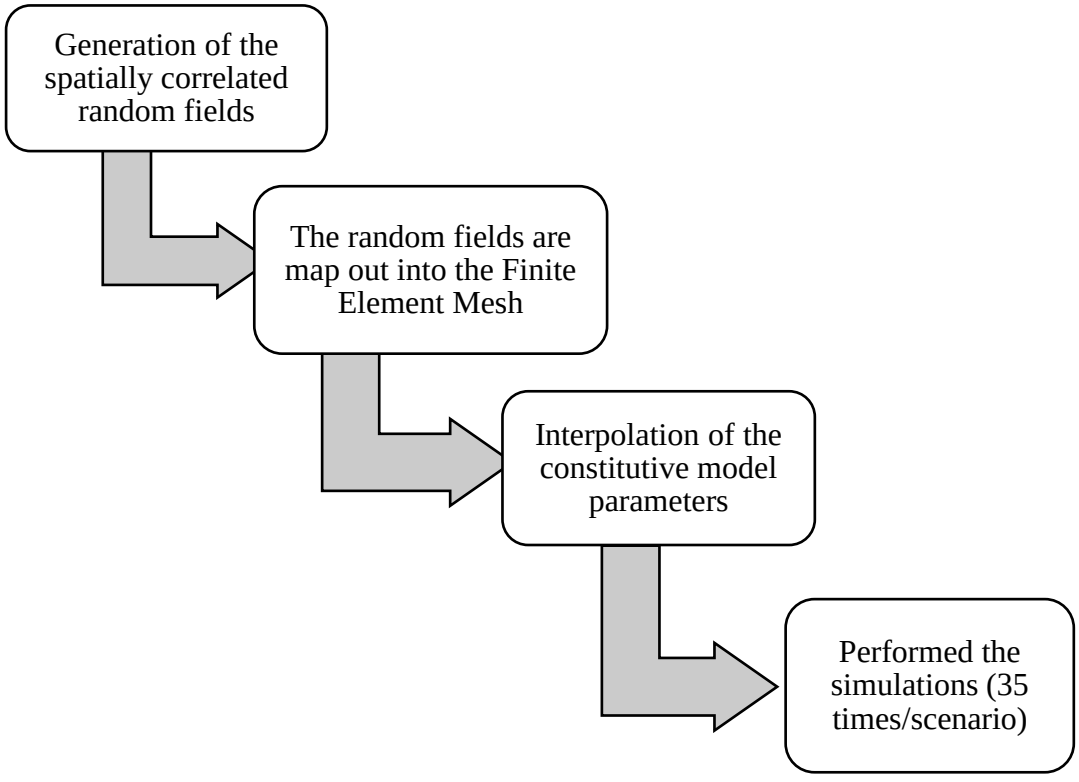

Figure 23.Description of the Stochastic Analysis Methodology

6.2.2. Generation of the random fields

The relative density (D_R) was the soil property that was chosen to be modeled as a Random Field, because there are different factors that can cause spatial changes in this property from one point to another in a soil deposit, such as formation processes, physical and chemical factors, and variations in stress conditions, adding uncertainty to our geotechnical system. Nadim & Lacasse [80]and Phoon & Kulhwahy [78] reported that the relative density (D_R) can be represented by a Gaussian distribution. Considering this, the relative density (D_R) was modeled as a multivariate gaussian correlated random field to represent the spatial variability that a soil deposit can present in situ conditions.

The Random fields were generated using an algorithm developed in Python, which employs a function named as "np.random.multivariate_normal" from the NumPy library [112]. The function needs two arguments: the first one corresponds to a matrix containing the mean (μ) of the data and the second argument is the correlation matrix, which is calculated based on the correlation function of the system (Equation 5) and the standard deviation of the data (σ). The algorithm is included in Section 0.

For this research, the mean of the relative density was chosen as $\mu_{D_R} = 65\%$ for the first layer and for the dense layer the mean value was assigned as 90%. Two values of standard deviation were evaluated, σ_{D_R}= 4% (C.V.=6%) and σ_{D_R}=10% (C.V.=15%), the first value represents experimental centrifuge laboratory conditions according to the observed range of variation reported by Kutter et al. [117] and ElGhoraiby & Manzari [31] for the LEAP-GWU2015 and LEAP-UCD-2017 version. The second scenario represents in situ soil conditions based on the findings of Lacasse & Nadim [80], who reported a coefficient of variation between 11%-36% for the Relative Density D_R, considering different sources of uncertainty due to soil properties, test methods, stress history and testing errors. Similarly, for each standard deviation, three correlation length were studied (R=0.7m, R=3.5m and R=7m). Huber [79] presents different methodologies to obtain the value of the correlation length, however the correlation length varies according to the soil deposit conditions. Therefore, the values for this research were chosen arbitrary to represent a short, medium, and large correlation length according to the dimensions of the soil deposit under study. For each case

of study, 35 simulations were performed, for a total of 210 simulations. Figure 24 and Figure 25 shows examples of the deviation ($\mu \pm x_i$) of different realizations of the random fields generated for the first and second scenario, respectively, representing the number of spaces between each variable for every correlation length.

6.2.3. Random Field property assignment to the Finite Element Mesh

After generating the random fields for the relative density, the values were mapped out into the finite element mesh. To achieve this goal, a coordinate system was assigned to the Random Field. Afterwards, using the MATLAB function named as "griddata" the surface with the coordinate system of the Random Field was interpolated into the coordinate system of the Finite Element Mesh by making a triangulation-based nearest neighbor interpolation. The results from this step were visually evaluated and it was found that the results were consistent with the original random fields as it is shown in Figure 26 and Figure 27, where the deviation ($\mu \pm x_i$) of different examples of the interpolated random fields are presented using the coordinate system of the Finite Elements Mesh.

6.2.4. Parameter interpolation

The constitutive model "PDMY02" does not account implicitly for changes associated to the variation in relative density. This variation must be addressed by calibrating the parameters to their specified relative density. Since the relative density was treated as a random field, it was necessary to find the values of the constitutive model parameters for each value of relative density in the random field. These values were calculated using an interpolation function in MATLAB [116] named as "spline", which makes a cubic data interpolation based on the parameters that were calibrated for the deterministic simulations ($D_R = 55\%, D_R = 65\%\ and\ D_R = 75\%$). Figure 28-33 shows the results for the interpolations conducted to obtain the constitutive model parameters. The parameters that were held constant (c_2, c_3, d_2 and d_3) are omitted. It can be noted that the spline function accurately interpolates the parameters value according to the calibrated parameters of the model. Additionally, the permeability for each element was calculated according to Equation 14 proposed by ElGhoraiby et al [128] .Afterwards, each element of the Finite Random Model was assigned

with their corresponding set of parameters based on the relative density obtained from its coordinate position at the Random Field.

$$k(cm/s) = 0.0207\, e_o - 0.0009$$ Equation 14

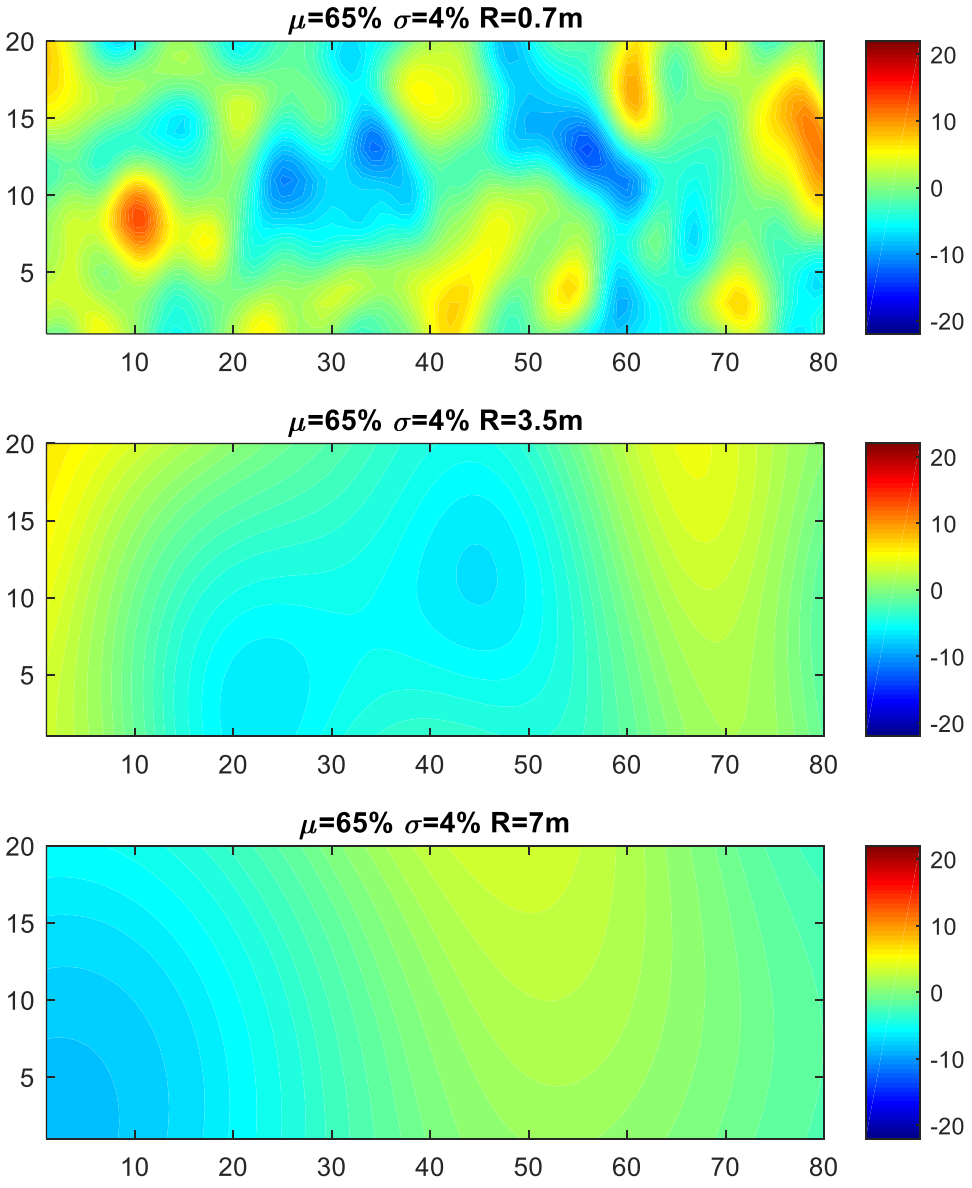

Figure 24. Examples of the deviation in relative density for Random Fields for $\mu_{D_R} = 65\%$, σ_{D_R}=4% (CV=6%).

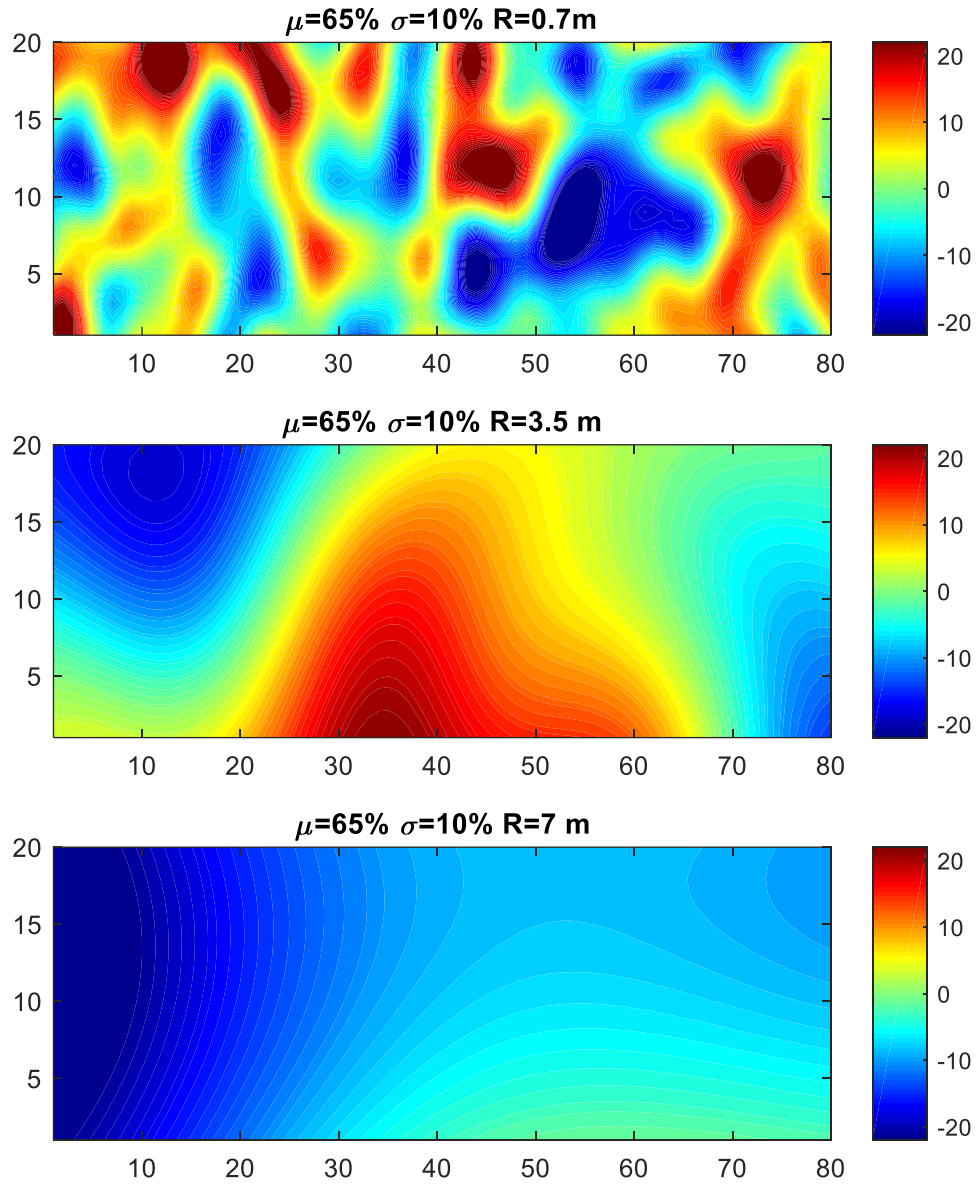

Figure 25. Examples of the deviation in relative density for different Random Fields for μ_{D_R} = 65%, σ_{D_R}=10% (CV=15%).

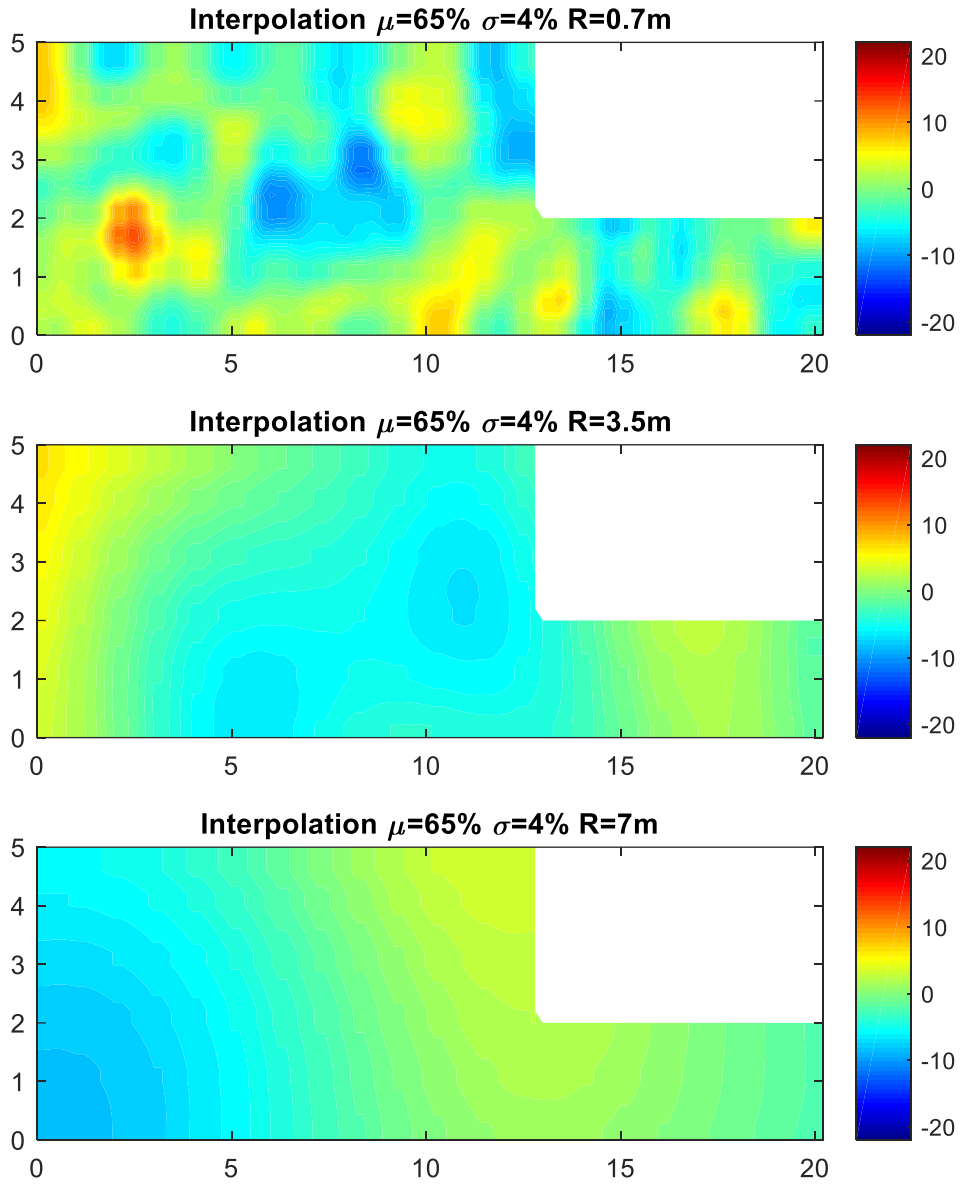

Figure 26. Examples of the deviation in relative density for interpolated Random Fields for μ_{D_R} = 65%, σ_{D_R}=4% (CV=6%).

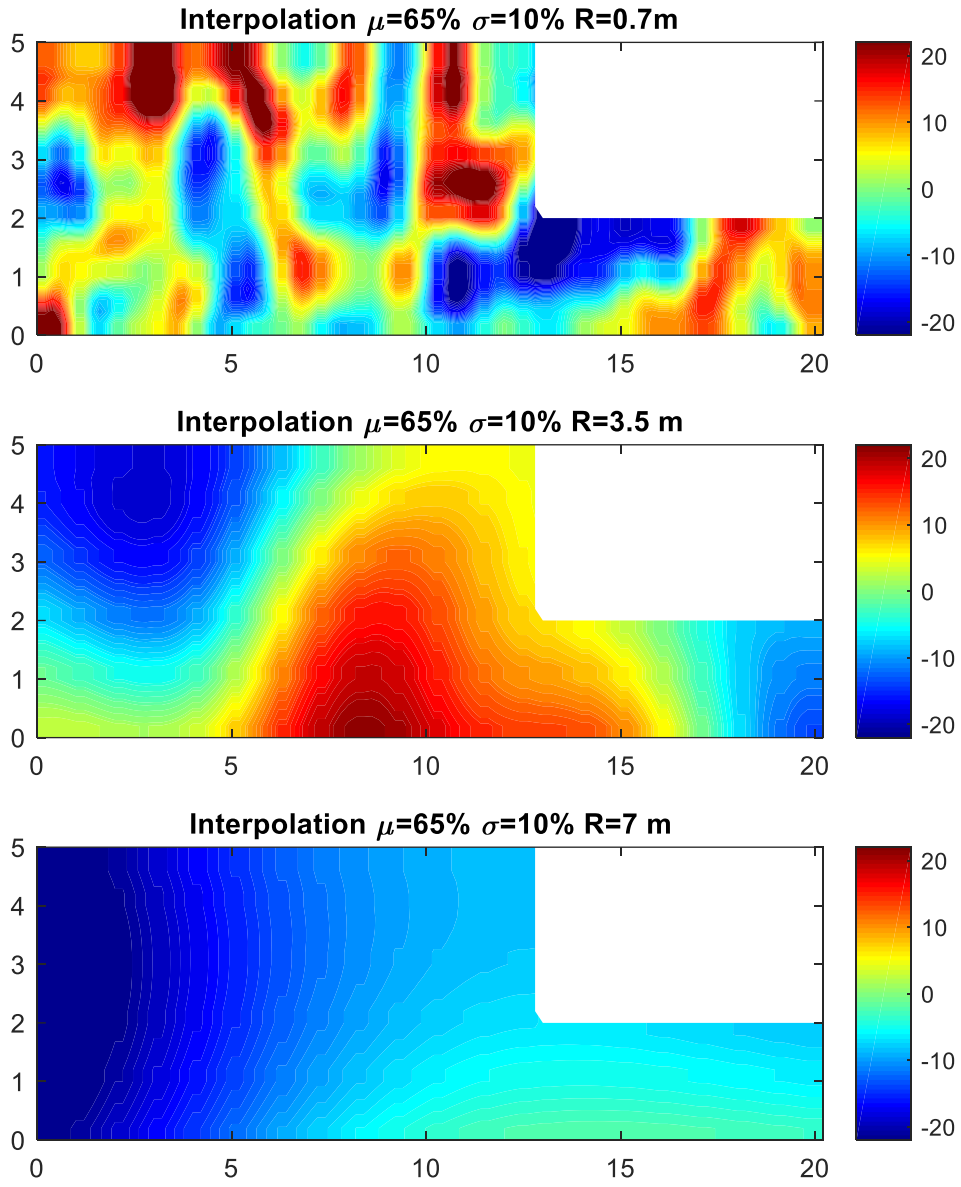

Figure 27. Examples of the deviation in relative density for interpolated Random Fields for μ_{D_R} = 65%, σ_{D_R}=10% (CV=15%).

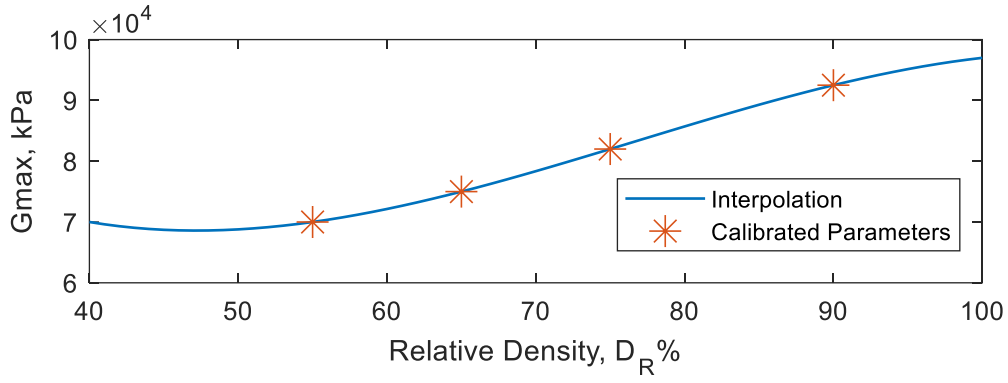

Figure 28. Interpolation results. Shear Modulus (Gmax) vs. Relative density (D_R)

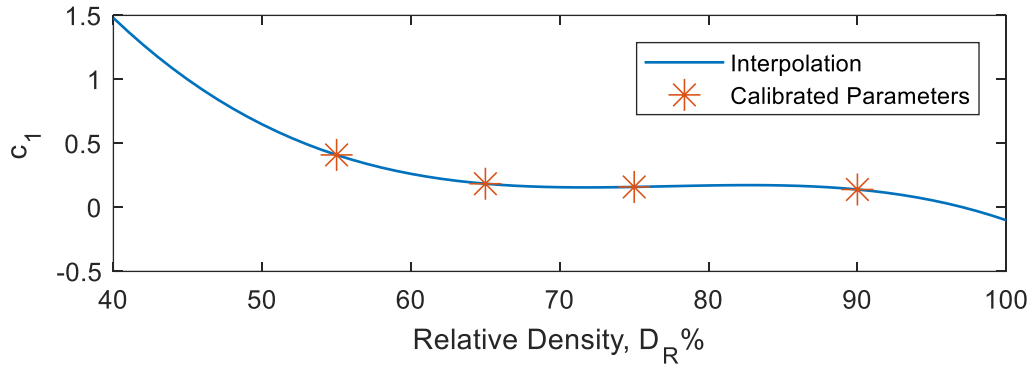

Figure 29. Interpolation results for the parameter c1 vs. Relative density (D_R)

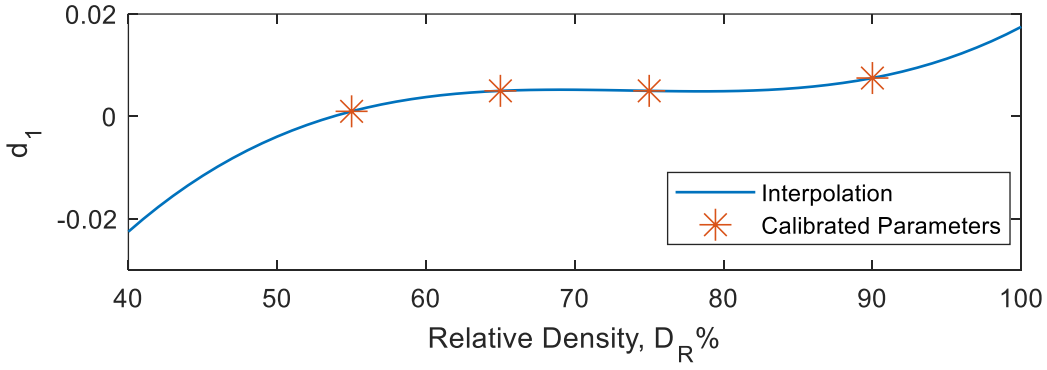

Figure 30. Interpolation results for the parameter d1 vs. Relative density (D_R)

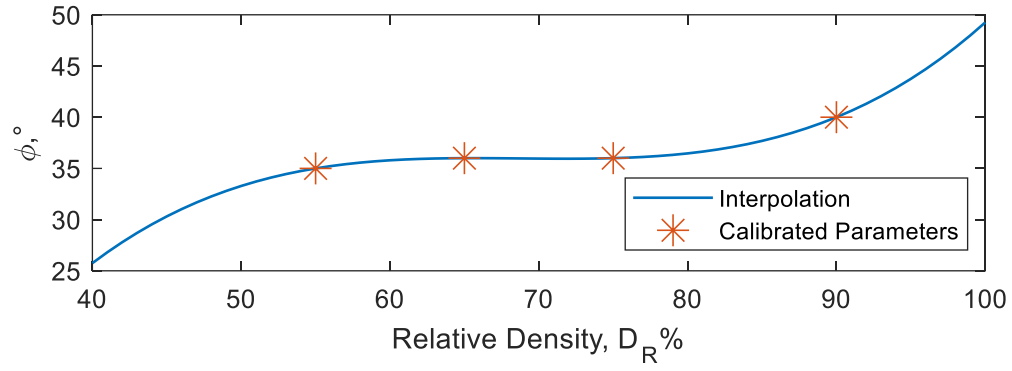

Figure 31. Interpolation results for the friction angle ϕ vs. Relative density (D_R)

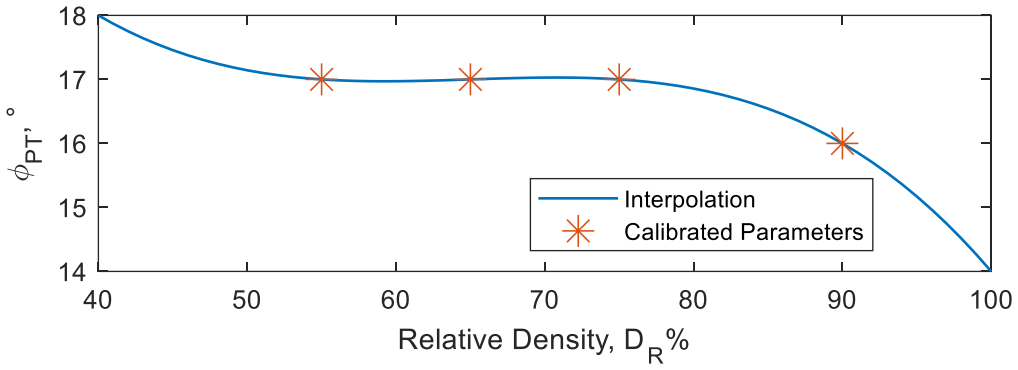

Figure 32. Interpolation results for the phase transformation phase angle ϕ_{P_T} vs. Relative density (D_R)

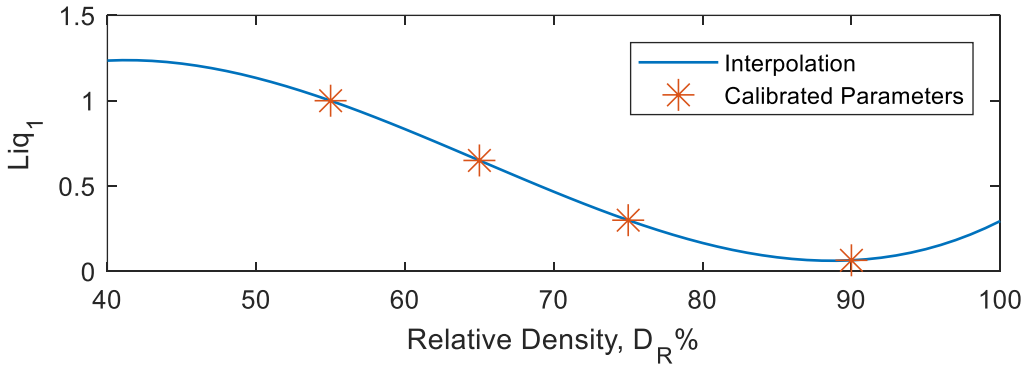

Figure 33. Interpolation results for the parameter Liq1 vs. Relative density (D_R)

6.3. Deterministic vs. stochastic analysis results and interpretation

This section presents a comparison between the results from the deterministic simulations, experimental tests, and probabilistic analyses performed. The results are arranged in figures that have the configuration of a matrix of 4 rows and two columns. The first row presents in the first column the results of the centrifuge tests and the second column shows the deterministic results for the three different relative densities ($D_R = 55\%, D_R = 65\%$ and $D_R = 75\%$). Consecutively, the following three rows shows the results corresponding to the stochastic analyses for the three different correlation lengths under study (R=0.7m, R=3.5m and R=7m). The first column exhibits the results for the first scenario, which corresponds to the random fields of the relative density generated with a standard deviation of 4% (CV=6%), and the second column exposes the results for the second scenario; random fields for the relative density generated with a standard deviation of 10% (CV=15%).

The probabilistic results are presented in figures that shows the 99.7% confidence interval in color gray, which corresponds to $\mu \pm 3\sigma$. The mean value of the probabilistic simulations is presented with a black line and in dashed lines the value of the boundary $\mu \pm \sigma$ can be found. Each figure presents a different sensor located at the top layer of the model. The locations of each sensor are illustrated in Figure 1.

The acceleration response is presented in Figure 34-36 for the furthest to the nearest top array of accelerometers, respectively. Figure 37-39 show the spectral acceleration response calculated using the accelerometers measurements. Additionally, the excess pore-water pressure response is displayed in Figure 46-48 for the furthest to the nearest top array of pore-water pressure transducers. To measure the vertical settlements, two sensors were used, sensor WY, which was located approximately 1 meter behind the sheet-pile and sensor B, located approximately 10 meters behind the sheet-pile. For the sake of brevity, only the results for sensor WY are presented at the surface level in Figure 58. The results for the lateral displacement of the wall at the surface level (Z=5m) can be found in Figure 57Figure 48.

In terms of the acceleration response, it can be noted that there is a good match between the accelerometer's measurements and the deterministic predictions of the acceleration

response as shown in Figure 34-36. However, after the liquefaction stared, the match decays and in some of the sensor location, the acceleration response goes to zero at the top of the array. The probabilistic simulations show similar trends for all the sensors (AHB3 (Figure 34), AHM3 (Figure 35), AHW3 (Figure 36)) for this variable. The simulations corresponding to the first scenario (Random field with standard deviation of 4%, CV=6%) and the second scenario (Random field with standard deviation of 10%, CV=15%) show that the range of variation becomes wider as the correlation length increases.

Figure 40-45 show the mean acceleration response and the standard deviation presented in the time history for the three sensors (AHB3, AHM3 and AHW3) and the two scenarios under study. In terms of the mean value, all the scenarios showed similar responses for every correlation length. The standard deviation of the probabilistic simulations for the sensor AHB3 (Figure 40, Figure 41) presented a value up to 0.1 g-0.12 g approximately for both scenarios, this sensor had the smallest range of variation. The probabilistic simulation results for the sensor AHM3 (Figure 42, Figure 43) had a value of standard deviation up to 0.16 g for the first scenario and 0.18 g for the second scenario. The probabilistic simulations for the sensor AHW3 (Figure 44, Figure 45) showed a value up to 0.18 g for both scenarios of standard deviation. It is important to mention that all the scenarios showed that the standard deviation increases with the correlation length.

Additionally, the deterministic simulations were not able to capture accurately the amplitude of "dilation" spikes in the acceleration response, probably because they occur at small time steps and there is not enough resolution in the computer to obtain this level of detail. However, the probabilistic simulations were able to capture the dilation spikes for the sensors AHM3 and AHW3. The effects of the dilation spikes were more visible with the increment in the correlation length.

The spectral acceleration response was calculated based on the acceleration time history results. The deterministic simulations reasonably capture the behavior of the spectral response of the centrifuge tests as it is shown in Figure 37-39. The period of the maximum spectral acceleration was predicted in most of the cases. However, as it was mentioned before, the numerical model was not able to simulate the amplitude of dilation spikes, which leads to

discrepancies at the beginning of the spectrums between the experimental and deterministic results.

The probabilistic simulations for the spectral acceleration response show similar behavior for all the sensors (Figure 37-39). The confidence interval for the 99.7% of data for the shortest correlation length (R=0.7 m) was small, similarly to the results of the acceleration time history. The range of variation increases with the standard deviation and the value of the correlation length. The probabilistic simulations of spectral response were not able to capture the behavior of the centrifuge test for the initial periods either. Figure 59 shows the values for the maximum mean and the maximum coefficient of variation for the spectral acceleration response for all sensors and scenarios evaluated.

In terms of the maximum mean value of the spectral acceleration response, it is noted that the maximum mean values and their trends, for all sensors, are very similar and they do not present much variation between the first and the second scenario. Meanwhile, the maximum coefficient of variation has a wide range of uncertainty, because it ranges from 10% to almost 40%. Additionally, when analyzing the behavior for different correlation lengths, it can be observed that the maximum coefficient of variation increases with a very steep slope between the correlation length of 0.7 m and 3.5m. After that, between 3.5 m and 7.0 m the slope becomes almost constant.

The results for the excess pore-water pressure are presented in Figure 46-48. The deterministic simulations were able to reasonable predict the excess pore-water pressure trend showed by the experimental tests. However, the centrifuge experiments did not show negative excess pore-water pressure for the pore pressure transducers located nearest to the wall (SENSOR PW3 in Figure 48). This could have been caused by restrictions in the sheet pile movement response, such as friction.

In terms of stochastic analyses, for the furthest sensor (Sensor PB3 (Figure 46)) the simulations presented a smaller variation for the first scenario of analysis (σ_{DR}=4%, CV=6%) than for the second scenario (σ_{DR}=10%, CV=15%). The trend for the pore-water pressure build up is similar for all cases. For both scenarios, the correlation length of 3.5 m shows a wider confidence interval than the correlation length of 0.7 m and 7.0 m.

Figure 49 and Figure 50 shows that the mean of the excess pore-water of the Sensor PB3 is similar for all the correlation lengths and both scenarios. In terms of the standard deviation, the first scenario ($\sigma_{DR} = 4\%$) shows similar standard deviations for all the correlation lengths, meanwhile, the second scenario, ($\sigma_{DR} = 10\%$), presents the biggest standard deviation for the correlation length of 3.5 m.

The sensor at the middle of the model PM3 (Figure 47) shows similar results to the furthest sensor, as presented in Figure 51 and Figure 52. In the pore-water pressure build up the range of variation is wider, meanwhile, in the dissipation phase, the range of variation decreases. The first scenario ($\sigma_{DR} = 4\%$) showed similar ranges of variation for all the correlation lengths under study. Unlike the second scenario ($\sigma_{DR} = 10\%$), which presented the widest range of variation for the correlation length of 3.5 m. Figure 51 and Figure 52 shows that the correlation length does influence the mean excess pore-water pressure, unlike the standard deviation that is directly affected by the values of the correlation length.

The sensor located nearest to the wall PW3 (Figure 48) showed the widest range of variation of all sensors. For the first scenario, in the buildup phase, the range is small, and it started to become wider as the time increases, achieving its widest range in the dissipation phase. In this scenario, all the correlation lengths showed similar ranges of variation. The second scenario showed wider ranges for the pore-water pressure build up and for the dissipation phase than the first scenario. Also, the correlation length of 3.5 m showed the biggest range of variation. This phenomenon can be easily appreciated in Figure 53 and Figure 54 that shows the mean value and the standard deviation of the excess pore-water pressure for all the time history por Sensor PW3. Figure 60 presents the maximum mean and standard deviation observed for every sensor.

In terms of horizontal displacement, the deterministic simulations were able to predict the trends presented and its maximum value. It can be noted that there is a mechanism that cannot be captured by the deterministic model when the shaking is happening, this could have been caused by the amplification of vertical and compressive waves due to the water. The effect of the water changes over time, but this is not considered in the numerical model.

Likewise, the probabilistic simulations were able to estimate a confidence interval that can predict the experimental results of the horizontal displacement for the three values of relative density evaluated in the centrifuge tests as can be seen in Figure 57. Table 2 and Table 3

presents the statistics for the final horizontal displacement for the first and second scenario, respectively. The mean value of the final horizontal displacements for the first scenario is similar for all correlation lengths, ranging from 46.07 cm to 48.89 cm. However, the mean value of the final horizontal displacements for the second scenario is directly affected by the correlation length, because the results range from 53.09 cm to 73.17 cm. In terms of the horizontal displacement, the coefficient of variation ranges from 16%-48% for the first scenario and from 30%-71% for the second scenario, indicating the level of dispersion that the soil response can present in relation to the mean values. Figure 55 shows the mean and coefficient of variation of the final horizontal displacement.

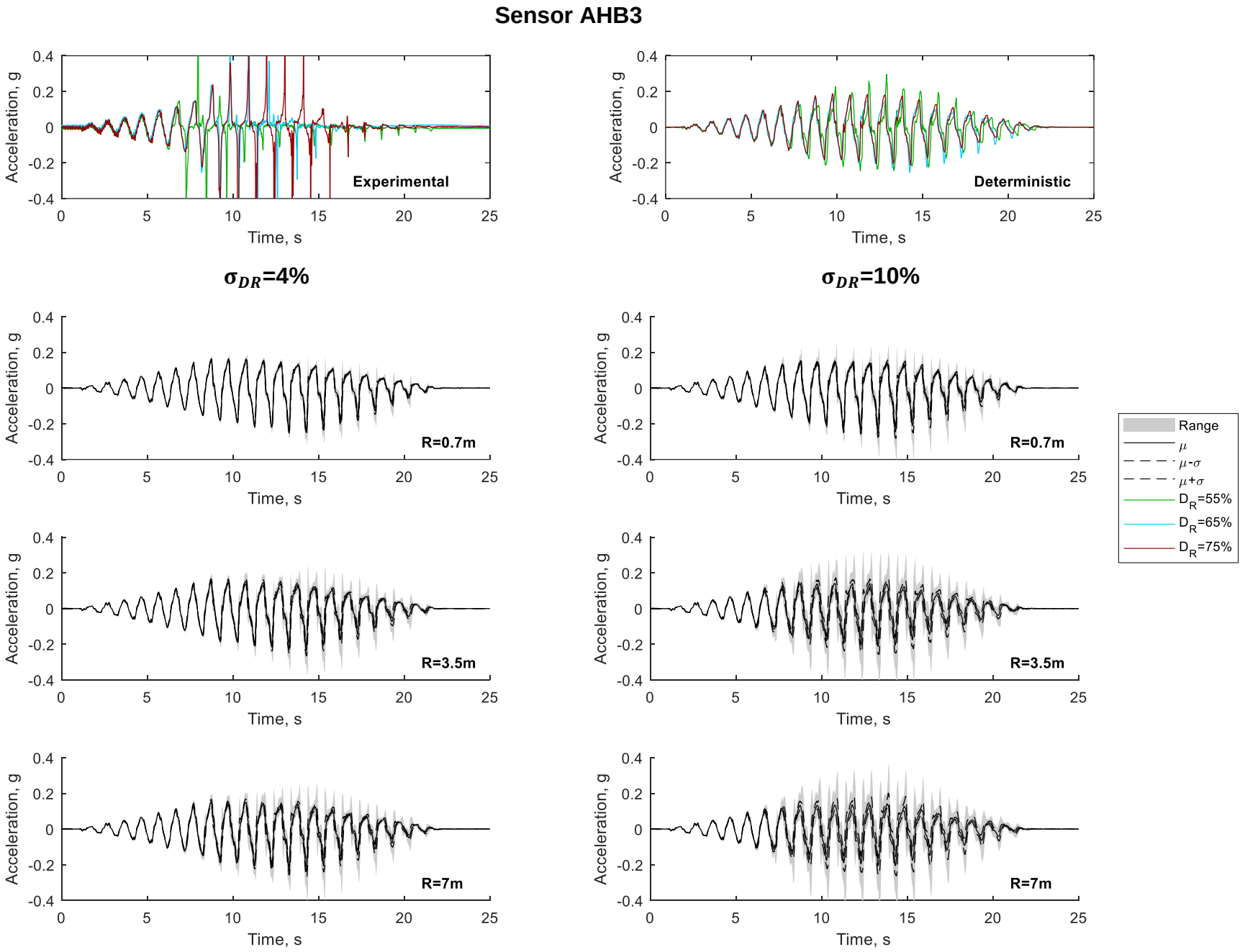

Figure 34. Experimental, deterministic, and stochastic acceleration response corresponding to the furthest sensor (AHB3) of the top array of accelerometers.

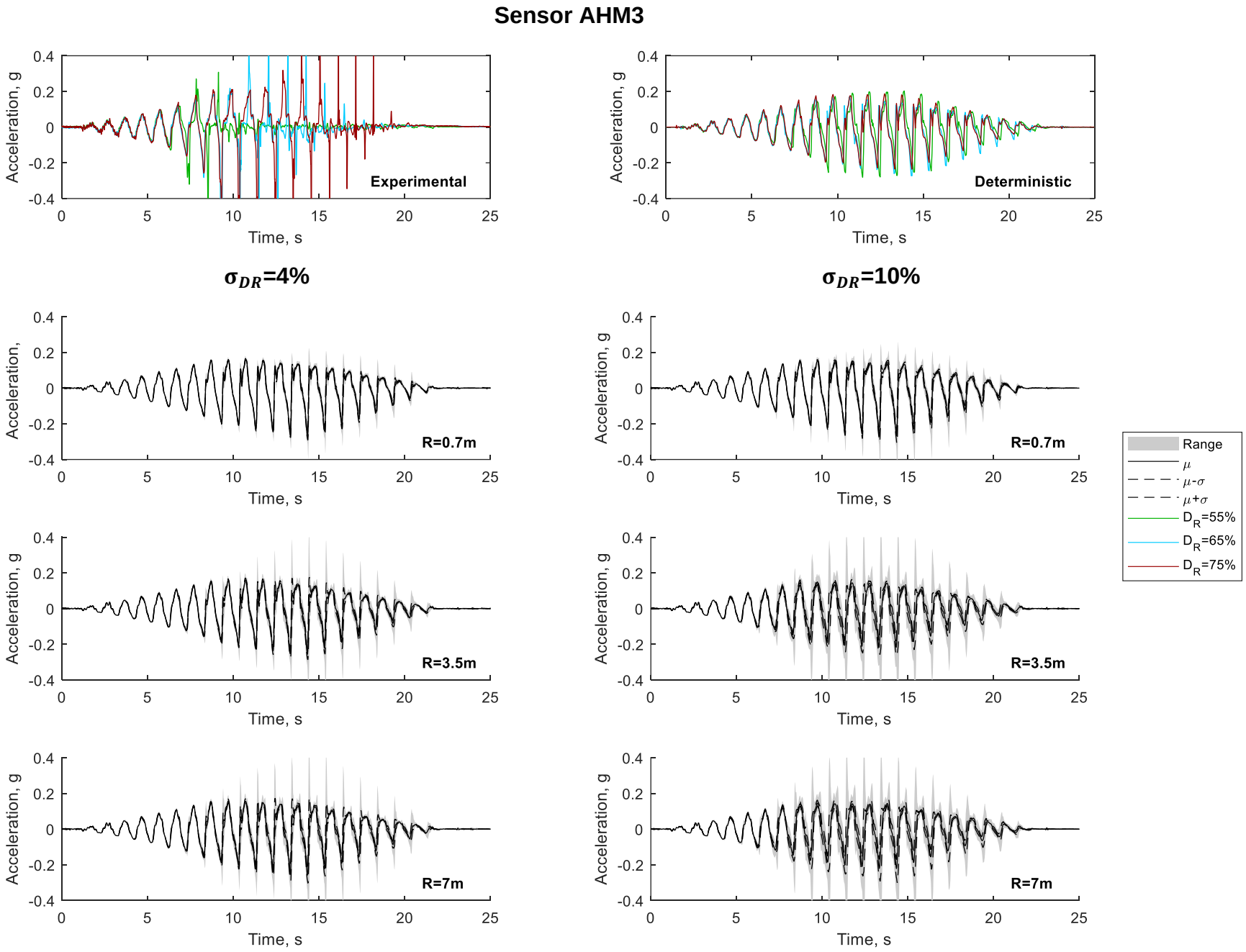

Figure 35. Experimental, deterministic, and stochastic acceleration response corresponding the middle sensor of the top array (AHM3) of accelerometers

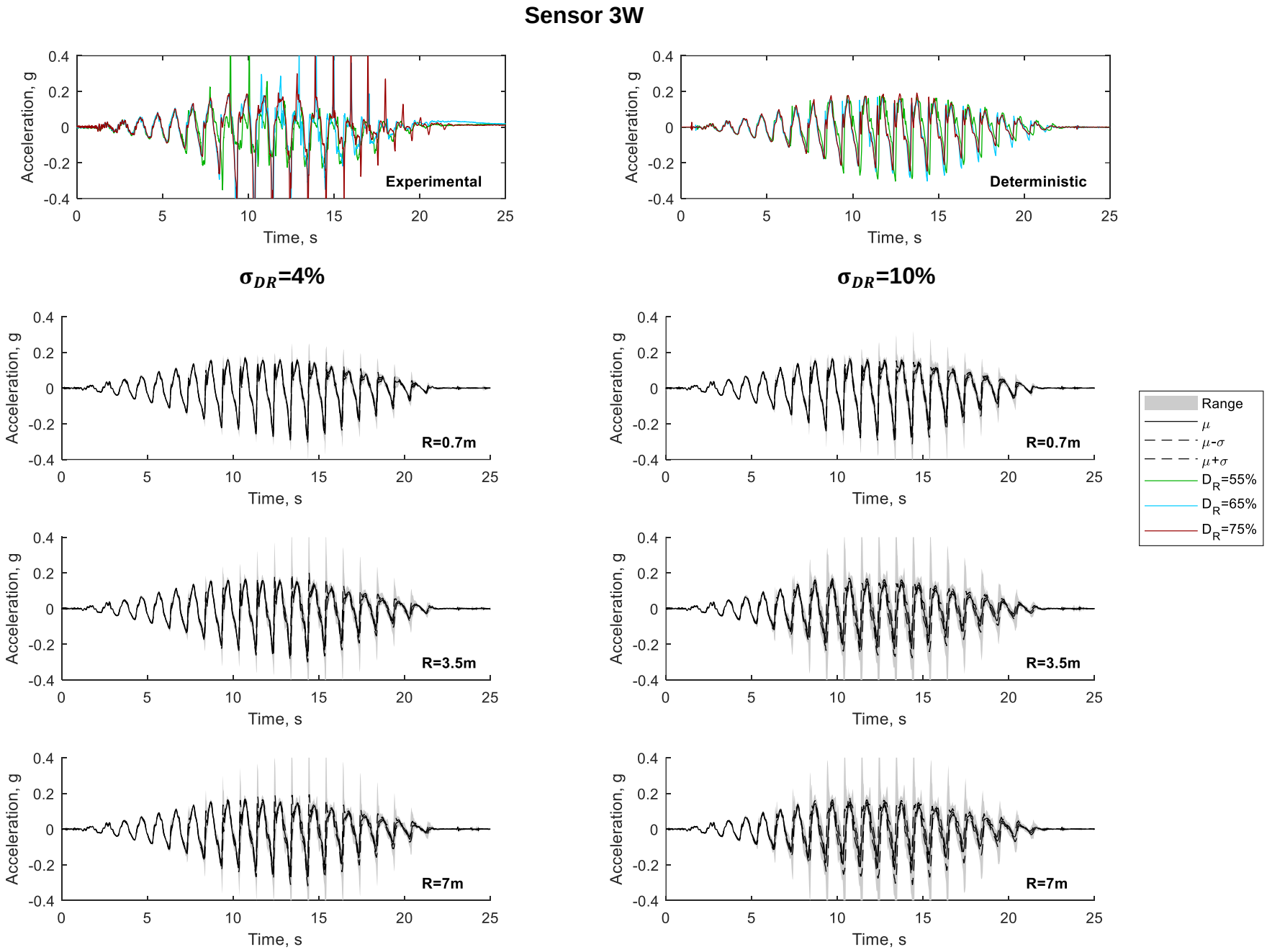

Figure 36. Experimental, deterministic, and stochastic acceleration response corresponding the nearest sensor (AHW3) of the top array of accelerometers.

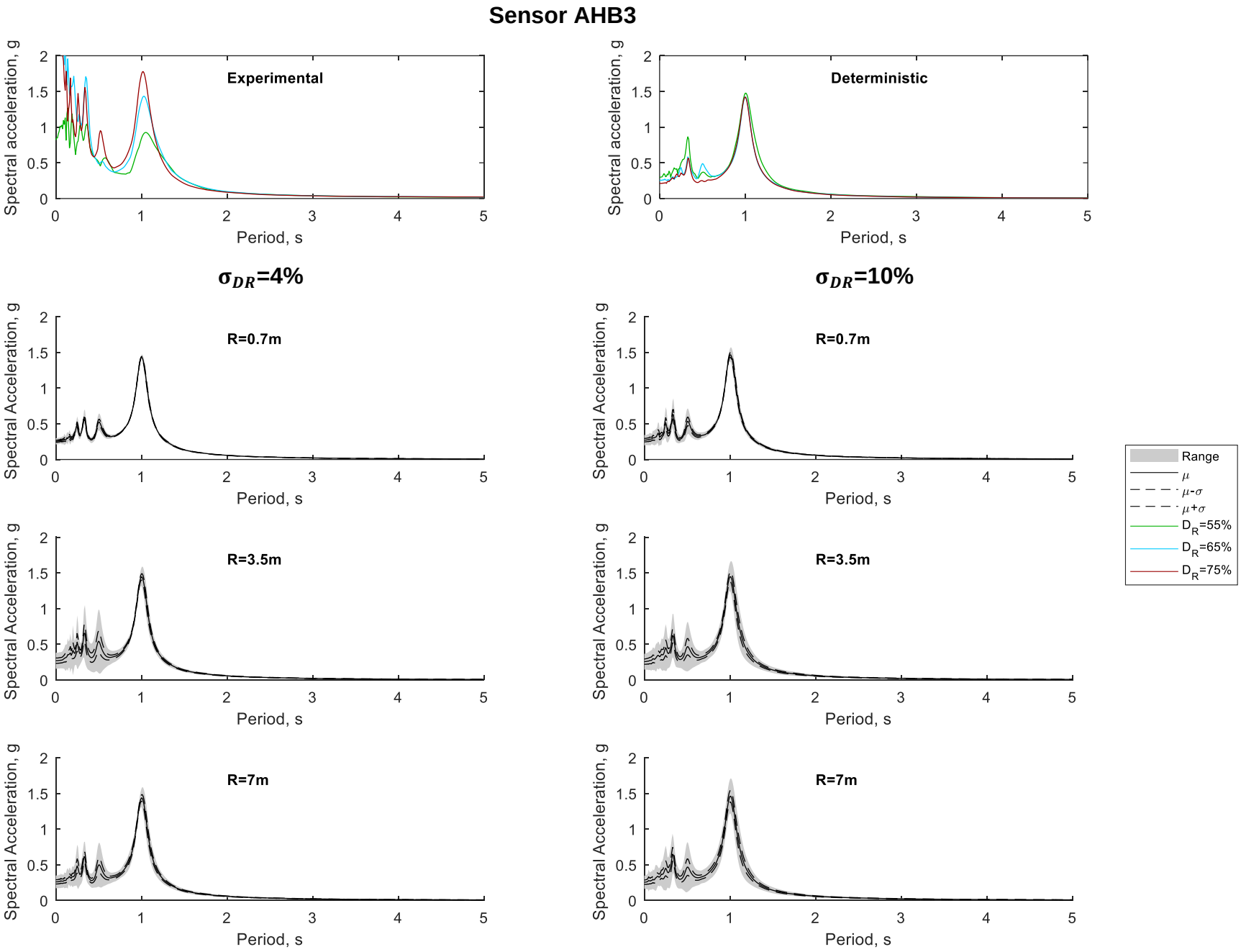

Figure 37. Experimental, deterministic, and stochastic spectral acceleration response corresponding to the furthest sensor (AHB3) of the top array of accelerometers.

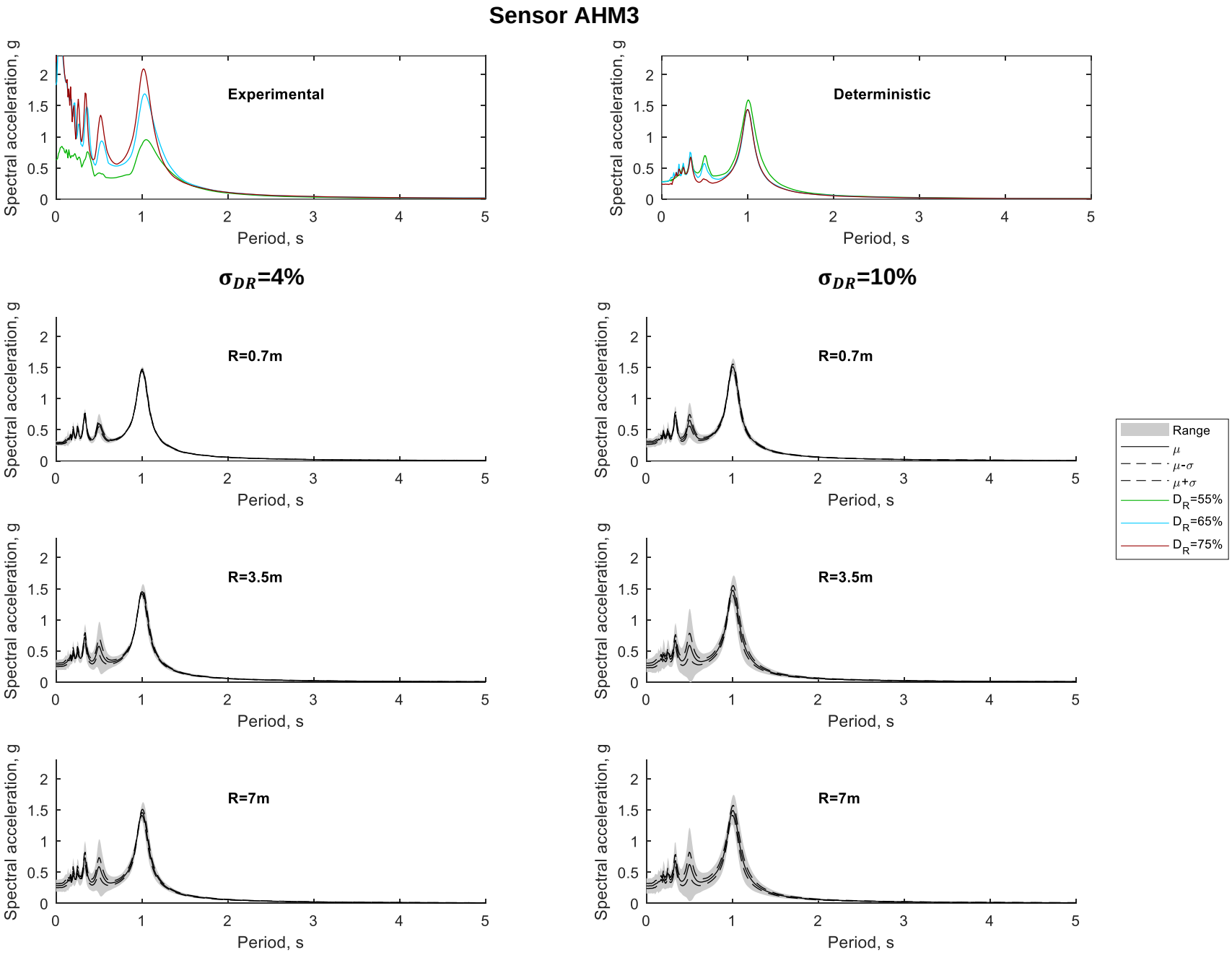

Figure 38.Experimental, deterministic, and stochastic spectral acceleration response corresponding to the middle sensor (AHM3) of the top array of accelerometers.

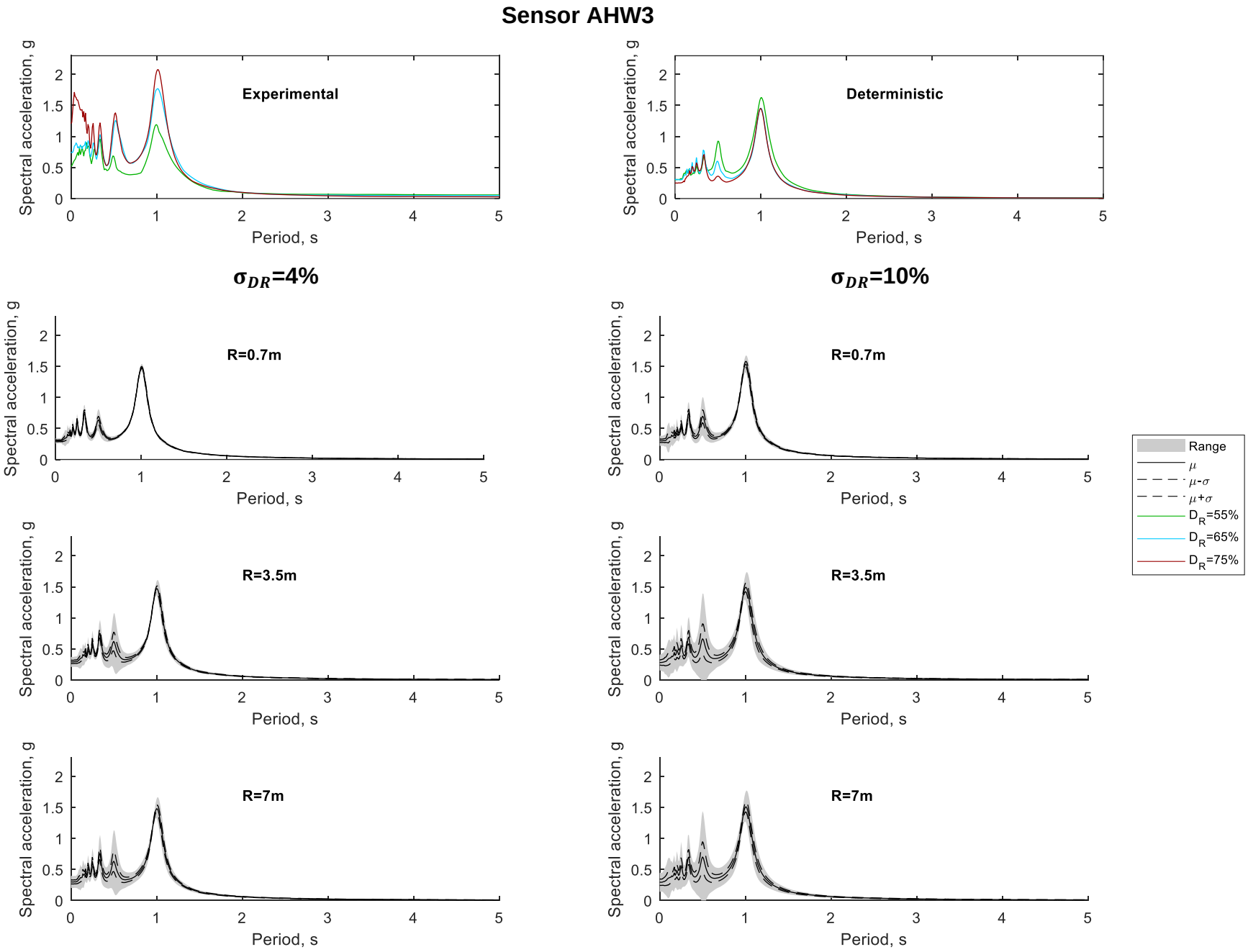

Figure 39. Experimental, deterministic, and stochastic spectral acceleration response corresponding to the nearest sensor (AHW3) of the top array of accelerometers.

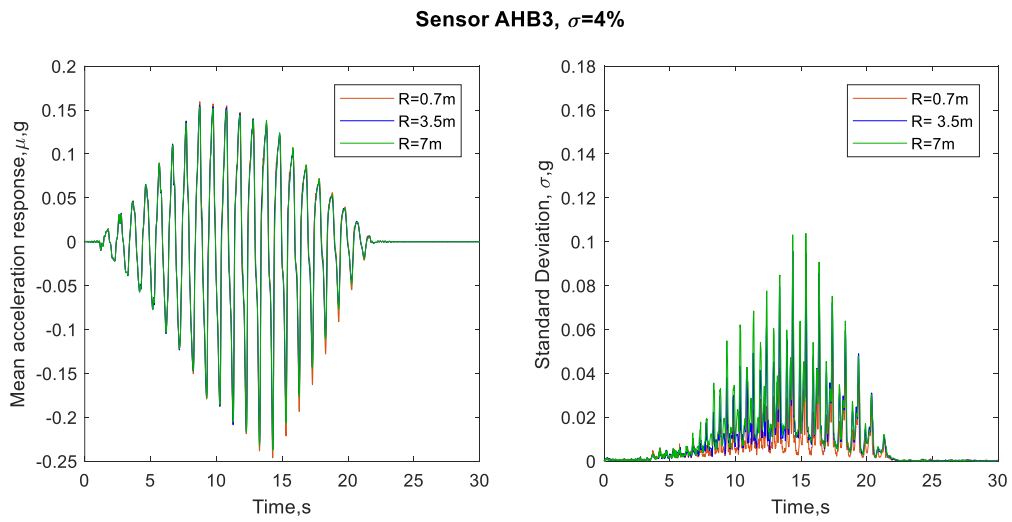

Figure 40. Mean and standard deviation for the acceleration response time history for σ_{DR}=4% (C.V.=6%) Sensor AHB3

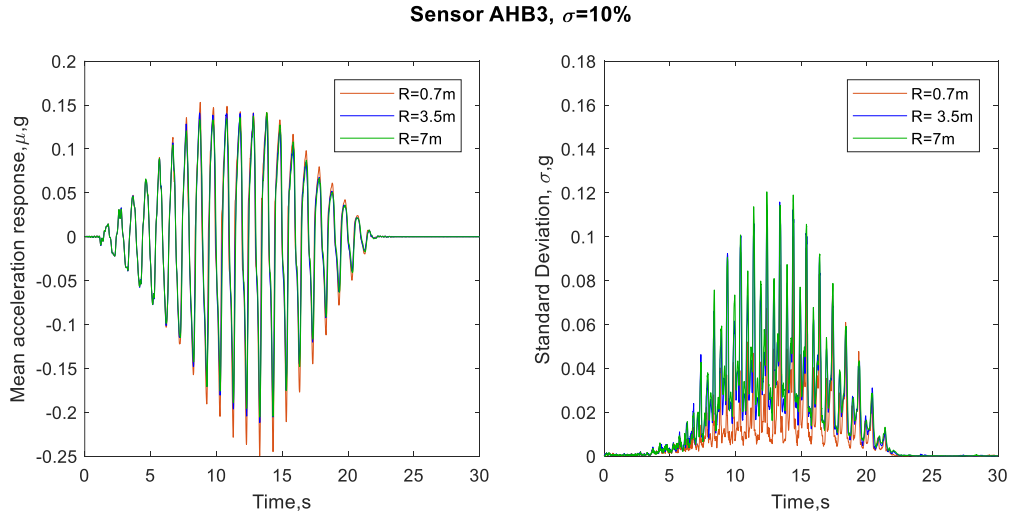

Figure 41. Mean and standard deviation for the acceleration response time history for σ_{DR}=10% (C.V.=15 %) Sensor AHB3

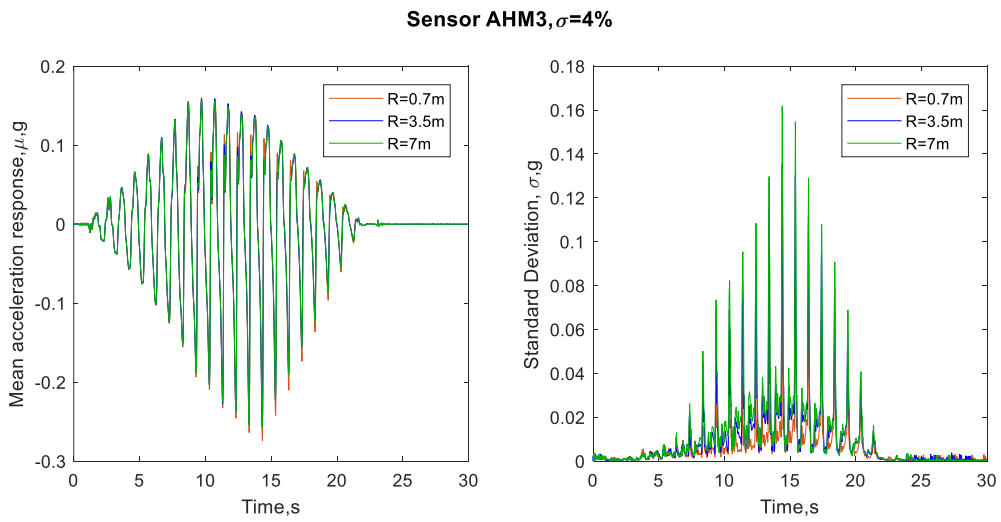

Figure 42. Mean and standard deviation for the acceleration response time history for σ_{DR}=10% (C.V.=6 %) Sensor AHM3

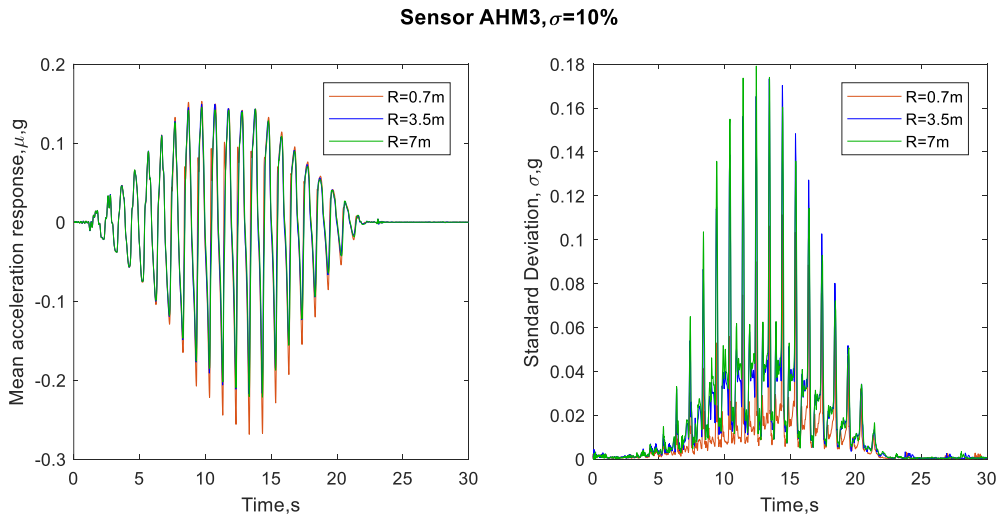

Figure 43. Mean and standard deviation for the acceleration response time history for σ_{DR}=10% (C.V.=15%) Sensor AHM3

Equally important, the deterministic results show a consistent prediction with the centrifuge experiments for the maximum vertical settlement. Similarly, the probabilistic simulations were able to predict the vertical settlements for all the three values of relative density tested on the centrifuge experiments. Figure 58 presents the results of the vertical settlements for the probabilistic simulations. The range of variation of the vertical settlement increases with the increment in the correlation length. Figure 56 , Table 4 and Table 5 presents the statistics for

the final settlement for all scenarios. The first scenario presents similar results for the mean of the final vertical settlement and the second scenario shows that with the increment in the correlation length, the mean of the final vertical settlement can vary from -10 cm to -15cm. It is also important to mention that the coefficient of variation ranges 25% to 55% in the first scenario and from 32% to 85% in the second scenario, indicating the variation expected in terms of the settlements of this problem.

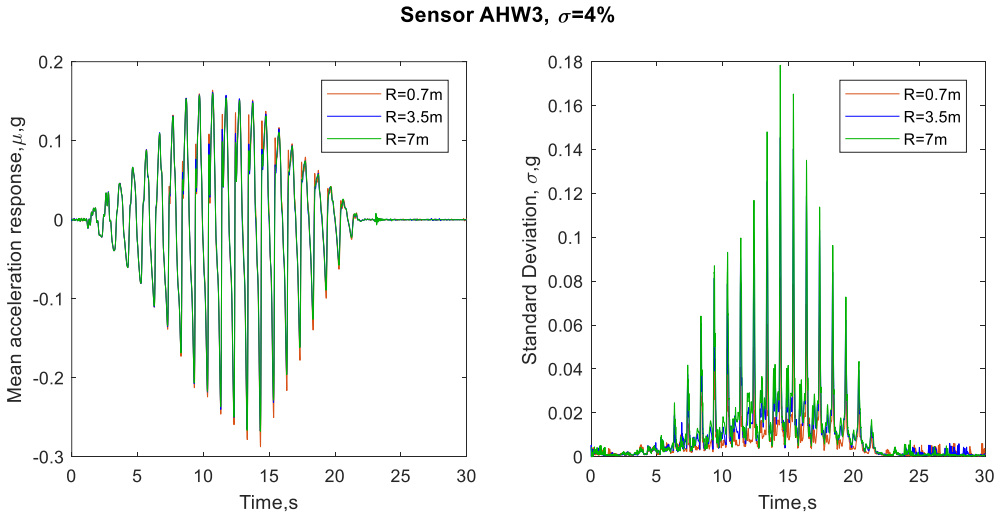

Figure 44. Mean and standard deviation for the acceleration response time history for σ_{DR}=4% (C.V.=6 %) Sensor AHW3

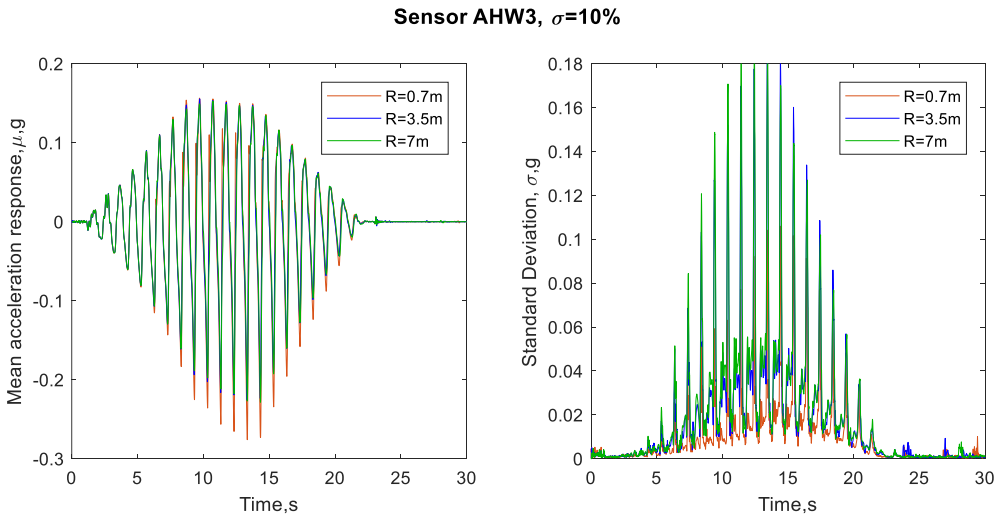

Figure 45. Mean and standard deviation for the acceleration response time history for σ_{DR}=10% (C.V.=15 %) Sensor AHW3

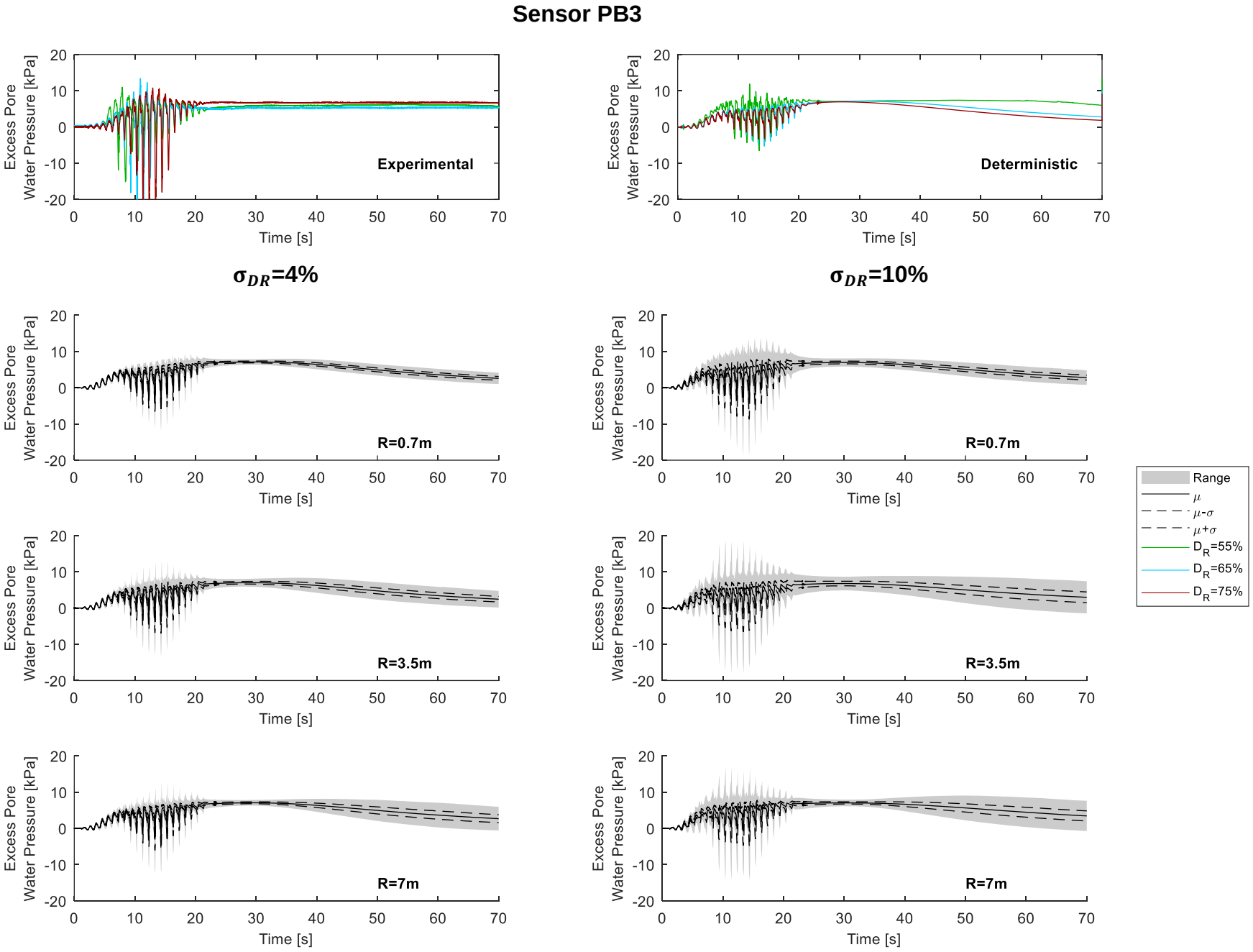

Figure 46. Experimental, deterministic, and stochastic results of the excess pore-water pressure response corresponding to the furthest sensor (PB3) at the top horizontal array of pore pressure transducers.

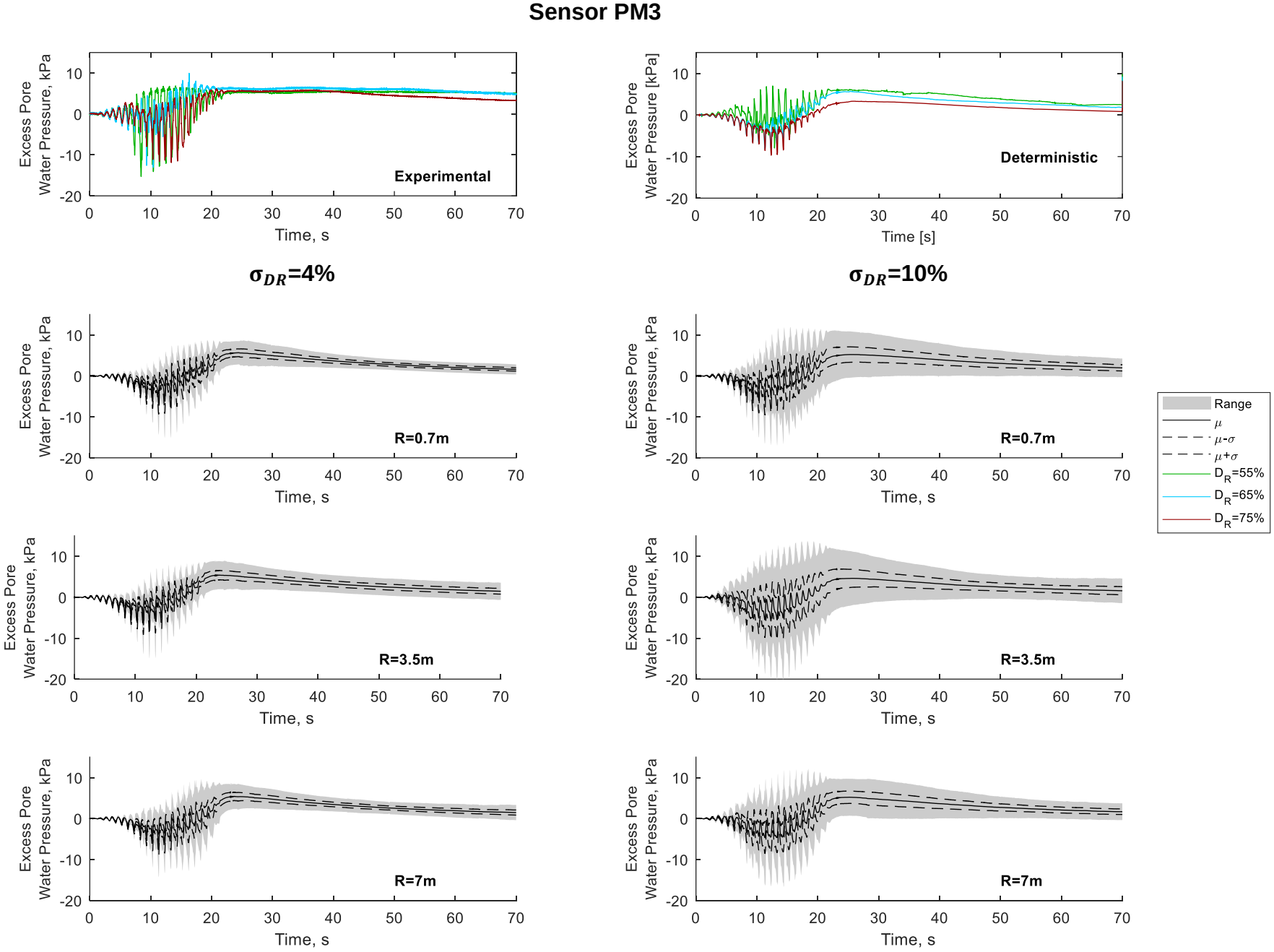

Figure 47. Experimental, deterministic, and stochastic results of the excess pore-water pressure response corresponding to the middle sensor (PM3) at the top horizontal array of pore pressure transducers.

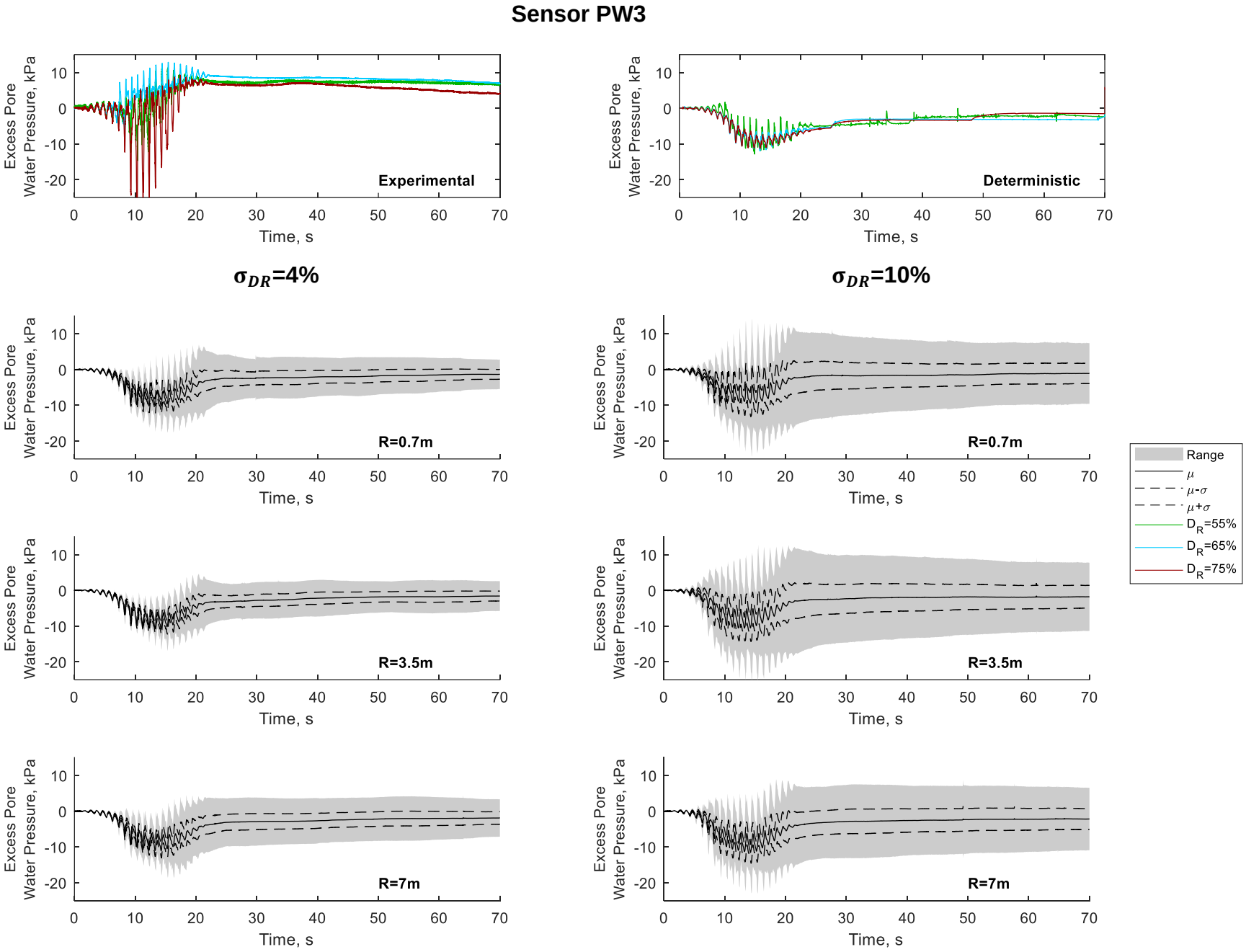

Figure 48. Experimental, deterministic, and stochastic results of the excess pore-water pressure response corresponding to the nearest sensor (PW3) at the top horizontal array of pore pressure transducers.

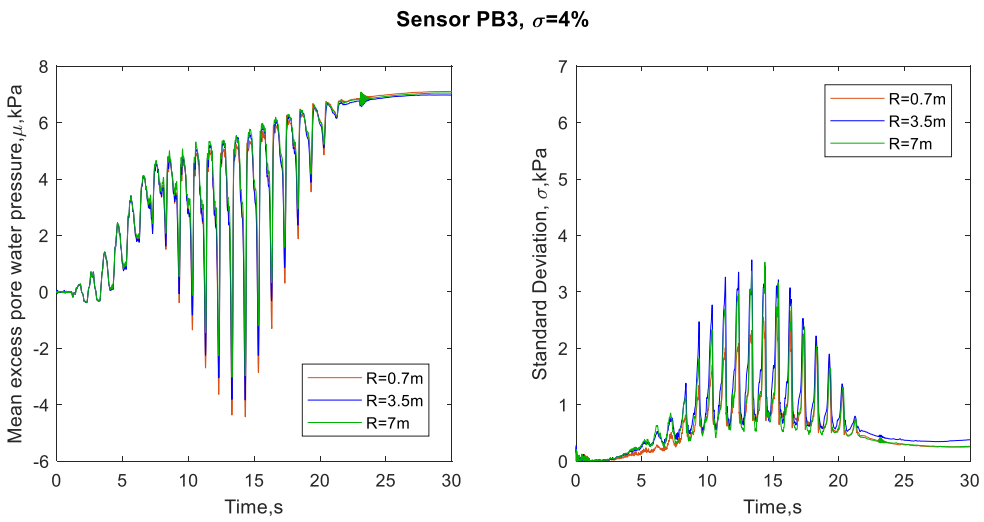

Figure 49. Mean Excess pore-water pressure and standard deviation for the first scenario ($\sigma_{DR} = 4\%, CV = 6\%$) Sensor PB3

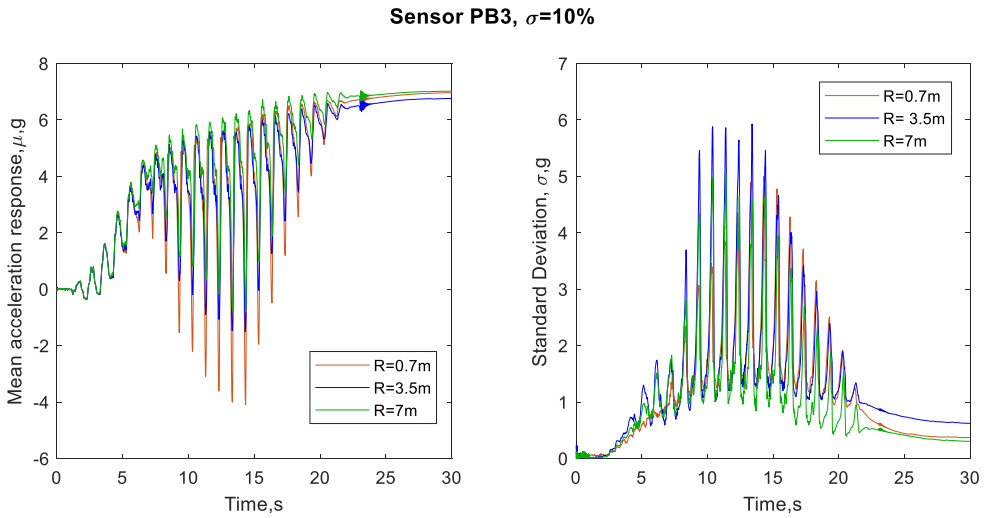

Figure 50. Mean Excess pore-water pressure and standard deviation for the second scenario ($\sigma_{DR} = 10\%, CV = 15\%$) Sensor PB3

Table 2. Statistics for the final horizontal displacement for the first scenario (σ_{DR}=4%)

Correlation length, m	μ, cm	σ, cm	CV, %
R=0.7	46.07	7.25	16
R=3.5	46.41	18.40	40
R=7	48.89	23.43	48

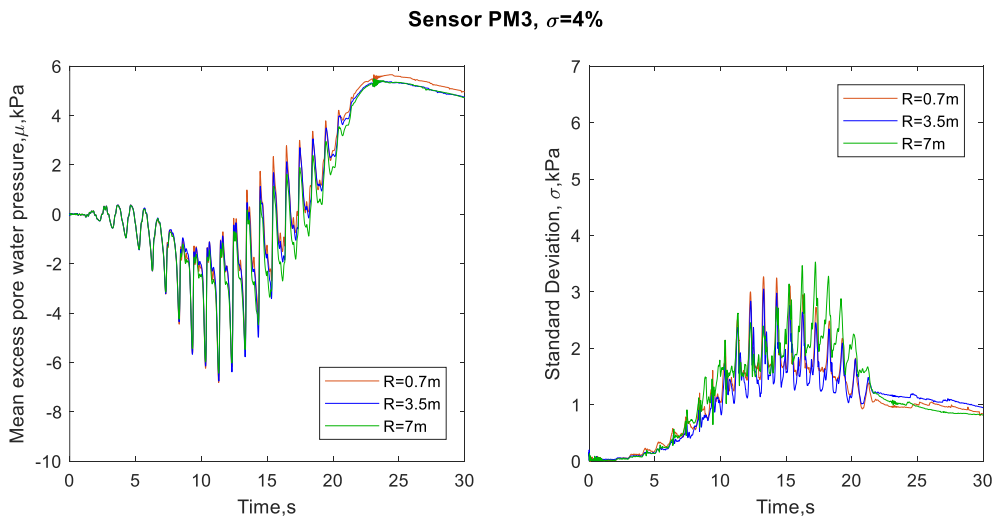

Figure 51. Mean Excess pore-water pressure and standard deviation for the first scenario ($\sigma_{DR} = 4\%, CV = 6\%$) Sensor PM3.

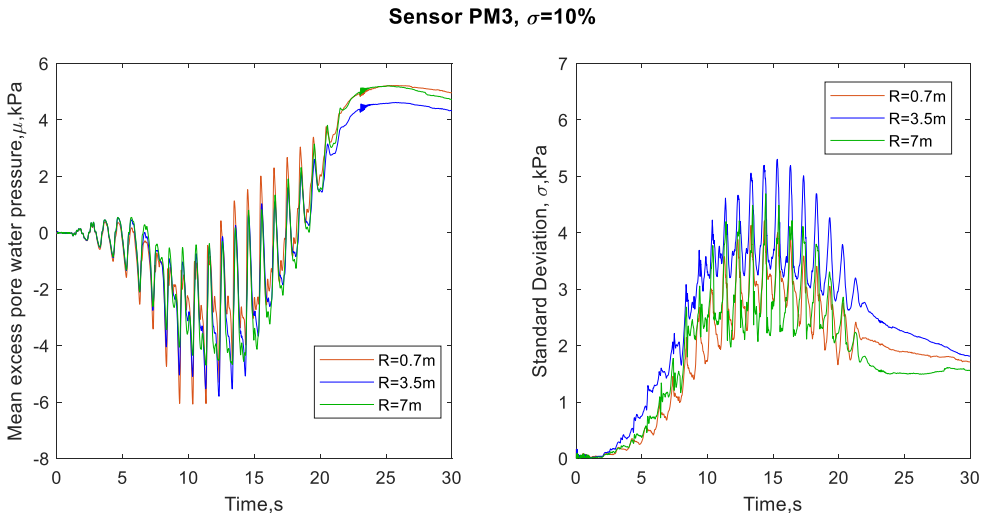

Figure 52. Mean Excess pore-water pressure and standard deviation for the second scenario ($\sigma_{DR} = 10\%, CV = 15\%$) Sensor PM3.

Table 3. Statistics for the final horizontal displacement for the second scenario (σ_{DR}=10%)

Correlation length, m	μ, cm	σ, cm	CV, %
R=0.7	53.09	15.88	30
R=3.5	64.92	47.91	74
R=7	73.17	51.49	71

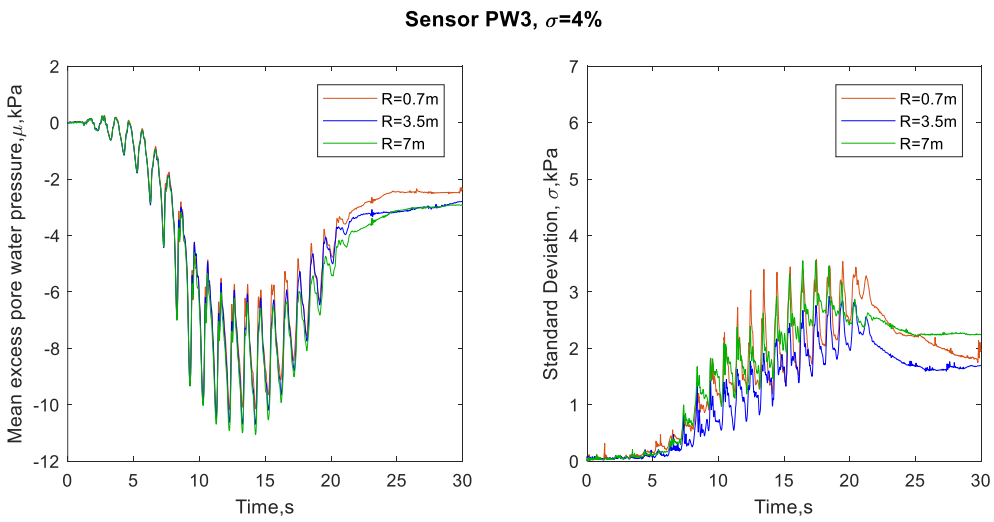

Figure 53. Mean Excess pore-water pressure and standard deviation for the first scenario ($\sigma_{DR} = 4\%, CV = 6\%$) Sensor PM3.

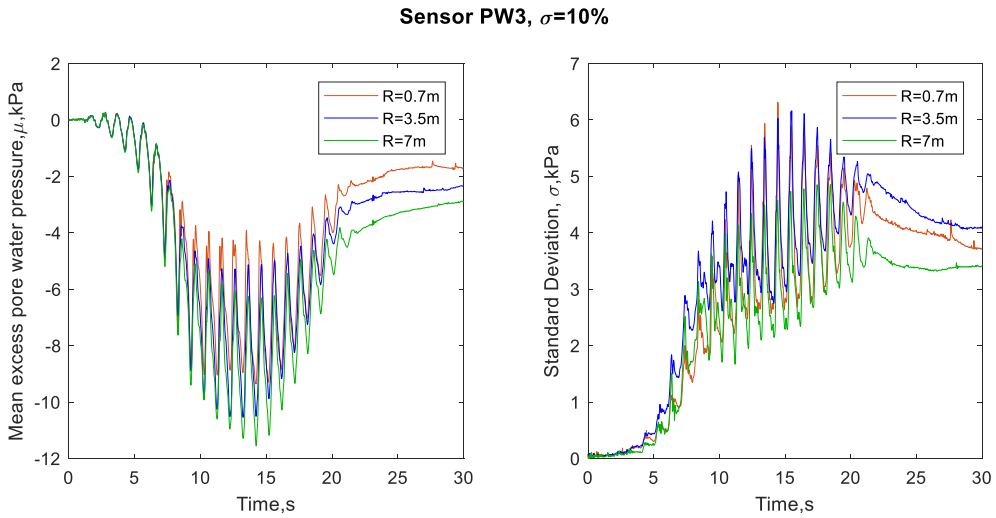

Figure 54. Mean Excess pore-water pressure and standard deviation for the second scenario ($\sigma_{DR} = 10\%, CV = 15\%$) Sensor PM3.

Table 4. Statistics for the final vertical settlements for the first scenario (σ_{DR}=4%)

Correlation length, m	μ, cm	σ, cm	CV, %
R=0.7	-7.79	2.09	27
R=3.5	-8.26	3.50	42
R=7	-8.52	4.76	56

Table 5. Statistics for the final vertical settlements for the second scenario (σ_{DR}=10%)

Correlation length, m	μ, cm	σ, cm	CV, %
R=0.7	-10.12	3.45	34
R=3.5	-12.91	10.70	83
R=7	-14.48	12.30	85

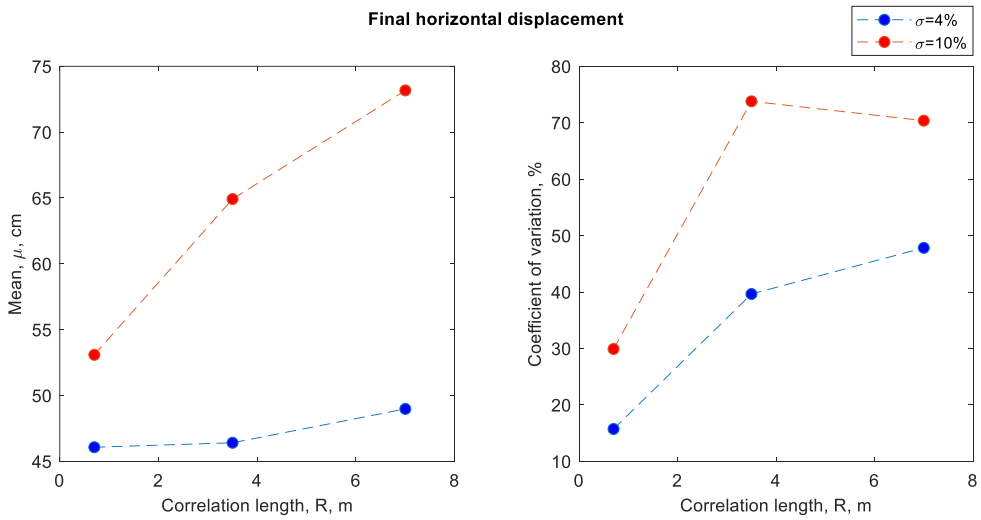

Figure 55. Mean and coefficient of variation for the final horizontal displacement vs. the correlation length.

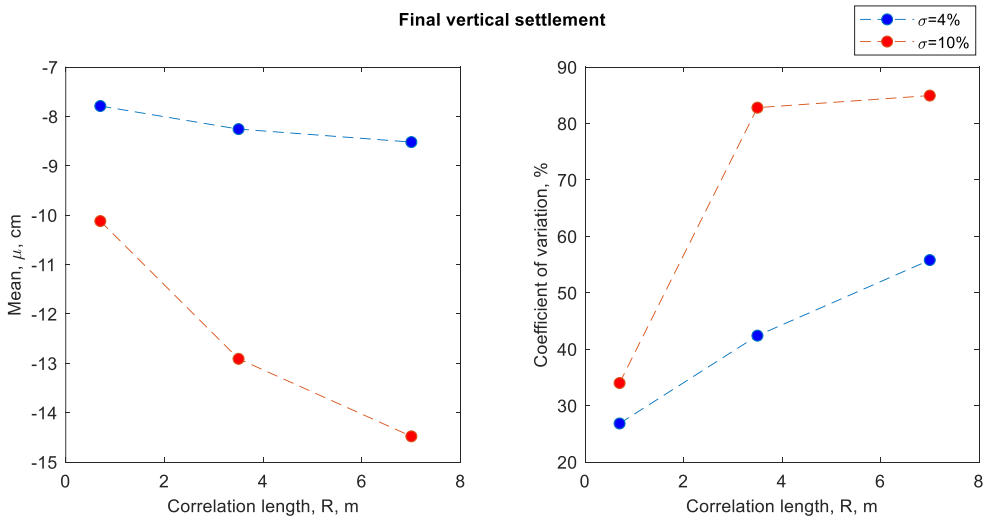

Figure 56. Mean and coefficient of variation for the final vertical settlement vs. the correlation length.

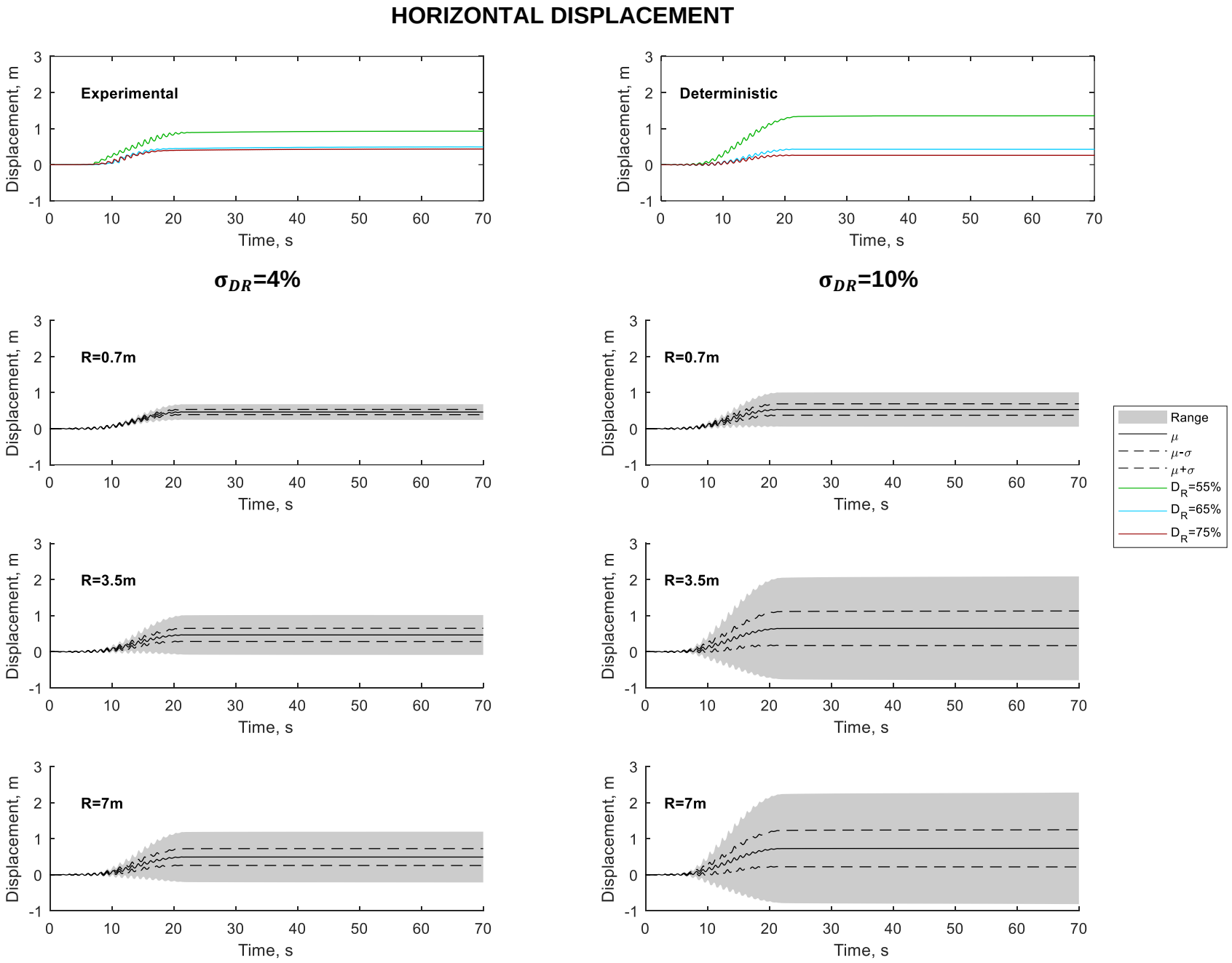

Figure 57. Experimental, deterministic, and stochastic horizontal displacements at the top of the sheet pile (Z=5m)

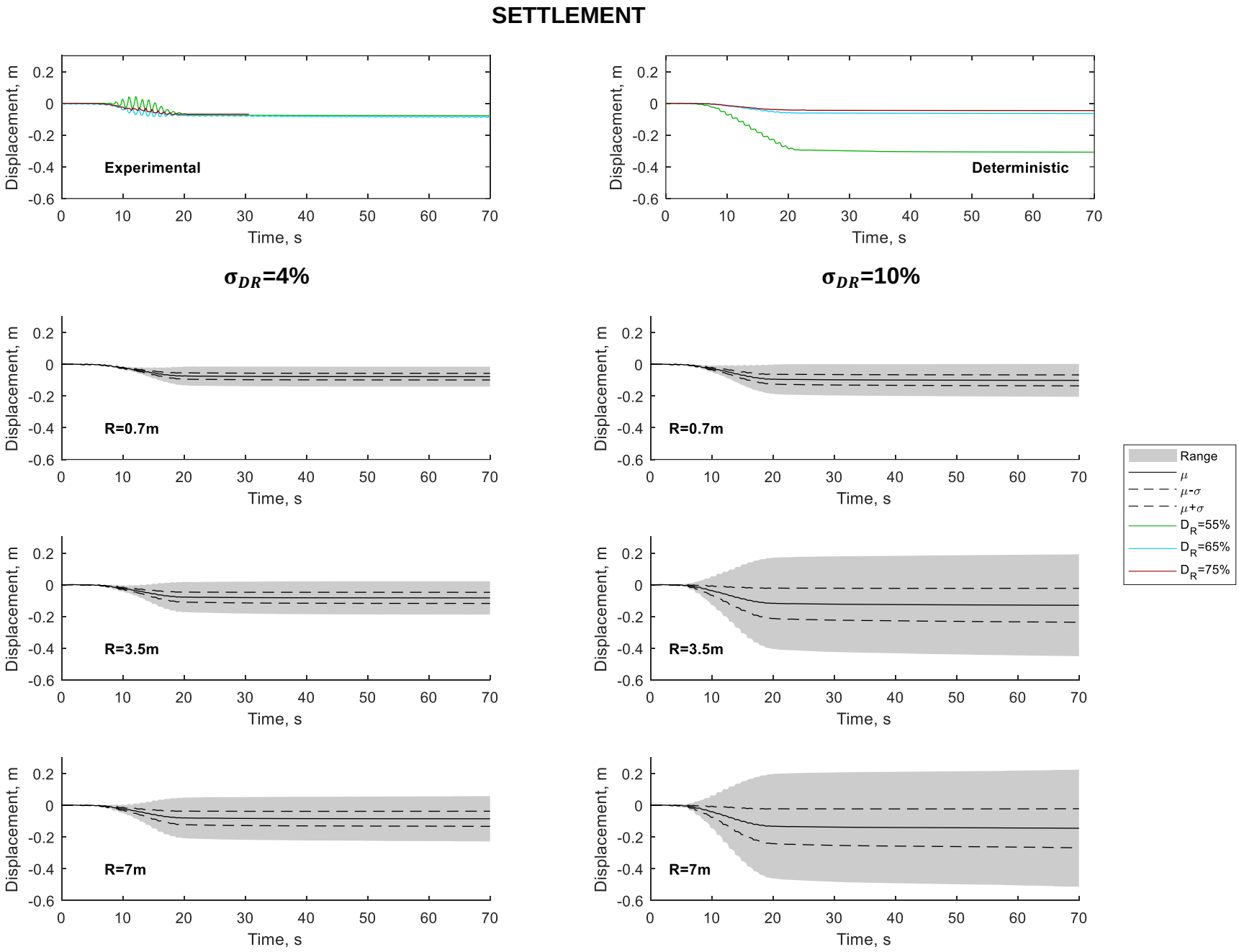

Figure 58. Experimental, deterministic, and stochastic settlements located 1 meter from the sheet-pile

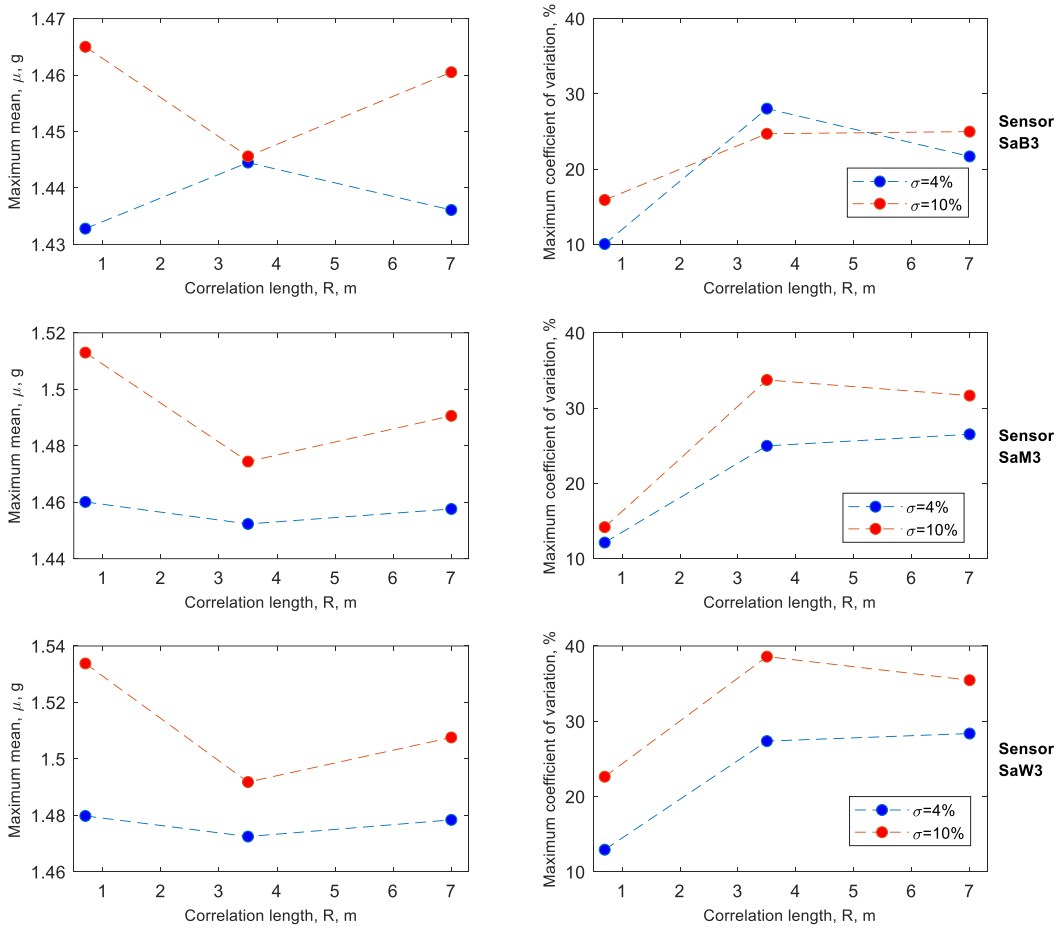

Figure 59. Maximum mean and coefficient of variation of the spectral acceleration response vs. the correlation length

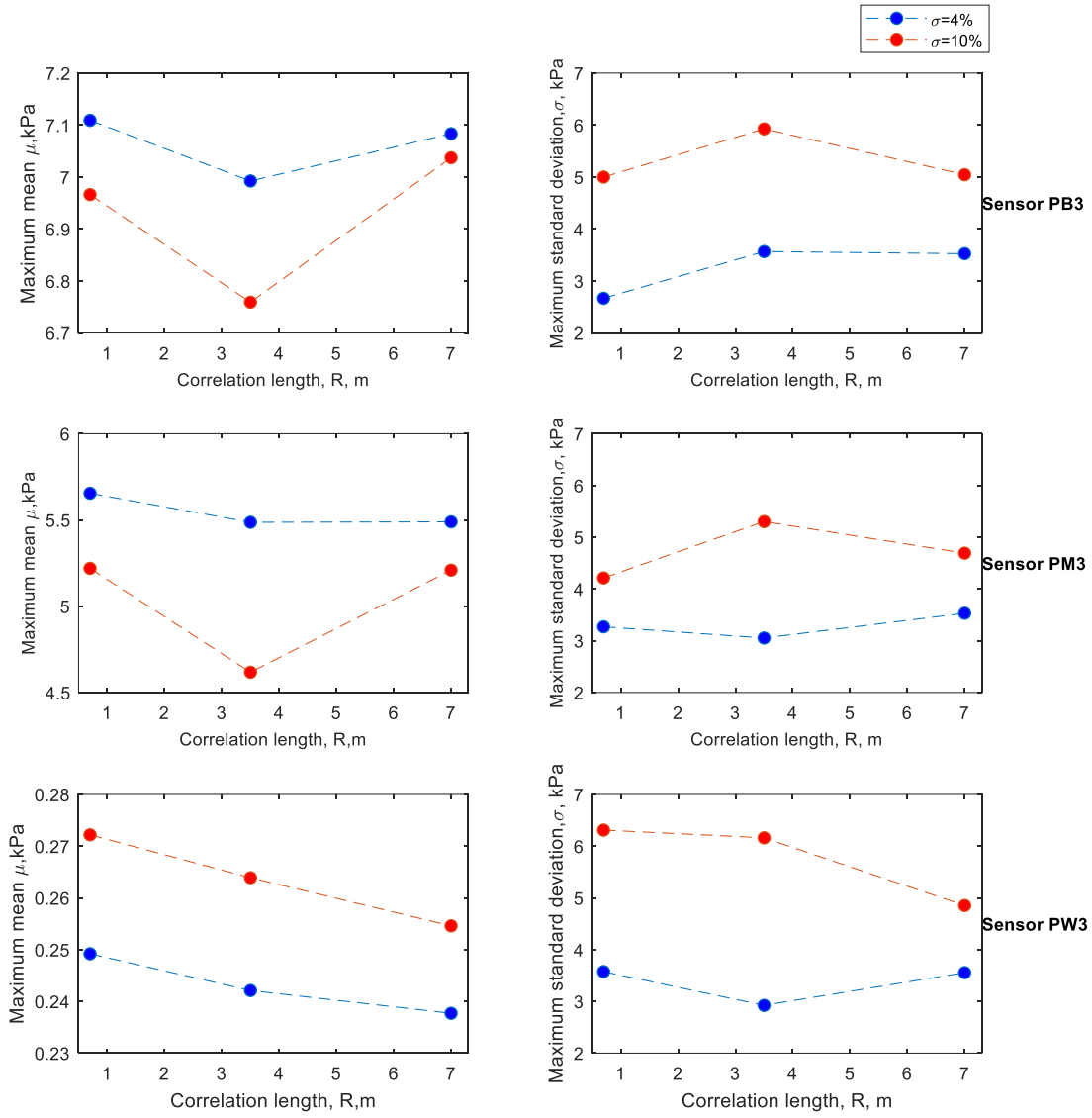

Figure 60. Maximum mean and coefficient of variation of the Excess Pore-water Pressure vs. the correlation length

7. Conclusions

7.1. Conclusions

In this research, it was possible to assets the effects of soil variability in the response of a liquefiable soils deposit supported by a retaining wall using the Random Finite Element Method, which combines the theory of random fields with Finite elements Analysis. A deterministic and a stochastic analysis was developed to achieve the objectives of the research. The deterministic simulations showed that the pressure-dependent multi-yield-surface model PDMY02 was able to reasonable capture the behavior of the sheet-pile system in terms of acceleration response, excess pore water pressure, vertical settlements, and horizontal displacements. Likewise, the stochastic analyses were also able to reproduce the centrifuge results of the system under study with the advantage of predicting a confidence interval for the expected results, considering the uncertainties due to the inherent variability of the soil, which were represented by evaluating the relative density as a Gaussian Random Field. The following conclusions can be drawn from this research:

- The PDMY02 model was able to reasonably follow the trend in terms of acceleration response, spectral acceleration, excess pore-water pressure, horizontal displacement, and vertical displacement.
- In terms of the acceleration response the deterministic model was not able to capture the dilation spikes presented on the centrifuge testing. Meanwhile, the probabilistic model was able to predict some of these spikes for the correlation lengths of 3.5 m and 7 m.
- The centrifuge experiments differ from the deterministic and probabilistic results in the excess pore-water pressure prediction near the sheet pile (SENSOR PW3). This could have been the cause due to external factors in the experimental configuration, such as friction. However, further research is needed.

- The probabilistic analyses did not show big variations in terms of the acceleration response and the spectral acceleration. The variables that are most influenced by inherent variability; represented in this work as the random fields of the relative density, are the excess pore-water pressure, the vertical settlements, and the horizontal displacements, which showed a wider 99.7% confidence interval ($\mu_{DR} \pm 3\sigma$).
- The probabilistic simulations showed an increment in the prediction intervals between the first and second scenario. The mean values of the probabilistic predictions are not affected by the correlation length in most cases, where it remains almost constant with the increment in the correlation length. However, the range of variation is directly affected by the correlation length. The variation in the acceleration response increases with the correlation length. In terms of excess pore-water pressure, the biggest variation was achieved for the correlation length of 3.5 m. The final horizontal displacement showed that between the correlation length of 0.7 m and 3.5 m the variation increases with a slope of 11.36% and 20.45% for the first and second scenario, respectively; meanwhile, between the correlation length of 3.5 m and 7.0 m the slope of variation becomes almost constant (2.7%). In terms of the final vertical settlement, between the correlation length of 0.7 m and 3.5 the variation increases with a slope of 6.8% for the first scenario and 22.7% for the second scenario, between 3.5m and 7.0 m the variation increases with a slope of 5%.
- Even tough, the mean value of the relative density in the probabilistic analysis was 65%, it was noted that the range of uncertainty of these analyses can reach values for the soil response that cover the experimental results for the relative densities between 55% to 75%.
- It was found that the range of variation of the results increases with the correlation length. This occurs because when a small correlation distance is evaluated, the soil presents small pockets with loose material and others with denser material, in such a way that the mean for different scenarios is similar, because the effects of loose sand pockets are compensated by the effects of dense sand pockets. On the other hand, when a large correlation length is evaluated, the soil can have a large area

with either dense or loose material. Such large areas are comparable to the size of the model, leading to a response that is dominated by either loose or dense soil, deviating from the mean response. However, further investigations related to the effects of the correlation length is needed.

- Stochastic analyses are a useful tool for determining the response of liquefiable soils because they are a way of capturing the uncertainties related to the variability of the soil deposit and the assumptions implemented for the numerical models. This way, it is possible to predict the soil response with a confidence interval. This will contribute to the development of safer and more optimal geotechnical designs as we gain a better understanding of the effects of uncertainties in soil variability.

7.2. Limitations and recommendations

For future work, several recommendations can be addressed. Firstly, it is recommended to increase the number of simulations. This way, it is possible to obtain a more representative sample for every scenario. Another recommendation is evaluating another source of uncertainty in the soil, such as the uncertainty due to systematic errors in experimental measurements. Test-to-test variability is still a recognized challenge in geotechnical engineering, which should also be addressed in future research efforts. Additionally, other variables affecting the soil response can be considered as random variables, such as the magnitude of the input motion and its frequent content.

One of the limitations of this study is that there was not available information for estimating the correlation length of the random fields, therefore, it was decided to choose different values to evaluate its influence on the soil response according to the dimensions of the problem in consideration. However, it was possible to see that this variable has a big influence in the soil response, therefore, it should be accurately estimated to reproduce the real soil conditions. Methodologies for the estimation of the correlation length according to the in-situ soil and experimental conditions should be considered for further research. Another recommendation is to study different correlation functions to determine which function presents a better match to in situ soil conditions.

References

[1] A. Vasko, "Stress Controlled Cylic Triaxial Tests," DEEDS , 2015 . [Online]. Available: https://datacenterhub.org/dataviewer/view/nees_datastore_1064:db/stress_controlled_cyclic_triaxial_tests/?filter=cyclic_loaded_triaxial_tests.control|Stress.

[2] ElGhoraiby, Park and Manzari, "PRJ-1783: LEAP-2017 GWU Laboratory Tests," DESIGNSAFE, 2017. [Online]. Available: https://www.designsafe-ci.org/data/browser/public/designsafe.storage.published//PRJ-1783/Cyclic%20Stress-Controlled%20Triaxial%20Tests.

[3] F. Ochoa-Cornejo, A. Bobet , C. Johnston, M. Santagata and J. Sinfield, "Cyclic behavior and pore pressure generation in sands with laponite, a super-plastic nanoparticle,," *Soil Dynamics and Earthquake Engineering,* vol. 88, no. 88, pp. 265-279, 2016.

[4] T. L. Holzer , M. Bennett, D. Ponti and I. Tinsley , "Liquefaction and soil failure during 1994 Northride earthquake," *Journal of Geotechnical and Geoenvironmental Engineering,* pp. 428-252, 1999.

[5] S. Bhattacharya, M. Hyodo, K. Goda, T. Tazoh and C. Taylor, "Liquefaction of soil in the Tokyo Bay area from the 2011 Tohoku (Japan) earthquake," *Soil Dynamics and Earthquake Engineering,* pp. 1618-1628, 2011.

[6] B. Seed and I. Idriss, "Analysis of soil liquefaction: Niigata earthquake," *Journal of the Soil Mechanics and Foundations Division,* vol. 93, no. 3, pp. 83-108, 1967.

[7] G. Castro and P. Steve, "Factors affecting liquefaction and cyclic mobility," *Journal of the Geotechnical Engineering Division,* vol. 103, no. GT6, pp. 502-516, 1977.

[8] D. Drucker and W. Prager, "Soil mechanics and plastic analysis or limit design," *Quarterly of Applied Mathematics,* vol. 10, no. 2, pp. 157-165, 1952.

[9] K. Roscoe and J. Burland, "On the generalized behaviour of "wet" clay," *Engineering Plasticity,* vol. 48, pp. 535-609, 1968.

[10] T. Adachi and F. Oka, "Constitutive equation for normally consolidated clays based on elasto-vicoplasticity," *Soils and Foundations,* vol. 22, pp. 57-50, 1982.

[11] Y. Dafalias, A. Papadimitriou and M. Manzari, "Simple anisotropic plasticity model for soft clays," in *Geo-Frontiers Congress* , Austin Texas, 2005.

[12] F. Darve, "An incrementally non-linear constitutitve law: Assumptions and predictions," in *Proc. Int. workshop on Constitutive Relations for Soils*, Grenoble, 1982.

[13] D. Kolymbas, "Computer-aided design of constitutive laws," *International Journal for Numerical and Analytical Methods in Geomechanics* , vol. 15, pp. 593-604, 1991.

[14] W. Fuentes, D. Masin and J. Duque, "Constitutive model for monotonic and cylic loading on anisotropic clays," *Geotechnique,* pp. 1-17, 2020.

[15] G. Gudehus, "A comprenhensive constitutive equation for granular materials," *Soils and Foundations,* vol. 36, no. 1, pp. 1-12, 1996.

[16] W. Iwan, "On a Class of Models for the Yielding Behavior of Continuos and Composite Systems," *J. appl. Mech* , vol. 34, no. 3, pp. 617-617, 1967.

[17] Z. Mróz, "On the description of anisotropic workhardening," *Journal of the Mechanics and Physics of Solids,* vol. 15, no. 3, pp. 163-175, 1967.

[18] J.-H. Prevost, "Plasticity Theory for Soil Stress-Strain Behavior," *Journal of the Engineering Mechanics Division,* vol. 104, no. 5, pp. 1177-1194, 1978.

[19] M. Klisinski, "Plasticity theory based on fuzzy sets," *Journal of Engineering Mechanics,* vol. 114, no. 4, pp. 563-582, 1988.

[20] P. Lade, "Elasto-Plastic Stress.Strain Theory for Cohesionless Soil with Curved Yield Surfaces," *International Journal of Solids and Structures,* vol. 13, no. 11, pp. 1019-1035, 1977.

[21] R. Brinkgreve and P. Vermeer, "PLAXIS finite element code for soil and rock analysis," Balkema, Rotterdam, 1997.

[22] M. Hicks, "Experience in calibrating the double-hardening constitutive model Monot," *International Journal for Numerical and Analytical Methods in Geomechanics* , vol. 27, pp. 1123-1151, 2003.

[23] Y. Dafalias, L. Herrmann and J. DeNatale, "The bounding surface plasticity model for isotropic cohesive soils and its application at the Grenoble Workshop," in *Proc Int. Workshop on Constitutive Relations for Soils*, Grenoble, 1982.

[24] . V. N. Kaliakin and Y. F. Dafalias, "Simplifications to the bounding surface model for cohesive soils," *International Journal for Numerical and Analytical Methods in Geomechanics,* vol. 13, no. 1, pp. 91-100, 1989.

[25] E. K. Mojtaba and H. A. Taiebat, "A bounding surface plasticity model for highly crushable granular materials," *Soils and Foundations,* vol. 51, no. 6, pp. 1188-1201, 2014.

[26] M. Pastor, O. Zienkiewicz and A. Chan, "Generalized plasticity and the modelling of soil behaviour," *Numerical and Analytical Methods in Geomechanics,* vol. 14, no. 3, pp. 151-190, 1990.

[27] L. H.I. and H. Liu, "Pressure-level dependency and densification behavoir of sand through a generalized plasticity model," *Journal of Engineering Mechanics,* vol. 129, no. 8, pp. 851-860, 2003.

[28] P. V. Lade and K. K. Moon, "Single hardening constitutive model for soil, rock and concrete," *International Journal of Solids and Structures,* vol. 32, no. 14, pp. 1963-1978, 1995.

[29] M. Uzielli, S. Lacasse and F. Nadim, "Soil variabiability Analysis for Geotechnical Practice," in *Characterisation and Engineering Properties of Natural Soils,* vol. 3, 2006.

[30] D. Griffiths and G. Fenton, "Probabilistic slope stability analysis by finite elements," *Journal of Geotechnical and Geoenvironmental Engineering* , vol. 130, no. 5, pp. 507-518, 2004.

[31] M. A. ElGhoraiby and M. T. Manzari, "The effects of base motion variability and soil heterogeneity on lateral spreading of mildly sloping ground," *Soil Dynamics and Earthquake Engineering,* vol. 135, 2020.

[32] D. Breysse, H. Niandou, S. Elachachi and L. Houy, "A generic approach to soil.structure interaction considering the effects of soil heterogeneity," *Géotechnique,* vol. 55, no. 2, pp. 143-150, 2005.

[33] G. Fenton and D. Griffiths, "Three-dimensnional probabilistic foundation settlement," *Journal of Geotechnical and Geoenvironmental Engineering* , vol. 131, no. 2, pp. 232-239, 2005.

[34] G. Fenton and D. Griffitths , Risk Assessment in Geotechnical Engineering, New Jersey : John Wiley & Sons, Inc, 2008.

[35] F. Nadim, "Accounting for Uncertainty and Varibility in Geotechnical Characterization of Offshore Sites," *Geotechnical Safety and Risk ,* vol. V, pp. 23-34, 2015.

[36] F. McKenna , G. Fenves and M. Scott, "Open System for Earthquake Engineering Simulation," University of California, Berkeley, CA, 2000 .

[37] Z. Yang, Elgamal A and E. Parra, "Computational model for cyclic mobility and associated shear deformation," *Journal of Geotechnical and Geoenvironment Engineering,* vol. 129, no. 12, pp. 19-27, 2003.

[38] Yang, Z, J. Lu and A. Elgamal, "OpenSees soil models and solid-fluid fully coupled elements. User's Manual," University of California. Department of Structural Engineering., San Diego , 2008.

[39] A. Khosravifar, A. Elgamal, J. Lu and J. Li , "A 3D model for earthquake-induced liquefaction triggering and postliquefaction," *Soil Dynamics and Earthquake Engineering,* vol. 110, pp. 43-52, 2018.

[40] Popescu, "VELACS," Sponsored by the Earthqake Hazard Mitigation Program of the National Science Foundation, [Online]. Available: https://www.princeton.edu/~dynaflow/radu/soil/velacs/.

[41] Kutter, Carey, Hashimoto, Zeghal, Abdoun, Kokkali, Madabhusgi, Haigh, Burali d'Arezzo, Madabhushi, Hung, Lee, Cheng, Iai, T. Tobita, T. Ashino, J. Ren, Y. Zhou, Y. Chen, Z. Sun and M. Manzari, "LEAP-GWU-2015 experiment specifications, results, and comparisons,," *Soil Dynamics and Earthquake Engineering,* vol. 113, pp. 616-628, 2018.

[42] B. Kutter, M. Manzari and M. Zeghal , Model Tests and Numerical Simulations of Liquefaction and Lateral Spreading LEAP-UCD-2017, Springer Open, 2017.

[43] L. Chen, A. Ghofrani and P. Arduino , "Remarks on numerical simulation of the LEAP-Asia-2019 centrifuge tests," *Soil Dynamics and Earthquake Engineering,* vol. 142, 2021.

[44] V. Mercado, W. El-Sekelly and M. Pico , "LEAP 2020 TYPE-B SIMULATIONS AT UNIVERSIDAD DEL NORTE," *Under Revission,* 2021.

[45] V. Mercado, W. El-Sekelly and M. Pico, "Leap 2020 Type C predictions simulations," *Under development.*

[46] Z. Yang and A. Elgamal , "Numerical Modeling of Earthquake Site Response Including Diland and Liquefaction," Department of Strcutural Engineering, Univerisity of California, San Diego, 2000.

[47] M. e. a. Zeghal, "LEAP-RPI 2020, Model Specifications".

[48] X. Li and H. Ming, "Unified modeling of flow liquefaction and cylic mobility," *Soil Dynamics and Earthquake Engineering* , vol. 19, pp. 363-369, 2000.

[49] B. Dursun and K. Ibrahim , "Damages According to Liquefaction And Suggestions," *IOSR Journal of Engineering (IOSRJEN),* vol. 6, 2016.

[50] T. He, A. Hulsey , M. L. Jiminian , E. Jampole , A. Morales , A. Perez, S. Raj and S. Whicman, "Reconfiguring New Zealand's Built Environment After the 2012-2011 Canterbury Earthquake Sequence and the 2016 Mw 7.8 Kaikoura Earthquake," A product of the EERI learning From Earthquakes Program, 2019.

[51] "Soil liquefaction leaves Indonesian island in ruins," *Turkiye,* 14 Oct 2018.

[52] N. Pirhadi, X. Tang, Q. Yang and F. Kang, "A new equation to evaluate liquefaction triggering using the response surface mehotd and parametric sensitivity analysis," *Sustainability,* vol. 11, p. 112, 2019.

[53] T. Kokusho, "Liquefaction potential evaluations by energy-based method and stress-based method for various ground motions: Supplement," *Soil Dynamics and Earthquake Engineering,* vol. 95, pp. 40-47, 2017.

[54] Y. Chen, S. Hsieh, J. Chen and C. Shih, "Energy-based probabilistic evaluation of soil liquefaction," *Soil Dynamics and Earthquake Engineering,* vol. 25, no. 1, pp. 55-68, 2005.

[55] A. H. Alavi and A. H. Gandomi, "Energy-based numerical models for assessment of soil liquefaction," *Geoscience Frontiers,* vol. 3, no. 4, pp. 541-555, 2012.

[56] T. Youd, I. Idriss and R. D. Andrus, "Liquefaction Resistance of Soils: Summary Report from the 1996 NCEER and 1998 NCEER/NSF Workshops on Evaluation of Liquefaction Resistance of Soils," *Journal of Geotechnical and Geoenvironmental Engineering,* vol. 127, no. 10, 2001.

[57] I. Idriss and R. Boulanger, "Semi-empirical procedures for evaluating liquefaction potential during earthquakes,," *Soil Dynamics and Earthquake Engineering,* vol. 26, no. 2–4, pp. 115-130, 2006.

[58] R. Moss, R. Seed, R. Kayen and J. Stewart, "CPT-Based Probabilistic and Deterministic Assessment of In Situ Seismic Soil Liquefaction Potential," *Journal of Geotechnical and Geoenvironmental Engineering,* vol. 132, no. 8, 2006.

[59] J. Berrill and R. Davis, "Energy Dissipation and Seismic Liquefaction of Sands: Revised Model," *Soils and Foundations,* vol. 25, no. 2, pp. 106-118, 1985.

[60] M. H. Baziar, Y. Jafarian, H. Shahnazari, V. Movahed and M. Amin Tutunchian, "Prediction of Strain Energy-Based Liquefaction Resistance of Sand-Silt Mixtures: An Evolutionary Approach," *Computer Geoscience,* vol. 37, pp. 1883-1893, 2011.

[61] D. Okur and A. Ansal, "Stiffness degradation of natural fine grained soils during cyclic loading," *Soil Dynamics and Earthquake Engineering,* vol. 27, no. 9, pp. 843-854, 2007.

[62] P. V. Lade, "Overview of Constitutive Models For Soils," in *Geo-Frontiers Congress 2005,* Austin, Texas, United States, 2005.

[63] D. C., "Constitutive Modeling for Geologic Materials: Significance and Directions".

[64] I. Smith and D. Griffiths, Programming the finite element method, John Wiley & Sons, 1982.

[65] R. Brinkgreve and P. Vermeer, "Plaxis: Finite Element Code for Soil and Rock Analyses," Balkema, 1999.

[66] M. Manzari and Y. Dafalias , "A critical state two-surface plasticity model for sands," *Géotechnique,* vol. 27, no. 2, pp. 255-272, 1997.

[67] X. Li and Y. Dafalias, "Dilatancy for cohesionless soils," *Géotechnique,* vol. 54, no. 4, pp. 449-460, 2000.

[68] Y. Dafalias , A. Papadimitiou and X. Li, "Sand plasticity model accounting for inherent fabric anisotropy," *Journal of Egineering Mechanics,* vol. 130, no. 11, pp. 1319-1333, 2004.

[69] Y. Dafalias and M. Manzari, "Simple plasticity sand model accounting for fabric change effects," *Journal of Egineering Mechanics* , vol. 130, no. 6, pp. 622-634, 2004.

[70] M. Taiebat and Y. Dafalias, "SANISAND: Simple anisitropic sand plasticity model," *International Journal for Numerical and Analytical Methods in Geomechanics,* vol. 32, pp. 915-948, 2008.

[71] R. Boulanger and K. Ziotopoulou, "Formulation of a sand plasticity plane-strain model for earthquake engineering applications," *Soil Dynamics and Earthquake Engineering* , vol. 53, pp. 254-267, 2013.

[72] K. Ziotopoulou and R. Boulanger, "Plasticity modeling of liquefaction effects under sloping ground," *Soil Dynamics and Earthquake Engineering* , vol. 84, pp. 269-283, 2016.

[73] J. H. Prevost, "A simple plasticity theory for frictional cohesionless soils," *Soil Dynamics and Earthquake Engineering* , vol. 4, no. 1, 1985.

[74] J. Prevost, "Mathematical Modelling of Monotonic and cyclic Undrained Clay Behaviour," *Int. J. Num. Meth. Geom.*, vol. 1, no. 2, pp. 195-216, 1977.

[75] J. Prevost, "Anisotropic Undrained Stress-Strain Behavior of Clays," *J. Geotech. Eng. Div*, vol. 104, no. GT8, pp. 1075-1090, 1978.

[76] A. Elgamal, Z. Yang, E. Parra and A. Ragheb, "Modeling of cyclic mobility in saturated," *International Journal of Plasticity*, vol. 19, p. 883–905, 2003.

[77] A. L. Jones, S. L. Kramer and P. Arduino, "Estimation of Uncertainity in Geotechnical Properties for Performance-Based Earthquake Engineering," Pacific Earthquake Engineering Research Center, University of California, Berkeley , 2002.

[78] Phoon,K and F. Kulhawy, "Characterization of geotechnical variability," *Canadian Geotechnical Jorunal*, vol. 36, pp. 625-639, 1999.

[79] M. Huber, *Soil variability and its consequences in geotechnical engineering*, Institut für Geotechnik der Universität Stuttgart, 2013.

[80] Lacasse and Nadim, "Uncertainities in characterizing soil properties," *Unvertainity in the Geologic Environment, From Theory to Practice, Proceeding of Uncertainity* , vol. Geotechnical Special Publication, no. 58, 1996.

[81] R. Lark, "Estimating variograms of soil properties by the method-of-moments and maximum likelihood," *European Journal of Soil Science*, vol. 51, no. 4, pp. 717-728, 2000.

[82] G. A. Fenton and E. H. Vanmarcke, "Simulation of Random Fields via Local Average Subdivision," *Journal of Engineering Mechanics,* vol. 116, no. 8, 1990.

[83] N. S.P., "Maximum likelihood Bayesian averaging of uncertain model predictions," *Stochastic Environmental Research and Risk Assessment,* vol. 17, p. 291–305, 2003.

[84] V. E., Random Fields: Analysis and Synthesis, Cambridge : MIT Press, 1983.

[85] C. Williams, Prediction with Gaussian processes: from linear regression to linear prediction and beyond, Michael Irwin Jordan, 1999, pp. 599-621.

[86] P. Hemyari and D. Nofziger, "Analytical solution for puncrual kriging in one dimension," *Soil Science Society of Americal Journal* , vol. 51, no. 1, pp. 268-269, 1987.

[87] A. Kolmogorov, Interpolation and extrapolation of stationary random sequences, Moscow: Bull. Moscow Univ., 1941.

[88] A. Journel and C. Huijbregts , Mining geostatistics, London: London Academic Press, 1978.

[89] J. Davis, Statistics and data analysis in geology - 2nd edition, New York: John Wiley & Sons, 1986.

[90] C. J.R., Numerical analysis for the geological sciences, Englewood Cliffs: Prentice Hall, 1995.

[91] F. Nadim, "Geotechnical site description using stochastic interpolation," in *Proceedings of the 10th Nordic Geotechnical Meeting* , Oslo, Norway, 1988.

[92] F. Nadim and S. Lacasse, "Probabilistic slope stability evaluation," *Proceedings of the 18th Annual Seminar on Geotechnical Risk Management* , pp. 177-186, 1999.

[93] K. Phoon , F. Kulhawy and M. Grigoriu, "Development of a reliability-based design framework for tansmission line structure foundations," *Journal of Geotechnical and Geoenvironmental Engineering,* vol. 129, no. 9, pp. 798-806, 2003a.

[94] K. Phoon , F. Kulhawy and M. Grigoriu, "Multiple resitance factor design (MRFD) for spread fondations," *Journal of Geotechnical and Geoenvironmental Engineering* , vol. 129, no. 9, pp. 807-818, 2003b.

[95] R. Popescu, G. Deodatis and A. Nobahar, "Effects of random heterogeneity of soil properties on bearing capacity," *Probabilistic Engineering Mechanics,* vol. 20, pp. 324-341, 2005a.

[96] N. Chen and C. Guedes Soares, "Spectral stochastic finite element analysis for laminated composite plates," *Computation Methods for Appling Mechanics Engineering,* vol. 197, pp. 4820-4839, 2008.

[97] C. Choi and H. Noh, "Stochastic finite element analysis of plate structures by weighted integral methods," *Structural Engineering Mechanics* , vol. 4, pp. 703-715, 1996.

[98] C. Choi and H. Noh, "Stochastic finite element analysis of shape imperfections in RC cooling tower shells," *Journal of Structural Engineering* , pp. 417-423 , 2000.

[99] A. D. Kiureghian and J. Ke, "The stochastic finite lemeent method in structural reliability," *Probabilist. Engrg. Mech.* , vol. 3, pp. 83-91, 1988.

[100] G. Falsone and G. Ferro, "A dynamical stochastic finite element method based on the moment equation approach for the analysis of linear and nonlinear uncertain structures," *Struct. Engrg. Mech,* vol. 23, pp. 599-613, 2006.

[101] G. Stefanou, "The stochastic finite element method: past, present and future," *Comput. Methods Appl. Mech. Engrg.,* vol. 198, pp. 1031-1051, 2009.

[102] M. Kleiber and T. Hien , The Stochastic Finite Element Method, New York: John Wiley & Sons, 1992.

[103] R. Ghanem and P. Spanos, Stochastic Finite Elements: A Spectral Approach, Berlin: Springer-Verlag, 1991.

[104] Papadrakakis, M and Papadopoulos, V, "Robust and efficient methods for stochastic finite element analysis using Monte Carlo Simualtion," *Compute rMethods in Applied Mechanics and Engineering* , vol. 134, no. (3-4), pp. 325-340, 1996.

[105] D. Griffiths and G. Fenton , "Bearing capacity of spatially random soil: the undrained clay Prandtl problem revisited," *Géotechnique,* vol. 51, no. 4, pp. 351-359, 2001.

[106] P. Allahverdizadeh, F. Griffiths and G. Fenton, "The Random finite Element Method (RFEM) in Porbabilistic Slope Stability Analysis with Consideration of Spatial Variability of Soil Properties," in *IFCEE 2015*, San Antonio, Texas, 3015.

[107] D. Griffiths, G. Fenton and H. Ziemann , "Realiability of passive earth pressure," *Georisk,* vol. 2, pp. 113-121, 2008.

[108] S. E. Cho, "Probabilistic analysis of seepage that considers the spatial variability of permeability for an embankment on soil foundation," *Engineering Geology,* vol. 133–134, pp. 30-39, 2012.

[109] E. Vanmarcke, Random Fields: Analysis and Synthesis, Cambridge, Massachussetts: MIT Press, 1984.

[110] C. Powell, "Generating Realisations of Stationary Gaussian Random Fields by Circulant Embedding," 20213.

[111] M. Gutierrez and R. De Borst, "Stochastic Finite Element Methods," in *Comprenhensive Structural Integrity*, Delft University of Technology,The Netherlands, Elsevier, 2003, pp. 607-635.

[112] C. Harris, K. Millan and S. van der Walt, "Array programming with NumPy," *Nature,* vol. 585, p. 357–362, 2020.

[113] "Numpy.random.multivariate_normal," Numpy, [Online]. Available: https://numpy.org/doc/stable/reference/random/generated/numpy.random.multivariate_normal.html. [Accessed 4 03 2021].

[114] A. Papoulis, Probability, Random Variables, and Stochastic Processes, New York: McGraw-Hill, 1991.

[115] Mathworks, "Cubic spline data interpolation, User's Guide," 2012b. [Online]. Available: https://www.mathworks.com/help/matlab/ref/spline.html. [Accessed 10 01 2021].

[116] MATLAB, *verion 7.10-0,* Natick, Massachusetts: The MathWorks Inc., 2010.

[117] B. Kutter , T. Carey , T. Hashimoto , M. Zeghal , T. Abdoun and P. Kokkali , "LEAP-GWU-2015 experiment specifications, results and comparisions," *Soil Dynamic Earthquake Engineering,* vol. 113, pp. 616-28, 2017.

[118] S. Mazzoni, F. McKenna, M. H. Scott and G. L. Fenves, "OpenSees command language manual," *Pacific Earthquake Engineering Research (PEER) Center,* vol. 264, 2006.

[119] M. Scott and G. Fenves, "Krylov subspace accelerated Newton algorithm: application to dynamic progressive collapse simulation of frames," *Journal of Structural Engineering,* vol. 136, no. 5, pp. 472-480, 2009.

[120] A. Vytiniotis, "datacenterhub," 2014. [Online]. Available: https://datacenterhub.org/resources/13727/supportingdocs.. [Accessed April 2020].

[121] D. Drucker and W. Prager, "Soil Mechanics and Plastic Analysis or Limit Design," *Quarterly of Applied Mathematics,* vol. 10, no. 2, pp. 157-165, 1952.

[122] S. Kramer, Geotechnical Earthquake engineering, Upper Saddle River, New Jersey: Prentice-Hall, 1996.

[123] R. Kondner and J. Zelasko , "Hyperbolic stress–strain formulation for sands," in *Proceedings of the 2nd Pan-American conference on soil mechanics and foundations engineering*, Sao Paulo, Brazil, 1963.

[124] B. Hardin and V. Drnevich, "Shear modulus and damping in soils," *Journal of the Soil Mechanics and Foundations Division* , vol. 98, no. 7, pp. 667-692, 1972.

[125] Z. Mroz, "On the description of anisotropic work hardening," *Journal of the Mechanics and Physics of Solids* , vol. 15, no. 1, pp. 63-75, 1967.

[126] A. Parra Bastidas, "Ottawa F-65 Sand Characterization," Dissertation University of California Davis, Davis, California, 2016.

[127] A. Alarcon-Guzman , A. Leonards and J. Chameau , "Undrained monotonic and cyclic strenght of sands," *Journal of Geotechnical Engineering* , vol. 114, no. 10, pp. 1089-1109, 1988.

[128] M. ElGhoraiby , H. Park and M. Manzari, "Physical and mechanical properties of Ottawa F65 sand," *Kutter B, Manzari M, Zeghal M, editors. Model tests numer. Simulations liq. Lateral spreading*, pp. 41-62, 2019.

[129] K. Ziotopoulou and R. Boulanger, "Calibration and implementation of a sand plasticity plane-strain model," *Soil Dynamics and Earthquake Egineering* , vol. 53, pp. 268-280, 2013.

[130] B. Matasovic and M. Vucetic , "Cyclic characterization of liquefiable sands," *Journal of Geotechnical Engineering*, vol. 119, no. 11, pp. 1805-1822, 1994.

[131] T. Wolff, E. Demsky, J. Schauer and E. Perry , "Reliability assessment of dike and leeve embankments," *Uncertainty in the Geologic Environment, From Theory to*

Practice, vol. Proceeding of Uncertainty'96, no. Geotechnical Special Publication No. 58 , 1996.

[132] P. Lumb, "The variability of natural soils," *Canacdian Geotechnical Journal,* vol. 3, pp. 74-79, 1966.

[133] D. Assimaki, "Spatial variability of soil properties in forwared and inverse site response analyses," in *Proceedings of GeoCongress*, Atlanta, 2006.

[134] T. Carey , B. Kutter , M. Manzari and M. Zeghal , *Leap Soil Properties and Element Test Data*, 2017.

Appendix

Random Field Generation Algorithm

```
import pandas as pd
import matplotlib.pyplot as plt
import numpy as np
n = 20;
m = 80;
x = np.linspace(0,20,m);
y = np.linspace(0,5,n);
drmean=65;
drs=10;
v=10**2;
XM,YM = np.meshgrid(x,y);          #parejas coordenadas
puntos = np.array([[xi,yi] for xi in x for yi in y]);
plt.plot(puntos[:,0],puntos[:,1],'ob');
label = np.arange(0,puntos.shape[0]).reshape((n,m));
## Building the correlation matrix
r = 2;
k = 0;
M = np.zeros((n*m,n*m));
for i in range(0,n):
```

```
  for j in range(0,m):
    p = np.array([i,j]);
    for i1 in range(0,n):
      for j1 in range(0,m):
        q = np.array([i1,j1]);
        eti = label[i1,j1];
        M[k,eti] = np.exp(-0.5*(np.linalg.norm(p-q)**2)/(2*(r**2)));

    k+=1;

print(M)
plt.matshow(M);
plt.colorbar()
mean=np.zeros(n*m);
mean=mean+drmean;
S = np.random.multivariate_normal(mean,M*v);
S = S.reshape(n,m);
plt.contourf(S)
print(S)
np.shape(S)
import scipy.io as sio
sio.savemat('Smatrix.mat', {'S':S})
```